



ÉCOLE POLYTECHNIQUE
FÉDÉRALE DE LAUSANNE

**Mathematical Modeling and Numerical
Simulation of Excitation-Contraction
Phenomena in the Heart**

Luis Miguel de Oliveira Vilaca

submitted to the Department of Chemistry in EPFL
in partial fulfillment of the requirements for the degree of

**Master of Science in
Molecular & Biological Chemistry**

June 2013

under the supervision of
Professor Alfio Quarteroni and Doctor Ricardo Ruiz-Baier

List of Figures

2.1	Human heart muscle anatomy [1].	14
2.2	Conduction system of the human heart and specific potential profile [2].	15
2.3	Different type of muscular cells [3].	16
2.4	Anatomical structure of a cardiomycte [4].	17
2.5	Biological structure of one sarcomere [5].	18
2.6	Typical structure of the cell membrane [6].	19
2.7	Scheme of the membrane's permeability. Hydrophobic and small uncharged polar molecules can cross the membrane passively or by non-specific pores. The presence of a charge in the molecule prevents any passage by simple diffusion.	19
2.8	Proteins' class associated to transport in cell membrane [7].	20
2.9	Gap junction strucutre [8].	21
2.10	Active transport mechanisms [9].	24
2.11	Five phases of the action potential [10].	26
2.12	Scheme of the sarcomere contraction [11].	27
2.13	Scheme of the contraction cycle of the sarcomeres [12].	28
2.14	Biochemical system of Ca^{2+} fluxes involved on the electro-mechanical coupling. The different acronyms stands respectively for: RyR (Ryanodine receptor), NCX (Na^+-Ca^{2+} exchanger, I_{NaCa} in table 2.3), PLB (phospholaban), and SR for the sarcoplasmic reticulum [13].	29
2.15	Scheme of the troponin complex of the thin filament and the effect of Ca^{2+} ion [12].	29
2.16	Scheme describing the potential membrane assumption used in GHK equation. .	33
2.17	Numerical scheme associated to electocardiac simulation [14].	37
2.18	Original electrical circuit used by Hodgkin & Huxley to represent the membrane [15].	39
2.19	Representation of the heart organ with a slice of the ventricular muscle and the respective proportion of different cells [16].	42
2.20	Scheme of the cell used in the ten Tusscher, Noble, Noble & Panfilov model. Each of the ionic current and the subcellular space are presented. The Buf_C resp. Buf_{SR} represented the buffer molecules situated in the cytosolic resp. sarcoplasmic reticulum compartments.	44
2.21	Scheme of the cell used in the Jafri, Rice & Winslow model (1998). Each of the ionic current and the subcellular space are represented. The $TRPN$, CaM and CSQ defines the three kind of buffers: troponin, calmodulin and calsequestrin. .	45
2.22	Protein structure of the EF hand calcium-binding domain with hand representation.	46
2.23	Transitions' diagram of the L-type Ca^{2+} channel's states. The subscript Ca indicates the mode Ca transitions while numerical subscripts represent the number of permissive subunits. The C respectively O states corresponds to the close resp. open states. The detailed mathematical model is presented in Appendix.	47
2.24	Transitions' diagram of the RyR's states. The subscript C (resp. O) indicates closed (resp. opened) states while numerical subscripts represent the subtype of closed or opened state. The detailed mathematical model is presented in Appendix.	47
2.25	Diagram of the Huxley crossbridge model [17].	48

2.26	Half muscle structure diagram of the Negroni Lascano crossbridge model [18]. L stands for the half-length sarcomere while h represents the myosin head elongation from the no force position $h = 0$	49
2.27	Diagram of the Ca^{2+} -kinetics used in the Negroni Lascano model.	50
4.1	Steady-state potential (left panels) and Ca^{2+} profile (right panels) for the three kind of ventricular cells by ten Tusscher & al model simulations. The profiles have been computed for 400, 600, 800 and 1000 ms stimulation intervals.	64
4.2	Comparative graphs of the steady-state potential (left) and Ca^{2+} profile (right). The profiles have been computed for 600 ms stimulation interval (1.67 Hz).	65
4.3	Comparative graphs of the steady-state currents dynamics for the three ventricular cells.	66
4.3	Comparative graphs of the steady-state currents dynamics for the three ventricular cells (continued).	67
4.4	Action potential duration restitution curves (left) and AP amplitude profiles (right) obtained via the two pacing protocols : S1-S2 standard restitution (top) and dynamic protocols (bottom).	67
4.5	Gating variables and associated currents obtained by simulation of ten Tusscher & al. model at 600 ms stimulation interval for the epicardial cell.	68
4.5	Gating variables and associated current obtained by simulation of ten Tusscher & al model at 600 ms stimulation interval for the epicardial cell (continued).	69
4.6	Ca_i^{2+} profiles obtained from JRW model computed with FE (left) and RK4 (right) method with constant time step $\Delta t = 10^{-4}$	70
4.7	Ca_{NSR}^{2+} - Ca_{JSR}^{2+} profiles obtained from JRW model computed with FE (left) and RK4 (right) method with constant time step $\Delta t = 10^{-4}$	71
4.8	Comparative graphs of the steady-state potential (left) and Ca^{2+} profiles (right). The profiles have been computed for 400, 600, 800 and 1000 ms stimulation intervals.	71
4.9	Dynamics of the calcium sub-system simulated by the JRW model at 600 ms stimulation interval.	73
4.10	Gating variables and associated currents obtained by simulation of JRW model at 600 ms stimulation interval.	74
4.11	Left: Muscle force response (F_m) to a step length (L).The step amplitude is equal to $-0.003 \mu m$ for a duration of 0.02 ms. Right: Stiffness diagram obtained from step length ΔL ranging from -0.005 and $0.001 \mu m$. Open circles represent the minimum drop force (F_1), while crossed points represents the force from quick partial recovery F_2 . F_1 and F_2 was normalized with respect to to steady state isometric force.	76
4.12	Profile of the crossbridges elastic elongation h for a length step of $-0.003 \mu m$ and $[Ca^{2+}] = 2\mu M$	76
4.13	Left: Different isotonic force step applied ranging from -75 mN to 0 $mN \cdot mm^{-2}$. Right: Associated half sarcomere L response to force step.	77
4.14	Isometric contraction at 1 Hz pacing frequency for the TNCP coupled model. Left: Simulation V , Ca_i^{2+} and F profiles. The force and the potential are normalized by their respective maximum value. Right: Respective TCA , TCA^* , T^* troponin state evolution with total force profile.	77
4.15	Isometric contraction at 1 Hz pacing frequency for JRW coupled model. Left: Simulation V , Ca_i^{2+} and F profiles. The force and the potential are normalized by their respective maximum value. Right: Respective TCA , TCA^* , T^* troponin state evolution with total force profile.	78

4.16 Isometric contraction at 1 Hz pacing frequency for TNNP model. The total muscle length is ranging from 0.85 and 1.15 μm . Left: Total muscle force profiles. Right: Elastic behavior of the cardiac muscle. (o) points represent the maximum peak force value of F , while (+) data are the resting value.	79
4.17 Isometric contraction at 1 Hz pacing frequency for JRW model. The total muscle length is ranging from 0.85 and 1.15 μm . Left: Total muscle force profiles. Right: Elastic behavior of the cardiac muscle. (o) points represent the maximum peak force value of F , while (+) data are the resting value.	79
4.18 Estimation of $[TCa]$ time evolution for TNNP model. The data was obtained from a 0.04 μm length pulse of length 0.02 s. (a): Isometric force response to different muscle length pulse applied at different time course. (b): Estimated TCa time course (+) with the associated TCa profile from normal isometric contraction. . .	80
4.19 Estimation of $[TCa]$ time evolution for JRW model. The data was obtained from a 0.04 μm length pulse of length 0.02 s. (a): Isometric force response to different muscle length pulse applied at different time course. (b): Estimated TCa time course (+) with the associated TCa profile from normal isometric contraction. . .	81
4.20 Values of the $F(Q_b, Q_r, Q_{d2})$ coupling term for TNNP (left) and JRW (right) obtained from an isometric contraction response to the different pulses length. . .	81
4.21 Series of afterloaded contraction experiments for the TNNP model. The results were obtained from clamp isotonic force ranging from 20 to 40 $mN \cdot mm^{-2}$. Left: F_m force muscle length. Right: L_m total muscle length.	82
4.22 Series of afterloaded contraction experiments for the JRW model. The results were obtained from clamp isotonic force ranging from 20 to 40 $mN \cdot mm^{-2}$. Left: F_m force muscle length. Right: L_m total muscle length.	83
4.23 Series of quick-release contraction experiments for TNNP model. The results was obtained from clamp isotonic force ranging from 20 to 40 $mN \cdot mm^{-2}$ at the maximum isometric force F_m . Left: F_m force muscle length. Right: L_m total muscle length.	83
4.24 Series of quick-release contraction experiments for JRW model. The results was obtained from clamp isotonic force ranging from 20 to 40 $mN \cdot mm^{-2}$ at the maximum isometric force F_m . Left: F_m force muscle length. Right: L_m total muscle length.	84
4.25 Active state profiles for different afterload quick-release contraction simulated with TNNP coupled model.	84
4.26 Muscle velocity shortening $\frac{dL_m}{dt}$ and maximum length shortening $L_m^{shortening}$ as a function of afterloaded F for TNNP model (left) and JRW model (right).	85

List of Tables

2.1	Some of the most common arrhythmia diseases and their localization [19].	16
2.2	Principal cardiac ionic channels in vertebrate species [20].	23
2.3	Principal cardiac ionic exchangers and pumps in vertebrate species [20].	25
2.4	Intra- and extracellular distribution of ions in cardiac myocytes [13] The concentrations are given in mM.	26
2.5	Ionic currents used in the TNNP model (2004).	43
3.1	Table of the parameters used for Ten Tusscher ionic model. The values in parenthesis are the original values of the K.H.W.J. ten Tusscher & A.V. Panfilov paper (2004).	53
3.2	Table of the parameters used for Jafri Rice Winslow ionic model. The values in parenthesis are the original values of the M.S Jafri, J.J. Rice & R.L. Winslow model (1998).	55
3.3	Definition table of the pacing protocol class' attributes encountered in the Appendix.	57
3.4	Table of the electro-mechanical coupling parameters based on the crossbridges model of Negroni & Lascano [18]. Y_1 and Z_1 have been modified for the JRW model in order to be consistent with the original equations.	58
4.1	Table of the maximum APD_{95} of the different simulated cells for the two kind of pacing protocols.	63

Contents

1	Introduction	10
1.1	Significance	10
1.2	Objectives	10
1.3	Outline	11
2	Theoretical Background	13
2.1	Cardiac System	13
2.1.1	Circulatory System and Cardiac Anatomy	13
2.1.2	Electrophysiology	14
2.2	Cardiomyocyte Structure and Biology	16
2.2.1	Muscular Cells	16
Classification and Morphology	16	
Cardiomyocytes	17	
2.2.2	Membrane Structure	18
Channel Proteins	21	
Transporters and Pumps	24	
2.2.3	Action Potential of Cardiomyocytes	25
2.2.4	Contraction's Mechanism of Cardiomyocytes	27
2.3	Chemistry and Physical Background	30
2.3.1	Thermodynamics and Electrochemistry	30
Migration on solution	30	
Nernst Equation	31	
Donnan Equation	32	
Goldmann-Hodgkin-Katz Equation	33	
2.4	Mathematical Description	34
2.4.1	Macroscopic Cardiac Models	34
Introduction	34	
Numerical analysis	36	
2.4.2	Ionic Models	38
General Scope	38	
ten Tusscher, Noble, Noble & Panfilov model	41	
Jafri, Rice & Winslow model	43	
2.4.3	Contraction Simulation	48
3	Numerical Analysis and Implementation	52
3.1	Electrophysiological simulation	52
3.1.1	Ionic models	52
3.1.2	Pacing protocols	56
3.2	Electro-mechanical coupling	57
3.2.1	Parameters and numerical solver	57
3.2.2	Contraction protocols	59

4 Results	62
4.1 Ionic Models	62
4.1.1 Ten Tusscher Model	62
4.1.2 Jafri-Rice-Winslow model	70
4.2 Cardiac Electromechanical model	75
4.2.1 Dynamic behavior with constant $[Ca^{2+}]$	75
4.2.2 Dynamics of electro-mechanical coupled models	76
5 Conclusion and Perspectives	86
5.1 Conclusion	86
5.2 Perspectives	87

Résumé

Cette présente thèse de Master a pour but d'étudier certains aspects computationnelles et physiologiques du mécanisme d'excitation-contraction dans le muscle cardiaque. Ce phénomène présente de nombreuses complexités à différentes échelles spatio-temporelles. La validité, ainsi que l'applicabilité de modèles ioniques récents, basés sur des théories phénoménologiques et physiologiques précises, seront testées.

Le choix des modèles traités sera basé sur un équilibre entre les résultats capables de reproduire correctement la complexité de l'électrophysiologie cardiaque et un coût computationnel faible afin de résoudre rapidement et correctement un ensemble d'équations différentielles qui décrivent la dynamique du modèle ionique associé. Les modèles inclus dans ce projet ont été sélectionnés par le fait qu'ils tiennent compte d'une large partie des découvertes et des connaissances électrophysiologiques les plus récentes (ex. canaux calciques du type L et récepteurs à ryanodine) afin de reproduire au mieux la conduction électrique dans le tissu cardiaque humain.

A partir de ces dernières remarques, l'ensemble des résultats et comparaisons effectués sur les modèles choisis ainsi que la simulation des mécanismes d'activation mécanique cellulaire sont produites à partir de la librairie LifeV pour les éléments finis.

Dans une deuxième étape, un modèle récent pour la description de la dynamique de la contraction musculaire sera implémenté. L'importance d'utiliser de bon modèles pour la dynamique des ions impliqués fait alors sens afin d'identifier correctement leurs influences possibles sur l'activation de la mécanique musculaire qui permet au cœur de pomper le sang à travers tout le système cardiovasculaire.

Abstract

In this Master thesis we aim at studying some physiological and computational aspects of the excitation-contraction mechanisms in the heart muscle. This phenomenon exhibits many complexities at different spatio-temporal scales. The relevance and applicability of several recent phenomenological and physiologically detailed ionic models will be assessed.

The choice of the treated models is based on an equilibrium between results that manage to reproduce correctly the complexity of the cardiac electrophysiology and a weak computational cost in order to solve the large set of ODEs which describe the dynamics of that ionic model. The preferred models include a large part of the more recent electrophysiological discoveries and understandings (e.g. L-type calcium and ryanodine channels) in order to reproduce at best the electrical conduction in the human cardiac tissue based on different experimental or computational measurements.

According to these previous remarks, we will perform a thorough testing and quantitative comparison of these models and mechanical activation mechanisms in the framework of the LifeV finite element library.

In a second step, a recent model for the description of crossbridge dynamics will be implemented. The importance of using good ionic models makes sense to identify correctly the possible influence on the muscle mechanics activation, which enable the heart to pump blood throughout the entire circulatory system.

Acknowledgments

Dans ces quelques lignes, je tiens à remercier les personnes qui par leur aide ou leur soutien m'ont permis de rendre ce présent travail.

En premier lieu, je voudrais remercier tout particulièrement le Professeur Alfio Quarteroni pour avoir avoir, avant tout, accepté ma candidature, afin que je puisse réaliser mon projet de Master dans sa chaire CMCS. Je remercie avant tout son ouverture d'esprit qui m'a permis, moi étudiant en chimie, d'effectuer un projet dans un domaine où mes connaissances étaient des plus basiques. Ces encouragements et son enseignement m'a permis de garder un pied en mathématique, une branche qui me passionne et m'intéresse depuis de très nombreuses années. Encore une fois merci.

De ce fait, je remercie également la section de Chimie et Génie Chimique qui m'a autorisé sans aucun problème à effectuer ce projet en dehors de ma section et de m'avoir permis, ainsi, d'échanger et partager mes connaissances avec des gens d'autres milieux académiques.

Je voudrais également exprimer tout mes remerciements à mon superviseur Docteur Ricardo Ruiz-Baier pour toute l'aide qu'il m'a apporté durant ce projet et pour sa patience d'écoute lors des mes nombreuses questions. Je le remercie tout particulièrement pour ses nombreuses relectures et conseils apportés à la rédaction de ce travail, dont la qualité serait bien moindre sans sa précieuse aide.

I switch momentary in English to thanks Simone Rossi for introducing me the LifeV library and the time spent to help me finding errors in the code and teaching me some aspects of C++ coding.

Je tiens aussi à témoigner ma gratitude à mes deux collègues de bureau Aymen Laadhari et Paolo Tricerri pour leurs humeur et leur joie de vivre qui a rendu agréable chacun des jours passés au bureau.

En dernier lieu, et non pas des moindre, je remercie ma famille et mes amis de La Bande, de l'EPFL et du club d'Aikido des Eaux-Vives pour leur soutien et leur présence.

Chapter 1

Introduction

1.1 Significance

With the increase of the computation power and rapidity, the increase of in silico experiments in many researches domain have been observed in the recent years. One of the domain where this evolution was particularly developed this kind of tools is linked with biochemical and biophysical studies. The recent Human Brain Project [21] sponsors by the European Union remind the effort made by scientists to improve this area. The number of different computation simulations focus of those research takes into account a large diversity of biological mechanism. From the microscopic scale, as protein structure or novel bio-transformations, to macroscopic scale, as organs (heart, brain) or biological system (circulatory system), the panel of research performed nowadays is very important. The main challenge of this approaches is to able to develop a general model which enables to reproduce and understand the experimental results obtained in laboratory. Such hypothetical model will be, for example, a way to predict the evolution or the disorders sources of a patient disease without the use of invasive controls or tests applied sometimes. However, it can also provide a parallel mean to increase to knowledge of underlying microscopic processes associated to a biological phenomenon which are sometimes difficult to assess in experimental measurements.

In this context, the computation of a general model of the circulatory system is from recent years the source of an important number of publications or research on the computing simulation area [22]. Heart is a hollow organ implied on the circulatory system which is principal function is to pump blood throughout the entire organs that contains a particular living species. For that reason, those publications are mainly concern in three important aspects: electrophysiology, tissue mechanics, and blood flow [22]. Even if a large numbers of models have been implemented nowadays for each of these topics, coupled models based on a pair or more of those aspects are still not so important. A major impediment is the high calculation complexity and cost that can be encountered on each level of the cardiac simulation [22]. Moreover, these models are generally based on particular assumptions that can prevent any general combination between the different characteristics of heart modeling [23], [23].

One of the important coupled model to described heart activity is the electro-mechanical model. Such model will enable to understand more clearly the interactions between the conductive and mechanical part of the cardiac muscle, allowing, for example to improve knowledge about the effect of a large class of drugs used in the management of cardiac arrhythmia.

1.2 Objectives

Based on this context, the general objective of this study aims to construct coupled electro-mechanical models for ventricular cells, enable to reproduce correct physiological results and

enable to offer a better understanding on the interactions between the electrical and contraction properties of the cardiac muscle. To this aim, the choice of those models was taken following the specific and main points:

- Simulate the major ionic currents implies on the ventricular cells.
- Reproduce the complete Ca^{2+} dynamics on the cell.
- Reproduce human ventricular data
- Enable to give correct muscle contraction response due to the calcium-dependent activation process.
- Computationally not too expensive

Based on these constraints, the choice of the ionic models have been focused on the ten Tusscher, Noble, Noble and Panfilov model (2004) and the Jafri, Rice and Winslow model (1998). The first ionic model is based on the description of different kind of human ventricular cells conduction dynamics and takes into account a large part of the ionic channel currents [24] present over the cardiac cell membrane. Nonetheless, the treatment of the calcium dynamics is oversimplified in this model. To overcome this weakness, a comparison was made based on the second model introduced. It has the particularity to take into account a complete description of the calcium dynamics between the intracellular and the sarcoplasmic compartments which plays a crucial role on the contraction activation.

The second aspect treated is to able to reproduce the mechanical behavior of the cardiac muscle by using a coupled model based on the crossbridges model given by Negroni & Lascano (1995) [18]. The main objectives of this second part is to able to reproduce the following key points:

- Time delay between the electrical and muscle response of the ventricular cell.
- Reproduce the results of the original Negroni Lascano model and general experimental observations over the contraction process.
- Simulate the mechanical contraction influence on the electrical activity of the cell (mechano-electric feedback).

Based on the simulated results obtained, we will attempt to understand and described the biochemical processes involved on the electrical conduction and mechanical contraction which distinguish the ventricular cardiac cells from other excitable or/and contractile cells.

1.3 Outline

This report is organized in 4 principal chapters. The first chapter introduce some biological and biochemical background require for the understanding of the simulation results that leaded to this study. A description of the mathematical models used to describe the conductive and the mechanical properties of cardiomyocytes is also presented in a second part of this first chapter. Finally, the basis and the principal hypothesis of the two coupled models implemented was described at the end of this first chapter.

The second one introduces the numerical schemes and code implemented used during the project to simulate the different results and in order to model the different electrical and mechanical pacing.

Chapter 3 focuses on the results obtained during all the simulations. The chapter is separated in two parts: one focuses on the ionic model simulation, while the second addresses to the results of the two ionic models coupled with the Negroni & Lascano model.

The last chapter, the Appendix, summarizes the different equations that describe the two ionic models together with the key parts of the C++ or Matlab code implemented during the study.

Chapter 2

Theoretical Background

2.1 Cardiac System

2.1.1 Circulatory System and Cardiac Anatomy

Heart is a hollow and muscular organ that enables the blood transport through the circulatory system to the different organs in a large part of living species. Even if some anatomical differences exist depending on the species, the major function of heart is always conserved. It acts as a mechanical pump that enables blood to irrigate the entire biological system, enabling the transport and the exchange of essential resources (such as nutrient and oxygen) for the metabolism and also the evacuation of waste produced in the body. However, its role and the function of the circulatory system does not stop as a simple means of transport, but acts in distinct part of the biological system. Some of their functions are summarized below:

- Nutrients and gas transport
- Intermediate of the endocrine system (hormone signalization)
- Immune system
- Temperature and pH regulation
- Homeostasis

In human heart (and in a large variety of vertebrate), the heart is composed of four compartments described in Figure 2.1: the right and left *atria* and *ventricles*. The two sides are separated physically by a muscular thick wall, called (atrio-ventricular) septum, which prevents a possible blood transfer between them. This separation is a key feature of the circulatory system, the blood, poor in oxygen, enters via different veins to the right atrium. By a system of valves, which opens under particular pressure conditions, the blood enters into the right ventricle which, by a mechanical force, expels it through the lungs in order to be re-oxygenated. In a parallel way the oxygenated blood coming from the lungs enters the left atrium by the pulmonary veins. From there, the blood enters the left ventricle, which its principal function is to send the blood to the entire biological system via the aorta. This coordinate transport is made any time without the possibility that oxygenated and non-oxygenated blood can mix together.

The major part of this contraction cycle is supplied by the two cardiac ventricles, which act as the real motor of the pumping process [13]. This fact explains the physiological difference that exists between them and the atria. The ventricles' walls are thicker than atria in order to exert a sufficient force to expels the blood into the entire circulatory system. This fact explains also the bigger size of the left ventricle compare to the right one, due to the fact that the left must

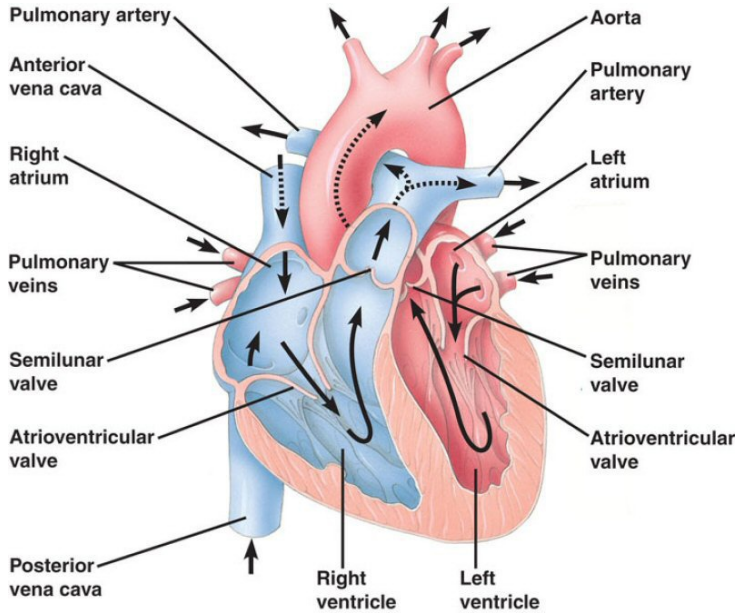


Figure 2.1: Human heart muscle anatomy [1].

force the blood to travel through the entire system, while the left only transport blood until the lungs.

All these functions are possible due to the spontaneous and rhythmic contraction activity of the cardiac muscle¹. During lifetime and in normal conditions, the heart will contract at an average frequency of around 72 beats per minute [25], with, almost, a constant and remarkable efficiency to pump the blood throughout the entire organism. This mechanical pump is initiated by contractions triggered by a cells' system specialized in electrical conduction, called *cardiomyocytes* (see Section 2.2.1). In vertebrate, the heart is constituted in majority of cardiac muscle and connective tissue [26]. Cardiomyocytes forms a multilayer muscle where each of tissue's level differs in a specific way in their conduction response (excitability, automatism and conductivity) and functions (pacemaker or contraction) enabling a coordinate contraction and therefore an efficient pump ability. Before taking to cells involved to the contraction part, let us focused on how the electrical signal is created directly on the heart.

2.1.2 Electrophysiology

All the system of blood transport and pumping of the heart is made possible, as it was said, by the rhythmic and coordinate contraction along all its muscle fibers. This coordination is allowed by a complex electrical system composed of specific cardiomyocytes presented in Figure 2.2.

The particularity of such system is to be able to excite spontaneously and almost independently of the neuronal electrical system [19]. However, this latter (and the endocrine system) can act on the electrical cardiac system through the autonomic system and enables to control the heart pacing (frequency and force) in some specific conditions, such as stress conditions or physical exercise.

The spontaneous electrical activity of the heart is allowed by a group of specialized cells called: *sino-atrial node*² (SA node) and *atrio-ventricular node* (AV node) [19]. Under normal conditions, the pacemaker signal is provided by the SA node and propagates throughout the right atrium to the AV node as it can be seen in figure 2.2. The connection between the visceral nervous system

¹It is said that the cardiac muscle is myogenic.

²Due to this physiological function, they are sometimes called heart's pacemakers.

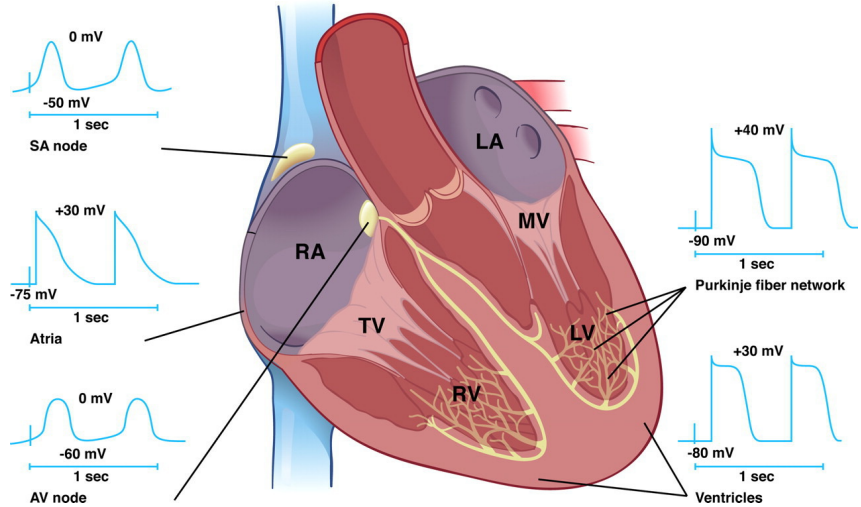


Figure 2.2: Conduction system of the human heart and specific potential profile [2].

and the conduction heart system is done by means of the SA node [19]. The electrical signal formation of such cells is formed by specific ionic channels that make the membrane potential (potential difference between intra- and extracellular space) not in a complete rest state, contrary to the other tissues (Fig. 2.2). Indeed, such kind of nodes presents a typical potential which is separated into two dynamical behavior: fast and slow potential increase [27]. This characteristic implies that after a rapid depolarization of the membrane potential, some specific channels still allow the diffusion of ionic species, preventing the potential to stay constant during some period of time. Those ionic currents depolarize slowly the membrane potential until it reaches some threshold value. When the depolarization rises this threshold, some of the closed ionic channels open and enable the transition to a rapid potential increase, triggering a new electrical pacemaker signal. The frequency automatism of such cells depends on various factors such as temperature, electrical signal from nervous system or drugs' effect [19].

In a second step, the signal reaches the AV node which is principal role, in normal conditions, is to decelerate the electrical influx from the SV node [28], [19]. This deceleration enables the system to synchronize efficiently the sequential contraction between the atria and the ventricles. The AV node transfers in a third step the signal to the two ventricles through the *Bundle of His* which divides into two branches (right and left) and terminating finally to the *Purkinje fibers*. These cells has the ability to conduct cardiac action potential rapidly and efficiently in order to create synchronized contractions of the ventricles. One cycle contractions ends finally with the repolarization (return to the initial electrical potential value) of the ventricles.

All the electrical system is constructed around a structured and connected pathways. Modifications or dysfunctions of such system induce a large panel of electrical diseases which leads to abnormal pumping activity of the heart and problems that can be associated. Arrhythmia or cardiac dysrhythmia regroups all the cardiac diseases which presents a cardiac rhythm different from the sinus one (created by the SA node). They are generally classified according to localization on the heart, their mechanism(s) and the benign or malignant nature [19]. Some of them are listed in Table 2.1.

Although many of those pathologies are still not completely well understood [29], [30], a large part of them are treated by drugs which acts directly on the biological membrane conductivity of the heart muscle cells. More specifically, they act on specific membranes proteins involved on the conduction system. This fact highlights the importance to create good ionic models that are enabled to capture physiological results in normal conditions. This constraint is a preliminary step in order to understand and postulates the physiological process that are involved in such

Name's Disease	Pathology	Localization
Premature Atrial Contractions (PACs)	Premature heart contraction	Atria
Atrial flutter	Abnormal heart rhythm	Atria
Supraventricular tachycardia (SVT)	Fast heart rhythm	Junctional
AV nodal reentrant tachycardia	Fast heart rhythm	Junctional
Ventricular fibrillation	Uncoordinated ventricles contraction	Ventricle
Ventricular tachycardia	Fast heart rhythm	Ventricle

Table 2.1: Some of the most common arrhythmia diseases and their localization [19].

pathologies. However, and before introducing the concepts associated to cardiac modeling, it will be important to describe how this electrical signal can propagate throughout the heart and which biological and biochemical processes are involved in order to have sufficient knowledge to catch the basic concepts that ionic models are based on.

2.2 Cardiomyocyte Structure and Biology

2.2.1 Muscular Cells

Classification and Morphology

In a large part of living species, the ability to move or the possibility to transport blood in the vessels are due to the existence of some particular cells that exhibits the ability to contract, called muscular cells. Generally, and in vertebrates, they are classified according to four different types: skeletal muscle, cardiac muscle, smooth muscle and myoepithelial cells (Fig. 2.3). The classification in these four groups depends on their respective structure or function in the organism. Whereas some of them are used to maintain the organs' tonicity, others are involved in a mechanical process which can be periodic or submitted to conscious control. Those differences lead generally to dissemblance in the contraction/relaxation times and in their reactivity against a electrical stimulus [31].

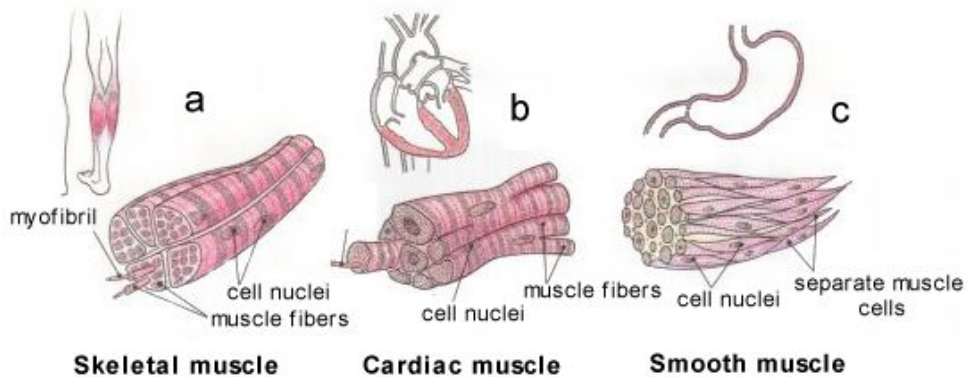


Figure 2.3: Different type of muscular cells [3].

Skeleton muscles, also called voluntary muscle, includes all kinds of muscle involved in locomotion, the global posture maintaining, articulations' stability and heat production of living species. Even if the control of the muscle is maintained by unconscious reflex, skeletal muscles react to conscious control of the central nervous system.

Smooth muscle composes a large part of the organs structure and they don't react to conscious control. It is generally linked to the autonomic nervous system and maintains well function of

particular organs.

Cardiomyocytes are particular muscular cells that compose the cardiac muscle (Section 2.1.1). They are part of the *myocytes* classification, which groups all muscular cells that contains only one nucleus, as it is the case of all muscular cells, except for skeletal cells, which are polynucleated.

One major difference between muscular cells is the presence or not of a sequence of dark and clear bands, visible under electronic microscope. Such kind of muscular cells are called *striated muscle* and regroups both cardiomyocytes and skeletal muscle. These bands are due to the presence of a particular proteic structure called sarcomeres which will be described in Section 2.2.1.

Cardiomyocytes

Structurally, cardiomyocytes are very closed to skeletal muscle. As for skeletal muscle each of them is constituted of a large number of myofibrils which possess a diameter between 1 and 2 μm [31]. Myofibrils are structured as a linear combination of sarcomeres which defines the space that separates each of the contractile system of myofibrils. More precisely, sarcomeres are particular arrangements of proteic filaments that are composed of many different proteins and give the elasticity properties of these cells, including the ability to contract or stretch. Each of the sarcomeres is delimited by extension of the plasma membrane of the cardiomyocytes which allows the connection between different myofibrils. These extensions, or more precisely invagination, are called T tubules or transverse tubules. Its crucial function is to enable the rapid transfer of the depolarization across all the cardiomyocytes which is necessary to the contraction mechanism. Around each sarcomeres and between T tubules, the myofibrils are covered by a specific endoplasmic reticulum called sarcoplasmic reticulum. It plays a specific role in the contraction system by providing a large amount of Ca^{2+} which is involved in the contraction mechanism.

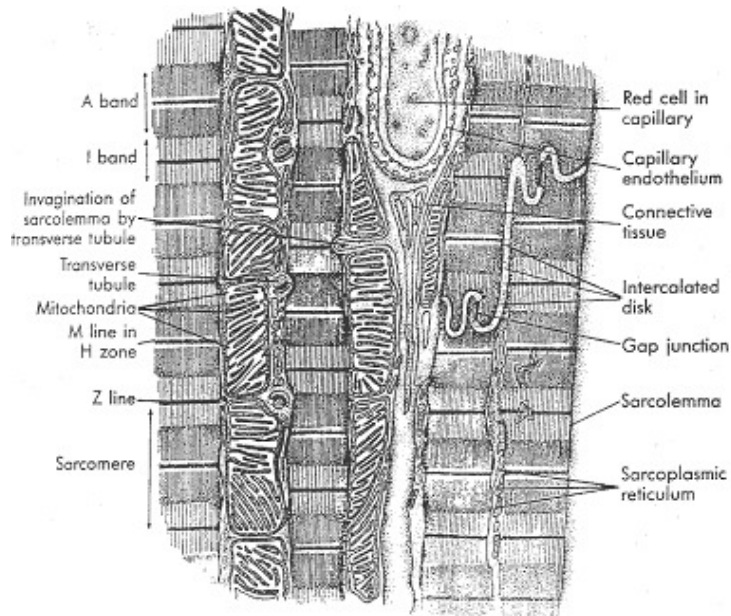


Figure 2.4: Anatomical structure of a cardiomyocyte [4].

Nevertheless cardiomyocytes possess some characteristics that makes them distinct of skeletal muscle. First at all, the length is much smaller. Its length is comprised between 50 and 100 μm and it has a diameter around 10 or 20 μm [31]. Secondly and from an histologic point of view, cardiac muscle cells differ from the skeletal muscle in the sense that they form a tridimensional network of connections between adjacent cells favored by the presence of bifurcations at the end

of each cell ([31], [32], intercalated disk in Figure 2.4). Skeletal muscle forms contrary very long muscle fibers, which can reach the length of the complete muscle. The connections are allowed by a system of specific junctions that provides a mechanical cohesion between myocardial cells and electrical coupling between each other. This important cell network allows the cardiac muscle cells to act as a functional syncytium even if, contrary to skeletal muscle fibers (which is a real syncytium³), they possess an unique nucleus. Finally, the heart function is always at work, therefore needing a large amount of energy to work properly. In this aim, the cardiac cells are generally rich in mitochondrion and glycogen, much more than skeletal muscle [33].

The contractile unit of the cardiomyocytes due to the structure of the proteic filaments presents a striated structure form by more or less dark bands associated to electronic density of the proteins revealed by electronic microscope (Fig. 2.5). As the figure presents, a sarcomere is delimited by 2 *Z lines* situated in the so called *I bands*, which defined the zone of small electronic density. In this region, the sarcomere presents a regular hexagonal disposition of thin filaments. These thin filaments are composed principally by three important proteins called *actin*, *troponin* and *tropomyosin*. In the dark region, called *A band*, another essential protein is found, called myosine. It composed by thick filament and presents also an hexagonal pattern.

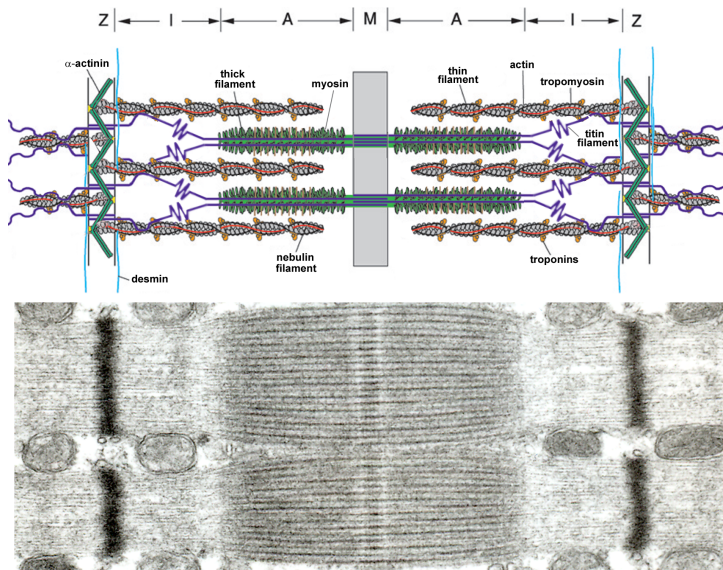


Figure 2.5: Biological structure of one sarcomere [5].

The thin and the thick filaments are linked to each other by biochemical bridges formed by extension of myosine proteins at regular space interval. These connections allow the formation of tension that leads to muscle contraction. Nonetheless, these bridges evolve in time by regulation of the chemical interaction mainly due to troponin and tropomyosin, regulated themselves by intracellular Ca^{2+} .

2.2.2 Membrane Structure

Cardiomyocytes as any living cell are an auto-reproductive system arranged around a specific structure called the plasma membrane. The plasma membrane is a thin lipid bilayer of about 5 nm [34] whose principal role is to separate the intra-cellular environment from the extra-cellular one. However, its role in the cell does not restrict to a simple border between these two environment. Indeed, during their growth and all lifetime, the membrane should allow the transport of chemical compounds necessary to the metabolism and it might be able to evacuate the waste products formed by vital reactions in the cell. In order to facilitate those exchanges,

³ Syncytium: Multinucleate cell [32].

the membrane possesses a certain permeability due to the presence of channels and pumps which might be very selective and composed by specific proteins in order to have a fine control on the transported components. Moreover, the plasma membrane plays an active role in the structural form of the cells. Indeed, due to its thickness, the cell membrane is extremely weak and to enhance mechanical stability, it is supported by specific proteins in the cytosolic space which formed a net called cellular cortex. It serves also as an anchor of the cytoskeleton which acts on the cell's shape and allows the formation of specific tissue by attaching proteins in the extracellular matrix [34].

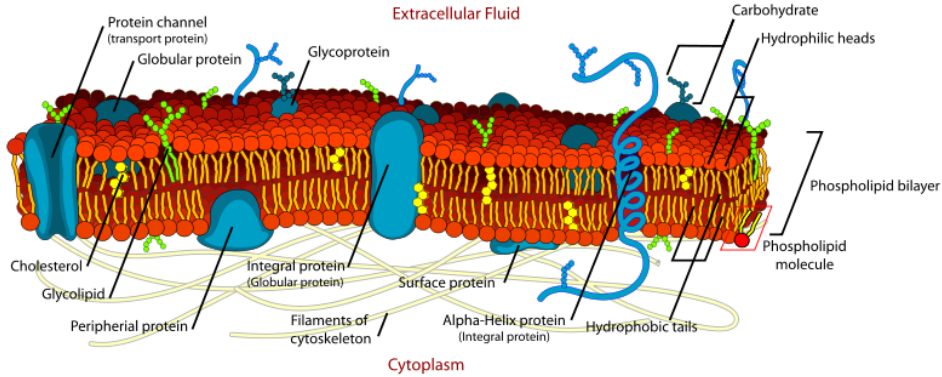


Figure 2.6: Typical structure of the cell membrane [6].

Nevertheless and as it was mention before, the most impressive property of the plasma membrane is its ability to form an active barrier that controls the entrance and the exit of any kind of molecules. By this molecular structure, the barrier that formed the membrane is relatively strong, and except for small or non polar molecules, prevents the diffusion of the molecules across the extra- and intracellular space as between the organelles and the intra-cellular space (Fig. 2.7)

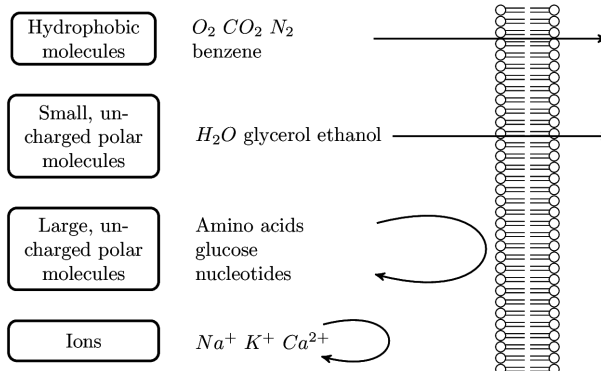


Figure 2.7: Scheme of the membrane's permeability. Hydrophobic and small uncharged polar molecules can cross the membrane passively or by non-specific pores. The presence of a charge in the molecule prevents any passage by simple diffusion.

As figure 2.7 presents, non polar molecules like linear gas molecules (O₂ or CO₂) can diffuse easily across the membrane. This is quite logical in the sense that those molecules are important in the cellular respiration processes and might be transported easily throughout the cell in order to maintain viable biological processes. Small polar but non charged molecules can also diffuse rapidly into the intracellular space if they are sufficiently small. Water and ethanol can diffuse rapidly across the membrane [34] while non charged amino acids or glycerol diffuse much slower across the lipid bilayer due to small membrane permeability. Finally, ionic species (like charged amino acids, glucose or nucleotides) cannot pass at all due to their charge and the strong interactions with water which forms a cage that prevents all passage across the

lipophilic environment of the membrane. Nonetheless, the cells have to transport rapidly inside or outside the cell all the chemical substances whatever their own chemical nature, which is impossible by simple diffusion. That is one of the reason why the cells develop the ability to control and select the chemical species that can pass across the membrane. For that, specific proteins called transmembrane protein channels and transporters, allow the cells to import and to export molecules, which is fundamental for the stability of the cells and the biological system they form. Endocytosis and exocytosis are other processes that allow the cells to overpass the transport between the interior and the exterior of the cell. This kind of transport process uses the properties of the lipid membrane in order to create a vesicle by invagination of the membrane helped by some specific proteins that enables the fusion of the vesicle with the plasma membrane.

The variety of proteins that are used by biological systems is very large and can have a very specific structure according to its function and position in the cell [34]. This particular chemical structure gives to those proteins the ability to be selective for a class of molecules or also to be specific of one kind of molecules or atoms (e.g. some trans-membrane channels are very selective of the ion's type and do not allow the passage of another ion, even if the charge is same, [34]). Those proteins can be separate in two major classes, mentioned above: *transmembrane protein channels* and *transporters* (Fig. 2.8).

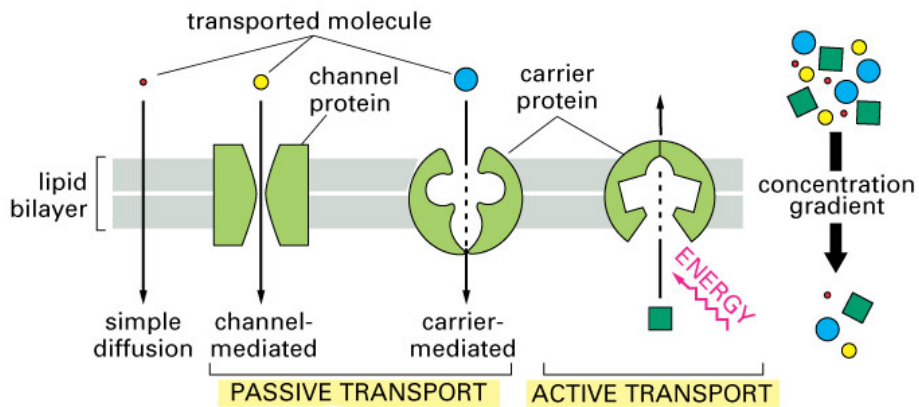


Figure 2.8: Proteins' class associated to transport in cell membrane [7].

Besides structural differences, the major distinction between the two transport membrane proteins' class is their ability to choose the molecules that are transported. The protein channels select the molecules according to their size and their charge. If the channel is open, the molecules will be transport passively and spontaneously across the membrane due to the electrochemical gradient (see Section 2.3.1) if the chemical properties of the molecule is adapted to the selective control of the channel. The *passive* transport defined the transport of molecules or ions without external energetic contribution. External means simply energy that is different from the chemical potential energy linked with the transported molecule. Otherwise, the transport is called *active* (Fig. 2.8). If the conditions are satisfied, the molecule will pass the membrane spontaneously in order to reach thermodynamical equilibrium state, minimizing the energy. The concept of thermodynamic equilibrium is an important aspect that might be explained in order to understand completely the transport of chemical species in the cell (see Section 2.3.1).

In the other hand, transporters selects the carried molecules by the presence of specific binding sites. If the chemical species is adapted to that site, the transporter brings inside or outside the cell the molecule one by one simply by changing its conformation. Contrary to protein channels, the transport can be passive or active. The energy contribution involved in the active transport can be of different nature: ATP, co-transporters, or light activation.

Channel Proteins

Channel proteins are transmembrane proteins that simply allow the passage of ionic species throughout the lipid bilayer by creating a hydrophilic channel in some specific conditions. The direction of such a transport depends exclusively on the electrochemical potential gradient of those ions.

Some of them present a relatively large diameter of opening and a small selectivity for substances. Generally this kind of proteins is not used as a primary transporter between extra- and intra-cellular, but rather in some specific organelles or tissues. It consists of two classes of channel proteins called *gap junctions* and *porins*. Gap junctions are channels specially designed to allow the communication between adjacent cells when it is particularly important to coordinate a particular metabolic system. For instance, the coordination in the transmission of electrical conduction in muscular cells is one of the biological mechanism that employs this kind of proteins (Fig. 2.9).

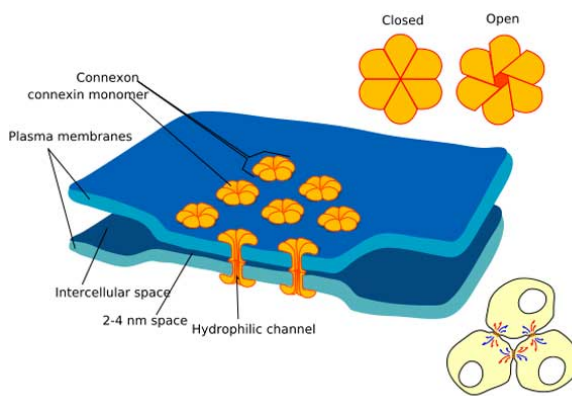


Figure 2.9: Gap junction strucutre [8].

Porins are proteins structured as a barrel, and composed of so called β -strands. By this specific structure, their selectivity is very poor and hence it is not generally used in communication between the two cellular sides separated by the membrane. One exception is the aqua-porine that can pass selectively water molecules and prevents passage of all ions. In vertebrate cells, the major use of porines can be found in the mitochondrial wall in order to transport rapidly the metabolites necessary to the respiration process.

Nevertheless, it is clear that such proteins cannot be used in a general manner in biological systems, otherwise the cells would not be able to control their environmental conditions leading to a disastrous cell death. In order to have the control over the distribution of ionic concentrations, biological systems have developed a large variety of channel proteins with very specific features. The variety of these channels is founded on many points. Firstly, the selectivity for one ion or more, depends on the protein structure of such channels. The chemical nature of the amine acids, their position and the size of the pore are some of the principal features that influence which type of ions can pass. Secondly, the possible mechanism that influence the opening of the channels can be very different: voltage, mechanical stimulus or binding-ligand activation are the major three classes that can be encountered in cells. However, and whatever the specific features of the channel, one point, that was mentioned just above, can be found on all these proteins, it is the property to be in two (eventually three) biological states: open and close (and sometimes inactivated⁴). Indeed, all the ionic channels have the property of not to be open permanently. Generally, the transition between open and closed state depends on the particular conformation

⁴This state can be found on many ionic channels implicated on the conduction system of muscular cells or neurons.

of the proteins and prevents that the concentrations of all ions reach an equilibrium state avoiding some important metabolic paths for the cells (e.g. glucose transport in the kidney). This control on the channel's opening allows the cell to maintain concentrations far away from the equilibrium ones. But it is important to note that the opening due to any activation does not mean that the channel is completely open, but only that the opening probability is increased due to the activation process [34]. Consequently, the channel oscillates between an open and a close state with a more or less probability according to the environmental conditions. The third state that can be found in some ionic channels, called inactive, prevents any possible diffusion and allows to some biological tissues to control more efficiently its electrochemical environment. This state is largely found on systems where electrical conduction is important as it was mentioned before [34], [31].

In cardiac muscle, the variety of ionic channels is very important and each of them allows the diffusion of specific ions with more or less control. In cardiac diseases, a large variety of drugs has as target, the control of a current through a given ionic channel [20], [35]. Most of them interfere with the opening of the channels allowing to reduce or increase the action potential duration (see Section 2.2.3). A list of the most common cardiac ionic channels in vertebrate are listed in Table 2.2. For each of them it was specified the type of activation, which kind of molecules can influence its state, the physiological role and more importantly, which kind of ions can pass across it. Moreover, in order to be consistent with the ionic model described in 2.4.2, the associated current name used is also mentioned.

<i>Current</i>	<i>Diffusive ions</i>	<i>Activation mechanism</i>	<i>Agonists</i>	<i>Blockers</i>	<i>Physiological Role</i>
I_{Na}	Na^+	Voltage (depolarization)	Non physiological <ul style="list-style-type: none"> • Aconitine • Veratridine 	Non physiological <ul style="list-style-type: none"> • Tocainide • Encainide • Flecainide 	<ul style="list-style-type: none"> • Upstroke of atrial and ventricular muscle action potential • Action potential plateau
I_{to}	K^+	Voltage (depolarization)	Physiological <ul style="list-style-type: none"> • α-agonists Non physiological <ul style="list-style-type: none"> • Capsaicin • Solatolol 	Physiological <ul style="list-style-type: none"> • Early repolarization phase (phase 1) 	
I_{Ks}	K^+	Voltage (depolarization)	Physiological <ul style="list-style-type: none"> • cAMP • β- & α-agonists Non physiological <ul style="list-style-type: none"> • Phorbol ester 	Non physiological <ul style="list-style-type: none"> • Amiodarone • Propafenone • Clofamilium 	Repolarization
I_{Kr}	K^+	Voltage (depolarization)	Physiological <ul style="list-style-type: none"> • See I_{Ks} • $[K_o^+]$ Non physiological <ul style="list-style-type: none"> • See I_{Ks} 	Non physiological <ul style="list-style-type: none"> • Dofetilide • Propafenone • Quinidine 	Repolarization
$I_{K,1}$	K^+		Physiological <ul style="list-style-type: none"> • K_o^+ 	Physiological <ul style="list-style-type: none"> • Na_o^+ • Ca_o^+ 	<ul style="list-style-type: none"> • Atrial and ventricular muscle resting potential • Rapid repolarization (phase 3) at end of action potential
$I_{Ca,L}$	Ca^{2+}	<ul style="list-style-type: none"> • Voltage (depolarization) • Ligand 	Physiological <ul style="list-style-type: none"> • β-agonists • cAMP • ATP • PKA, PKC, PKG (protein kinase) Non physiological <ul style="list-style-type: none"> • Atrotoxin • Tiacotoxin 	Physiological <ul style="list-style-type: none"> • $[Ca^{2+}]$ increase • Adenosine Non physiological <ul style="list-style-type: none"> • Nifedipine • Verapamil • Diltiazem 	<ul style="list-style-type: none"> • SA node: pacemaker potential • SA and AV node: upstroke action potential • Action potential plateau • Excitation-contraction coupling

Table 2.2: Principal cardiac ionic channels in vertebrate species [20].

Transporters and Pumps

Generally, and in order to transport solutes against their electrochemical gradient, the simple diffusion transport allowed by ionic channels is not sufficient. Indeed, due to the transport of compounds against its electrochemical potential, it is necessary to supply an external energy to allow the protein to transport the impermeant⁵ species. In cardiomyocytes, pumps are a crucial component of the stabilisation of the transmembrane potential and the possibility to the system to return to initial conditions after an electrical impulse and therefore to be ready for the next stimulus. The ability to maintain a constant and negative transmembrane potential depends on the ability of the cell to maintain mostly imbalance the concentration of Na^+ , K^+ and Ca^{2+} ions across the lipid bilayer, which is not possible by simple diffusion.

As it was said before the transport of molecules thanks to external energy is called active transport. The energy necessary for active transport can be provided by different pathways. A large majority of active transport in living cells is done by phosphorylation of ATP or other energetic storage molecules due to intrinsic kinase⁶ activity of the transporter ([34], Fig. 2.10). This pathway is part of the more specific active transport called *primary active transport* or *direct active transport*. It regroups all transporters which use directly energy supplied by chemical reactions or light activation to transport molecules across a membrane [34]. On the other hand, *secondary active transport* proteins, also known as *co-transporters*, use the electrochemical gradient of one specific molecule or ion in order to carry another compound in the opposite and not spontaneous direction (Fig. 2.10). As the Figure 2.10 presents, co-transporters are classified in two groups, antiporters and symporters, according to the relative direction of the transported compounds.

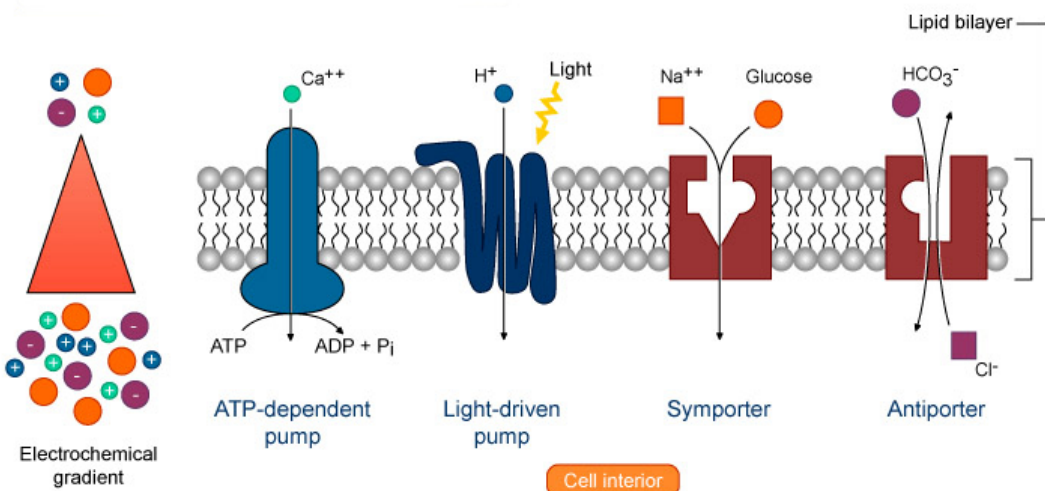


Figure 2.10: Active transport mechanisms [9].

In cardiomyocytes, Ca^{2+} -ATPase and Ca^{2+} -exchanger are some of the most important transporters that allow to maintain a low level of $[Ca_i^{2+}]$ and hence to be sensitive to intracellular calcium release, which is primordial to the contraction mechanism.

As for the ionic channel, a table which describes the principal pumps used in cardiomyocytes are described in Table 2.3. The current's name still be consistent with the ionic current's name

⁵ *Impermeant*: That cannot pass through a semi-permeable membrane.

⁶ *Kinase*: Enzyme type specialized on transfer of phosphate groups from high-energy donor molecules, such as ATP, to specific substrates.

in the models of Section 2.4.2. This time it includes not the type of activation but how the external energy is supplied.

<i>Current's name</i>	<i>Transported ions</i>	<i>Active type mechanism</i>	<i>Agonists</i>	<i>Blockers</i>	<i>Physiological Role</i>
	$3 Na^+ \text{ to } 1 Ca^{2+}$				
I_{NaCa}	$Na_o^+ \rightarrow Na_i^+$ $Ca_i^{2+} \rightarrow Ca_o^{2+}$	Normal mode Antiport	Physiological <ul style="list-style-type: none"> • MgATP • Ca_i^{2+} Non physiological <ul style="list-style-type: none"> • Concanavalin A 	Physiological <ul style="list-style-type: none"> • H^+ Non physiological <ul style="list-style-type: none"> • Lidocaine • Verapamil • Bepridil 	<ul style="list-style-type: none"> • Excitation-contraction coupling • Action potential plateau • Restore normal $[Ca_i^{2+}]$
I_{NaK}	$3 Na^+ \text{ to } 2 K^+$ $Na_i^+ \rightarrow Na_o^+$ $K_o^+ \rightarrow K_i^+$	ATPase	Physiological <ul style="list-style-type: none"> • MgATP Non physiological <ul style="list-style-type: none"> • Cardiac glycosides (nM) • α_1-adrenergic agonists 	Physiological <ul style="list-style-type: none"> • Ouabain • Digoxin • Bretylium Non physiological	<ul style="list-style-type: none"> • Pacemaker activity control of Purkinje fibers • Membrane potential maintenance
$I_{p(Ca)}$	$Ca_i^{2+} \rightarrow Ca_{SR}^{2+}$ or $Ca_i^{2+} \rightarrow Ca_o^{2+}$	ATPase	Physiological <ul style="list-style-type: none"> • MgATP • Ca^{2+}-calmodulin (PMCA) 	Physiological <ul style="list-style-type: none"> • Phospholamban (SERCA) Non physiological <ul style="list-style-type: none"> • Thapsigargin (SERCA) • Cyclopiazonic acid (SERCA) • Eosin (PMCA) • O-vanadate (PMCA) 	<ul style="list-style-type: none"> • Restore normal $[Ca_i^{2+}]$

Table 2.3: Principal cardiac ionic exchangers and pumps in vertebrate species [20].

2.2.3 Action Potential of Cardiomyocytes

Armed with the concept and the knowledge of the biological and physiological features of the cardiomyocytes, it was now possible to describe the generation and the evolution of the action potential triggered by the excitation of the electrical system.

Action potentials are important and rapid modification of the membrane potential which travels without modification along a particular conductive tissue. Even if the shape, the amplitude or its duration can vary between different kind of cells, its formation is fundamentally

identical [25]. Indeed, the action potential is a all-or-non electrical process. Following a electrical stimulation, the conductance of the membrane modifies due to different channel proteins which open due to a depolarization. If this depolarization is not strong enough compare to a critical value (called *threshold potential*), the cell returns rapidly to its initial conditions creating an aborted and local signal which does not trigger the different biochemical processes involves on the electrical conduction [34]. In contrary, if the electrical impulse leads to a sufficiently high depolarization, the cells react by forming an action potential, synonym of a rapid depolarization to positive values of the membrane potential. After a brief period, whose length depends on the cells' nature, the system returns to this initial membrane potential value, called *resting potential*.

In cells involved on the cardiac contraction, and principally in ventricle muscles, the evolution of the membrane potential is generally separated in five principal phases. The first one is associated to the normal conditions that lives the cell without the presence of an electrical signal. This phase, called *phase 4*, represents the resting membrane potential. The resting membrane potential in the human ventricular myocardium is around -85 and -90 mV ([36], [25], Fig. 2.11). In all conductive cells, the resting membrane potential depends strongly on the unequal distribution of ionic concentration on both sides of the cell membrane. Table 2.4 presents the principal ionic elements involved on the action potential formation and their respective distribution on the cell.

<i>Ion</i>	<i>Extracellular</i>	<i>Intracellular</i>
Na^+	135 - 145	10
K^+	3.5 - 5.0	155
Cl^-	95 - 110	10 - 20
Ca^{2+}	2	0.0001

Table 2.4: Intra- and extracellular distribution of ions in cardiac myocytes [13] The concentrations are given in mM.

This unequal distribution is enabled by two main factors: active transport proteins and the relative permeability of the membrane for the different elements. In normal conditions, the myocyte permeability is relatively important for potassium due to the presence of inward rectifier K^+ channels that are open at rest [35]. This explains the value of the resting membrane potential which are quite close of the reversal potential of K^+ (see Section 2.3.1).

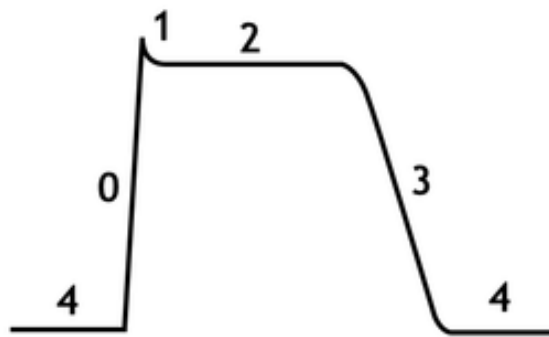


Figure 2.11: Five phases of the action potential [10].

Following an electrical stimulus coming from the pacemaker cells or external stimulation, voltage-dependent Na^+ potential open and enable a large release of sodium into the intracellular space due to high electrochemical potential of that ion. This leads to a rapid depolarization, and the so-called *phase 0* step. In some cardiac cells, a *phase 1* rapid repolarization ensues due to the opening of transient outward K^+ current (I_{to} , Table 2.2 [35]).

The *phase 2* is a very specific phase of the action potential on cardiac muscle cells [37]. It lasts generally around 100 ms and depends largely on a balance between inward calcium currents (largely by $I_{Ca,L}$ current) and delayed outward rectifier K^+ currents [37]. In vertebrates, the large release of Ca^{2+} ion is allowed by a particular structure (see Section 2.2.4) formed by the T-tubules. The duration of this *plateau phase* enables the system to be refractive to another stimulation, preventing uncontrollable contraction of the heart and loss on the pumping process [38]. For that reason, the duration of this phase is generally called *refractive period*. The refractive period is classified in two main parts defined as *relative* and *absolute* refractive period, which differs from the possibility or not to trigger a new action potential in some specific conditions.

Finally, after the refractive period, the L-type Ca^{2+} channel close while delayed rectifier current still stay open leading to a rapid repolarization of the membrane *phase 3*. Other K^+ currents such as inward rectifier activates during the phase 3, increasing even more the repolarization speed of the potential.

2.2.4 Contraction's Mechanism of Cardiomyocytes

The muscular contraction mechanism can be described by the early *sliding filament model* (1954, [31]). During one contraction of the sarcomere, it can be observed that the H band and the I band's width decrease while the distance between the Z disks, the H band and also the width of the A band are unchanged during the process (Fig. 2.12). These observations lead to derive the model where the two filaments slide in opposite direction with respect to each other without changing their respective length. The sliding of the two filaments is allowed by their specific orientation. While actin extends always from the Z disks to the H band, the myosin presents an inversion of orientation at the M disk ([31] Fig. 2.5). This specific orientation of the filaments implies that the myosin draws the actin to the center of the sarcomere.

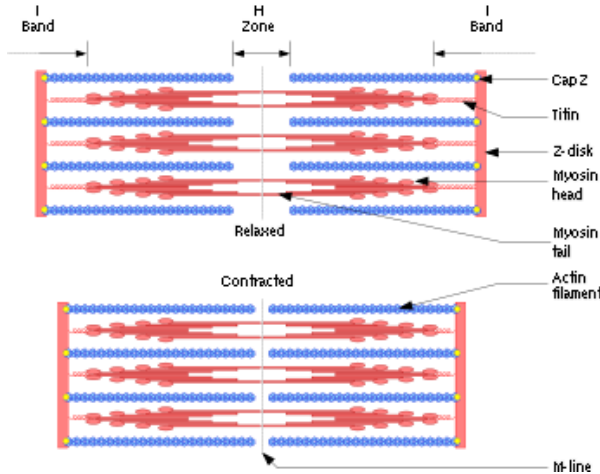


Figure 2.12: Scheme of the sarcomere contraction [11].

The mechanism of contraction is based on a biochemical cycle which depends especially on ATP and intracellular Ca^{2+} . ATP is the "fuel" that allows the myosin to slide across the thick actin filament. According to Figure 2.13, we can see that the energetic bond phosphate-ADP is broken by the ATPase activity of the myosin. When the contraction signal is given the myosin binds to actin molecules which promotes the liberation of the phosphate molecule. This detachment leads to a conformation's change which results to a net movement of the thick filament with respect to the thin one. The fixation of a new ATP molecule leads to a new cycle.

The signal used to activate the excitation-contraction cycle described above is controlled by the concentration's level of Ca_i^{2+} (intracellular calcium). The biochemical fluxes involved into the concentration level is desctried in Figure 2.14. When the electrical impulse of the SA node or the

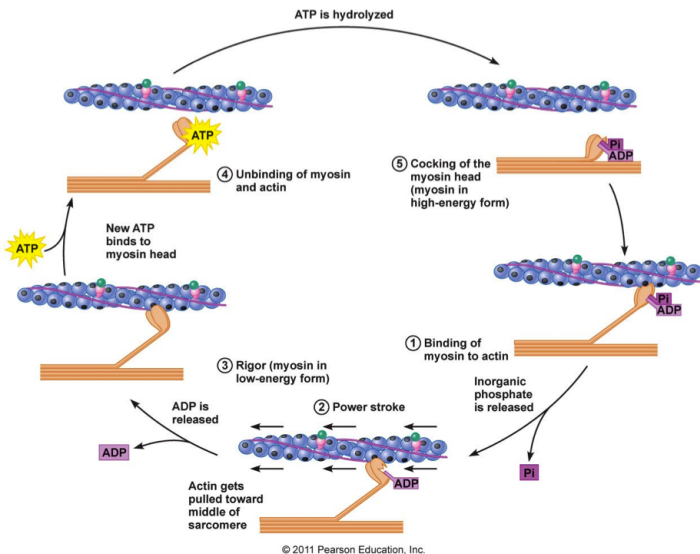


Figure 2.13: Scheme of the contraction cycle of the sarcomeres [12].

atrioventricular node is triggered, the electrical impulse cross the cardiac muscle cells throughout the T-tubules. This impulse leads to a rapid release of calcium which induces the muscle contraction. Each of the T-tubules forms with a single terminal cisternae of the sarcoplasmic reticulum a structure, called reticulum diad, where the two biological components are juxtaposed separated by a tiny space of around 15 nm the diad's junction [31]. This topology optimize the coupling between the depolarization impulse and a rapid release of Ca^{2+} . The release is possible due to some specific calcium channel that is encountered in the membrane surface of T-tubules and sarcoplasmic reticulum on the diad's junction. Two of them are particularly important. In the T-tubules, the dihydropyridin receptors are calcium voltage-dependent channel (also called, *L-type Ca^{2+} channel, $I_{Ca,L}$* in Table 2.2) which is deactivated by derivates of dihydropyridin, like nifedipine or bardipine ([20], Table 2.2). In the case of the sarcoplasmic terminal, the Ca^{2+} is released throughout a foot structure called *ryanodine receptor*. This structure is sensitive to the conformation change and calcium release of the dihydropyridin receptors promoting a rapid release of calcium of the reticulum. This coupling between the two channels are quite important in skeletal muscle, but also present in cardiomyocytes. In cardiac muscle cells a second mechanism, much more important, exists and consists of a massive calcium release triggered by the leak of calcium across sarcolemma channels. This kind of process are called *Ca^{2+} -induced Ca^{2+} release* (CICR).

Even if, we have described the entrance of Ca^{2+} more specifically, it remains to describe how these ions control the contraction of the sarcomeres. As it was described previously, the thin filament is composed principally of actin, tropomyosin and troponin. While the role of actin as support of the movement of the myosin was described, the role of tropomyosin and troponin have not been specified for instance. As the Figure 2.15 presents, the complex troponin-tropomyosin allows the regulation of the binds between actin and myosin. Tropomyosin is a hetero-dimer of homologous sub-units which formed a alpha-helical coiled col protein that lie along the α -helix groove of the actin filament (Fig. 2.15). Each of the hetero-dimer is attached by interaction with around 7 sub-units of the actin filament. Without Ca^{2+} presence, the troponin I prevents the interaction between the head of the myosin and the actin protein, by hiding the actin-myosin binding site, leading to muscular decontraction. Troponin C is the central protein associated to the control with respect to Ca^{2+} concentration. When the calcium ion binds to troponin C, it increase its affinity to troponin I, reducing in the same time the affinity of the latter with actin. This modification in the affinity induced a arrangement of conformation which moves all the

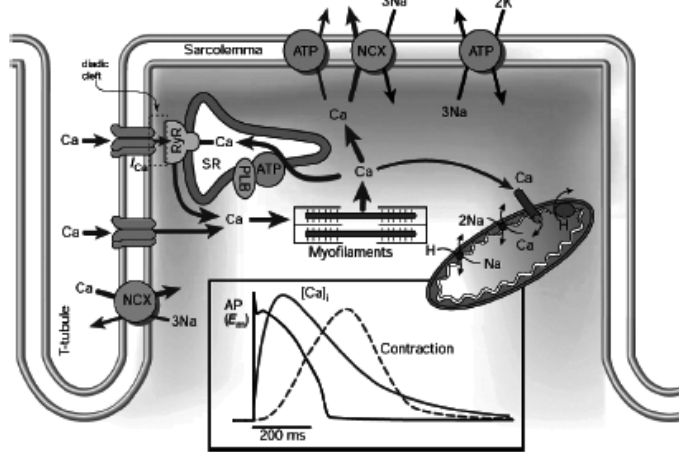


Figure 2.14: Biochemical system of Ca^{2+} fluxes involved on the electro-mechanical coupling. The different acronyms stands respectively for: RyR (Ryanodine receptor), NCX ($Na^{+}-Ca^{2+}$ exchanger, I_{NaCa} in table 2.3), PLB (phospholamban), and SR for the sarcoplasmic reticulum [13].

complex closer to the groove of the actin helix exposing the binding myosin-actin site, promoting the beginning of the contraction cycle described above.

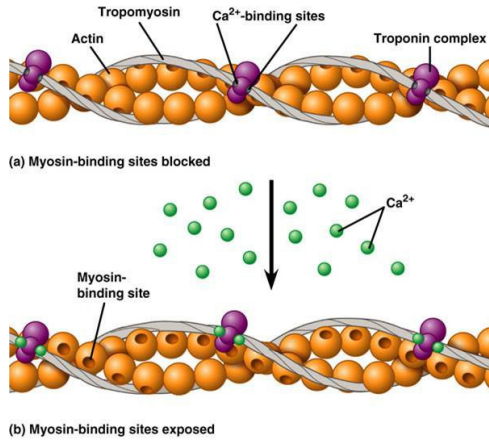


Figure 2.15: Scheme of the troponin complex of the thin filament and the effect of Ca^{2+} ion [12].

One major aspect of the electro-mechanical coupling is the delay on the time course between the different actors involved into this process, as it was presented in the inset of figure 2.14. The potential activates first, enables by voltage-dependent channels described previously to trigger a rapid increase of intracellular calcium concentration. Then the calcium ions binds to the troponin C liberating the binding sites of the thin filament, starting finally the muscular contraction. The delays between each step of the electro-mechanical coupling depends largely on the diffusion time of calcium through the intracellular space, and the calcium channel response to voltage modification. One of the main point of possible mechanical model is to be able to reproduce the correct sequence and time delay of the electro-coupling model.

2.3 Chemistry and Physical Background

2.3.1 Thermodynamics and Electrochemistry

In biological electrophysiology, the most important part of thermodynamic constraint is due to the electrostatic equilibrium. Indeed, the ions which play a crucial rule in the conduction propagation depends on the concentration and electro-neutrality between two sides of the lipid bilayer from an organelle or the extra and intra-cellular side. The electrochemical potential depends on two important parameters. The first one, the molar fraction, the concentration or any kind of value which measures the quantity. The variation in space of this parameter leads to a gradient which induces a diffusion of the ionic compound in order to reach an equilibrium state. The second one is the equilibrium of charges or more precisely the distribution of species that are electrically charged. Inhomogeneity in charges distribution leads to form an electrical potential which tends to induce a displacement of that particles which is more or less easy according to the conductivity of the solution. The conduction property of the muscular cell (also of the nervous cell) is provided by the fact that there exists a transmembrane potential at rest which is maintained in time by the system of ionic pumps. Indeed, a biological system is never at thermodynamic equilibrium, and large part of the energy consumed is used in order to maintain the state of the cell outside the equilibrium one. One of the important quantity that it uses for describing the state of a chemical system is the chemical potential. The chemical potential is the variation of a state function (like free energy U or enthalpy H) with respect to number of molecules variation. The state function used depends strongly on the experimental conditions. Generally, its common formulation is given with respect to Gibbs free energy (see Section 2.1).

$$\mu_i = \left(\frac{\partial G}{\partial n_i} \right)_{T,p,n_j \neq i} \quad (2.1)$$

An important use of the chemical potential is to compute some particular relations for equilibrium of a chemical system. In a solution, with charged species, the common chemical potential used is called electrochemical potential and has the form given in equation [39]:

$$\tilde{\mu}_i = \mu_i + z_i F \phi \quad (2.2)$$

We will now introduce some of concepts which are crucial to understand completely the dynamics of the implement ionic models and to justify the use of some specific relations.

Migration on solution

As it was said, the displacement of charges in a biological system depends strongly on two parameters, the electrical potential and the gradient of chemical potential. The molar flux is described by the phenomenological law [39]:

$$\vec{j}_i = -c_i \tilde{u}_i \vec{\nabla} \mu_i - z_i F c_i \tilde{u}_i \vec{\nabla} \phi - c_i \tilde{u}_i \vec{V}_i \vec{\nabla} p \quad (2.3)$$

Consequently, the migration of a particular compounds depends on the gradient of the chemical potential, the pressure's gradient and on the gradient of the electrical potential. The diffusion is a particular type of migration which depends only on thermal energy and the concentration. Based on (2.3), the flux for diffusion is simply given by the first term of the sum and can be written as:

$$\begin{aligned} \vec{j}_i &= -c_i \tilde{u}_i \vec{\nabla} \mu_i, \text{ where } \mu_i(\vec{x}, T) = \mu_i^\ominus(T) + RT \ln(c_i) \\ &= -\tilde{u}_i RT \vec{\nabla} c_i \end{aligned} \quad (2.4)$$

The equation (2.4) is commonly called 1st Fick's law which states that the diffusion flux is proportional to the gradient concentration. However, in conduction system like the muscular cells, the ions' fluxes across the membrane does not depend uniquely on gradient concentration. The use of the formulation (2.4) is valid if the membrane potential of the cell does not affect the diffusion of the ionic species. In other cases, we might include the gradient potential term of (2.3) giving rise to the Nerst-Planck equation:

$$\vec{j}_i = -\tilde{u}_i RT \vec{\nabla} c_i - z_i F c_i \tilde{u}_i \vec{\nabla} \phi \quad (2.5)$$

This equation with the relation (2.4) are the two principal relations that described the ionic transport in biological systems and explain their large use in the fundamental equations of the ionic models.

Nernst Equation

One of the most important aspect in electrophysiology studies is the concept of reversal potential. The reversal potential is a specific value of the membrane potential where the transmembrane flux of a particular ionic sort is equal to zero [40]. This value is characteristic of a given ionic channel or more generally of an ionic current as it was described in Table 2.2. The reversal potential depends strongly on both the distribution of ionic species in each side of the membrane and their respective permeability in some cases. The relation that link the parameters with this particular potential can be computed by different way. One of them is related to the Nernst equation, which is a mathematical formulation that it quite known in electrochemistry.

Indeed, in the point of view of redox reactions, Nernst equation is a mathematical formula which allows to determine the redox potential at equilibrium of some redox couple with respect to a standard potential (see (2.6)).

$$E = E^\ominus + \frac{RT}{nF} \ln \left(\frac{a_{Ox}^x}{a_{Red}^y} \right) \quad (2.6)$$

In the case of electrophysiology, the Nernst-like equation used to describe the reversal potential is derived by a simple ionic transfer equilibrium between two phases. The derivation of this equation is described in equation (2.7), the indexes ((1), (2) and \ominus resp.) describes in which phase the species i is located and the fact that it is evaluated at standard state respectively [39].

$$\begin{aligned} \text{At equilibrium } \tilde{\mu}_i^{(1)} &= \tilde{\mu}_i^{(2)} \\ \mu_i^{\ominus,(1)} + RT \ln \left(a_i^{(1)} \right) + z_i F \phi^{(1)} &= \mu_i^{\ominus,(2)} + RT \ln \left(a_i^{(2)} \right) + z_i F \phi^{(2)} \\ \phi^{(2)} - \phi^{(1)} &= \frac{\mu_i^{\ominus,(1)} - \mu_i^{\ominus,(2)}}{z_i F} + \frac{RT}{z_i F} \ln \left(\frac{a_i^{(1)}}{a_i^{(2)}} \right) \\ &= \Delta_{(1)}^{(2)} \phi_i^\ominus + \frac{RT}{z_i F} \ln \left(\frac{a_i^{(1)}}{a_i^{(2)}} \right) \end{aligned} \quad (2.7)$$

The value $\Delta_{(1)}^{(2)} \phi_i^\ominus$ in (2.7) is called the standard transfer potential. The similarity between equations (2.6) and (2.7) explains finally the terminology of Nernst potential for the reversal potential.

One drawback of the Nernst equation in order to compute the reversal potential is the fact that this relation is valid uniquely for system where the conductance depends only on one unique ion. Is for that reason, that the reversal potential is considered as a synonym of equilibrium potential for a single-ion system [39], [41]. This assumption is quite true for system where the

conductance or the permeability of the membrane for one ion is quite important with respect to others [41].

In systems where there are more than one ion involved, the reversal potential cannot be considered as a equilibrium potential. Indeed, in those systems, most (and in some cases, all) ions are not in equilibrium and have a net non zero fluxes across membrane. In this case, the reversal potential has the sense of the value at which the total current flux changes its direction. In that cases, the Nernst-like potential cannot be used in order to find the membrane potential for some biological system, and explain why some measurements are not in accordance with the computed value from (2.7). When a cell, more specifically a channel protein, is permeable to more than one ion, the cell potential is calculated by the Goldman-Hodgkin-Katz equation rather than the Nernst equation.

However, and before talking about Goldman-Hodgkin-Katz relation, it is important to mention one important aspect of the membrane potential in a Nernst-like condition system and the concept of Donnan potential.

Donnan Equation

By the composition of the electrolyte solutions in both sides of the cell membrane and its permeability to that ions many ions tends to be restricted to one phase of the biological system. This restriction, especially important for large ionic proteins, leads to develop an uneven distribution of the diffusible ions between the internal and external solution for each cell. Indeed, by thermodynamics consideration, the ionic species tends to equalize their electrochemical potentials in both side of the membrane inducing an osmotic and an electrical potential difference. The Donnan (or Gibbs-Donnan) equilibrium is therefore defined as the equilibrium condition described above. Hence, it can be considered as a particular case of the equation (2.7). Indeed, by considering an equal chemical potential between the two sides and by the fact that the standard chemical potential can be considered as equal since the solvent is the same between the two cellular sides, we can derive the Donnan potential (2.8).

$$\begin{aligned} \mu_i^{\ominus,I} + RT \ln(a_i^I) + z_i F \phi^I &= \mu_i^{\ominus,O} + RT \ln(a_i^O) + z_i F \phi^O \\ \mu_i^{\ominus,I} &= \mu_i^{\ominus,O} \\ E_{\text{Donnan}} = \phi^I - \phi^O &= \frac{RT}{z_i F} \ln \left(\frac{a_i^I}{a_i^O} \right) \end{aligned} \quad (2.8)$$

According to (2.8), it can be shown that the product of the concentration of pairs of diffusible ions on one side of the membrane equals that product on the other side. Indeed, in order to maintain electroneutrality in each solution, the equilibrium potential (Donnan) has to be equal for two ionic species with opposite sign leading to an equal but opposite sign current between this ionic pair. This has the consequence that the concentration of the particules is not equal in each side of the membrane. This phenomenon is called Donnan exclusion and largely due to the non-permeability of the membrane for some ions. When one particular ion cannot diffuse throughout the membrane, it leads to reduce the diffusion of ions with opposite charge while ions that charge are the same is favoured.

The Donnan exclusion induces large consequences in the ionic distribution of living cells creating the so-called membrane potential [42]. Moreover, the unequal distribution of proteins, sugars and other charged chemical compound leads to create a large osmotic pressure which would induce the sweling and the rupture of the cell if it was not counteract by active transporters like $\text{Na}^+ \text{-K}^+$ pump or $\text{Na}^+ \text{-Ca}^{2+}$ exchanger.

Goldmann-Hodgkin-Katz Equation

The drawback of the Nernst-like potential in order to compute the reversal potential is primarily due to the fact that it was only concerned with the presence of one ionic specie. It is well known that the membrane potential depends not only on the equilibrium potential of an unique ion but rather a composition of those potentials. The Goldmann-Hodgkin-Katz equation was implemented in order to take into account that the conductance of a particular cell (and consequently its potential) depends on the presence of more than one ionic compound, which Nernst equation does not succeed to capture. In the GHK equation the ionic conductivity of each species depends strongly on their respective membrane permeability. As for Nernst equation, several assumptions are made in this particular model [40], [42], [41]

1. The membrane potential behaves like a linear function across the membrane. In other words, the electric field is a field with direction perpendicular to the membrane and with constant norm (constant-field theory, Fig. 2.16).
2. The phenomenological equation is still valid across the membrane
3. All the ions' fluxes are independent of each other.

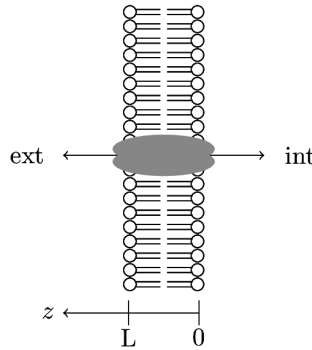


Figure 2.16: Scheme describing the potential membrane assumption used in GHK equation.

From phenomenological equation (2.3) and the scheme 2.16, we can write:

$$\begin{aligned} j_i &= -\tilde{u}_i RT \frac{dc_i}{dz} - c_i \tilde{u}_i z_i F \frac{d\phi}{dz} \\ &= -D_i \left(\frac{dc_i}{dz} - \frac{z_i F V_m}{RT L} c_i \right) \end{aligned} \quad (2.9)$$

In the equation (2.9), the \tilde{u}_i is the membrane molar mobility and z_i the charge number of the ionic specie i . By resolving this first order ODE and by defining the permeability P_i as D_i/L , we can find the GHK flux equation (also called *constant-field* equation, [41]):

$$j_i = P_i \frac{z_i F V_m}{RT} \frac{c_{out,i} - c_{in,i} \cdot e^{\frac{z_i F V_m}{RT}}}{1 - e^{\frac{z_i F V_m}{RT}}} \quad (2.10)$$

The GHK equation looks for the value of the reversal potential, i.e. the value of the membrane potential where the total current of the ionic species fall to zero. As the density current from the i -th species is defined simply by $J_i = q_i \cdot j_i$, the total current can be computed and we find that:

$$J_{tot} = \sum_i J_i = \sum_i q_i j_i = \sum_i z_i^2 P_i \frac{c_{out,i} - c_{in,i} \cdot e^{\frac{z_i F V_m}{RT}}}{1 - e^{\frac{z_i F V_m}{RT}}} = 0 \quad (2.11)$$

In the case, where the system is composed only by monovalent ions, the equation 2.11 can be written in terms of the potential as:

$$\sum_i P_i \frac{c_{out,i} - c_{in,i} \cdot e^{\frac{FV_m}{RT}}}{1 - e^{\frac{FV_m}{RT}}} = 0 = \sum_i P_i c_{out,i} - e^{\frac{FV_m}{RT}} \sum_i P_i c_{in,i}$$

$$V_m = \frac{RT}{F} \ln \left(\frac{\sum_i P_i c_{out,i}}{\sum_i P_i c_{in,i}} \right) \quad (2.12)$$

As it can be seen, in the case of a unique ion conductance ($P_i = 0$ for all $i \neq j$), the GHK equation reduced to the Nernst like equation of the Donnan potential (2.8). Moreover, contrary to (2.8) equation, the reversal potential depends not only on the relative concentration of the ion across the membrane but also on the membrane permeability of that specific ion. The GHK potential is sometimes used in the description of the reversal potential of some ionic current when the associated channel is permeable of more than one pair of ionic species [40], [42], [41].

2.4 Mathematical Description

2.4.1 Macroscopic Cardiac Models

Introduction

According to the previous chapter, and based on the theoretical knowledge developed, it is possible to build a mathematical model in order to simulate the electrophysiology of the heart. The goal of these mathematical model is to catch and understand the dynamic of the electrical conduction throughout the cardiac muscle based on the knowledge of the electrical conduction at the cell level. They provide consequently essential tools in order to increase the knowledge of bioelectrochemical phenomena occurring at the level of the cardiac tissue. This objective constitute the so-called *forward problem of electrocardiology* [22]. The motivation of developing such kind of models are important and goes from a deterministic interpretation of the electrical conduction and propagation from the cell level until the whole body scale including the coupling between the different part that constituted the heart. The solution of such problem allows in a final step to validate the simulation according to physiological data obtained from specific patients and thereby understand more clearly possible pathological response in the ECG or others clinical methods. In a completely different perspective, it is possible to construct a model which can extract relevant parameters of the cardiac conduction based on body-surface potentials obtained via the ECG of a patient. This perspective forges the basic principle of the *inverse problem of electrocardiology* [22]. The advantage of the inverse problem against the forward one is that the sources of the electrical activity of the heart must not be known in advance to compute the potential at the heart level. The development of these ionic sources, which constitute the base of the *ionic models* brings a part of artificiality and approximation that can not be used directly in a clinical perspective. Nonetheless, the forward problem enables to link the electrical cardiac sources with the resulting cardiac bioelectric response that can be measured with medical examination.

Nowadays the mathematical description of the heart in the forward problem reference is principally based on two principal mathematical orientation: the *discrete* model where the cardiac tissue is represented explicitly as a combination of individual cells and the *continuous* cardiac model which the mathematics are based on the syncytium behavior of the myocytes [22], [23].

The discrete cardiac model groups a large panel of methods from *cellular automaton*, where each cell of the tissue is simplified as an object that lived in a finite number of states, to the *coupled map lattices* where the states of the cells are continuous [22]. In all of the discrete models,

the cardiac tissue is represented as a lattice of cells where live in an unique state on a particular time. The transition of one particular cell to a new state depends on interactions with neighbors states on the lattice through their previous configurations. The major advantages of this kind of models is to compute correctly the heterogeneity's effects on the electrical propagation or to enable to model anisotropy in the electrical conduction and propagation [22]. Consequently it can take into account, for example, variations in the distribution of gap junctions or in the sizes of the cells' extracellular space. Furthermore, this approach makes possible to create models where effect at the cell level can be examined easily [22]. However, it is generally a difficult task for such kind of methods to describe the global dynamics properties of the tissue's conduction such as rate-dependent effects. Further, some of these automaton includes the electrical kinetics at the cell level through coupled ODEs (ionic models) and can lead to extensively computational cost in order to solve numerically the model.

Another widely accepted model of the electrical activity of the heart is the continuous cardiac model. This macroscopic model focused on the hypothesis that the cell can be viewed as two conducting media which constitute the intracellular solution, which includes the cardiac cells, and the extracellular medium, representing the interstitial space between the cells. The two domains are considered as ohmic conducting media and separated through the lipidic membrane of the cell. The term *continuous* of that model arises to the homogenization process that allows the intra- and extracellular space to form an overlapping and continuous domain which occupy the whole heart volume Ω [22]. This is justified by the fact that the cardiac tissue, by its biological structure, acts as a functional syncytium 2.2.1. This hypothesis on the construction of the heart domain compose the *bidomain approximation* or *bidomain model*. From the homogenized system, the mathematical model allows following averaged intra- and extracellular variables such as the current densities ($\mathbf{j}_i, \mathbf{j}_e$), the conductivity tensors ($\boldsymbol{\sigma}_i, \boldsymbol{\sigma}_e$) and the electrical potential ϕ_i and ϕ_e , which are defined in all the heart domain [23].

From these two ohmic media, the dynamics of those variables can be formulated mathematically by a system of partial differential equations (PDEs). Consequently, the relationship between all those variables are defined with the mathematical formulation given by (2.13).

$$\mathbf{j}_i = -\boldsymbol{\sigma}_i \nabla \phi_i, \quad \mathbf{j}_e = -\boldsymbol{\sigma}_e \nabla \phi_e \quad (2.13)$$

The tensors in equations 2.13 are computed according to the anisotropy of the heart muscle and each components is therefore a function of the conductivity and the local orientation tissue. Then, by using the charge conservation law and assuming that ionic source is related uniquely to cell membrane, we know that the following relations are valid [22]:

$$\begin{aligned} \nabla \cdot (\mathbf{j}_i + \mathbf{j}_e) &= 0 \\ \nabla \cdot \mathbf{j}_i + A_m \left(C_m \frac{\partial_t V_m}{\partial t} + i_{ion}(V_m, w) \right) &= I_{stim} \end{aligned} \quad (2.14)$$

Where $V_m \doteq \phi_i - \phi_e$ represents the membrane potential, A_m is the surface area-to-volume ratio, C_m the cell surface capacitance and I_{stim} stands for the applied stimulus current to the system. As it can be seen from (2.14) equation, i_{ion} is a function of the membrane potential together with w which represents the cell level' *states variables* which includes generally ionic concentrations or/and channel gating variables [43]. These variables are generally coupled with a system of ODEs which can be written in a general formulation by the equation (2.15).

$$\frac{\partial w}{\partial t} + g(V_m, w) = 0 \quad (2.15)$$

The choice of the g and i_{ion} functions depends then of the ionic model implemented. We will focus on ionic models and their definitions in the next subsection. Finally, by a simple

combination of equations (2.13), (2.14) and (2.15), we can derive the *isolated bidomain model* which is composed of a system of ODEs coupled via PDEs, which regroup a nonlinear reaction-diffusion equation and an elliptic equation.

$$\begin{aligned} A_m \left(C_m \frac{\partial_t V_m}{\partial t} + i_{ion}(V_m, w) \right) - \nabla \cdot (\boldsymbol{\sigma}_i \nabla V_m) - \nabla \cdot (\boldsymbol{\sigma}_i \nabla \phi_e) &= I_{app} \text{ in } \Omega \times [0, T] \\ \nabla \cdot (\boldsymbol{\sigma}_i \nabla V_m) + \nabla \cdot ((\boldsymbol{\sigma}_i + \boldsymbol{\sigma}_e) \nabla V_m) &= 0 \text{ in } \Omega \times [0, T] \\ \frac{\partial w}{\partial t} + g(V_m, w) &= 0 \end{aligned} \quad (2.16)$$

Where Ω represents the whole heart domain while $[0, T]$ stands for the simulation time interval. Associated to this PDEs, suitable boundary conditions is based on assuming a zero-flux in the potentials [40] along the normal outward direction of the boundary $\partial\Omega$.

$$\begin{aligned} \boldsymbol{\sigma}_i \nabla V_m \cdot \mathbf{n} + \boldsymbol{\sigma}_i \nabla \phi_e \cdot \mathbf{n} &= 0 \text{ on } \partial\Omega \times [0, T] \\ \boldsymbol{\sigma}_e \nabla \phi_e \cdot \mathbf{n} &= 0 \text{ on } \partial\Omega \times [0, T] \end{aligned} \quad (2.17)$$

One important approximation used to simplify the differential equations' system (2.16) is based on the *monodomain approximation*. This approximation assumes that the conductivity between intra- and extracellular are proportional [40], [22], leading to decouples the computation of V_m from that of ϕ_e . The new system of differential equations are therefore given by (2.18).

$$\begin{aligned} A_m \left(C_m \frac{\partial_t V_m}{\partial t} + i_{ion}(V_m, w) \right) - \nabla \cdot (\boldsymbol{\sigma} \nabla V_m) &= I_{app} \text{ in } \Omega \times [0, T] \\ \frac{\partial w}{\partial t} + g(V_m, w) &= 0 \\ \boldsymbol{\sigma} \nabla V_m \cdot \mathbf{n} &= 0 \text{ on } \partial\Omega \times [0, T] \end{aligned} \quad (2.18)$$

The monodomain model is an appropriate approximation in a large part of simulated propagation systems [22], and by its simplicity, explains its large use in simulation. However, this model does not catch the correct influence of ϕ_e into V_m and cannot be applied in systems where the stimulation current is done into the extracellular space.

Numerical analysis

In order to solve the coupled system of PDEs and ODEs that constitue the bidomain model, the choice of the numerical integrator is particularly important. One of these integrator that is suited for the resolution of bidomain model's solution is provided by the finite element (FE) method. The popularity of these method in electrophysiological simulation are principally due to its ability to handle derivative boundary conditions and to be applicable in system with irregular geometries as it is the case with the heart organ. However, the principal difficulties to solve the problem is the coupled PDEs and ODEs system that must be solved in a parallel manner. The computation of the solution follows a basic scheme which is reproduced in Figure 2.17.

At each time step, the numerical computation of the differential problems needs to construct the tensor conductivities of each media in order to solve the voltage part by FE method. Through the membrane potential, the cell model dynamics, defined from equation (2.15), couples with the PDEs system and might be solved by different ODE solver, where the choice depends on both computational cost or stability purpose. From time updated states variables the ODE system couples back to the PDEs given in (2.16). Back coupling of cell model to the PDEs system can be computed by a variety of ways, where each of them tends to different effects on the

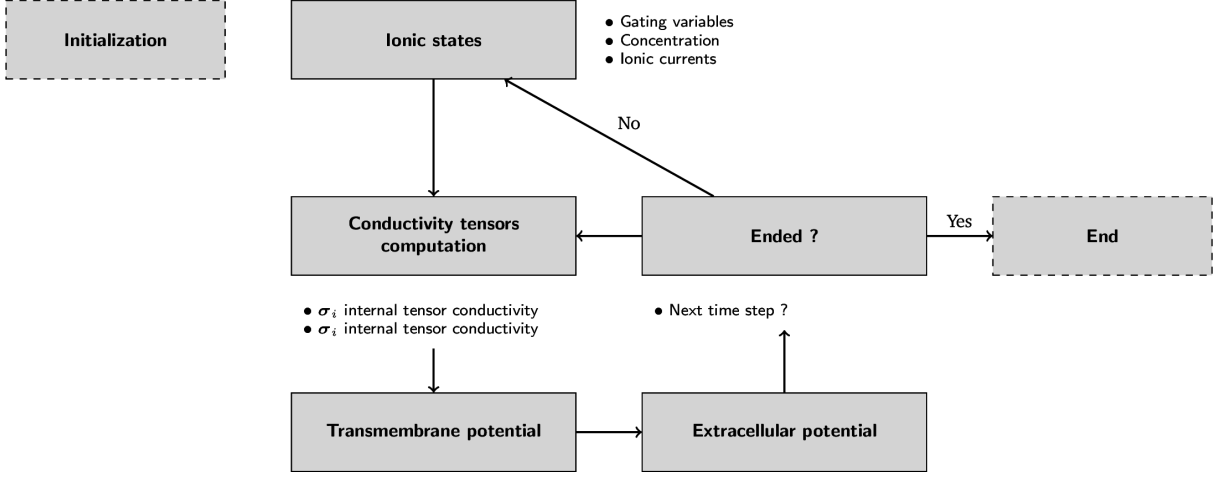


Figure 2.17: Numerical scheme associated to electocardiac simulation [14].

results of the electro-cardiac simulation [44]. In all the cases, the choice of the method depends strongly on an equilibrium between precision and computational cost. The two main procedures to compute ionic model solution can be based either on (a) an evaluation at each node of the FE mesh or (b) on each quadrature point in the interior of the polyhedra elements of the space discretization. Due to expensive computational cost of the method (b), a large part of cardiac modeling tends to use the first method, where conceptually the cells model is represented on each space node [44]. Commonly, in basic FE numerical scheme of the bi- or monodomain model needs the computation of integrals by quadrature methods which increase the numerical computation of problems (2.16) and (2.18). However, the computation of those integrals needs to know the value of some variables at each quadrature node. To avoid this problem, the main solution is introducing some interpolation approaches that will approximate the variable into the interior of each element. In order to clarify, this point let's introduce the FE and time discretization of the monodomain model (Eq. (2.18) without applied current. The FE space discretization transform the monodomain equation to relation

$$\int_{\Omega} A_m C_m \frac{\partial V_m}{\partial t} \phi_j - \int_{\Omega} \sigma \nabla V_m \cdot \nabla \phi_j = \int_{\Omega} A_m i_{ion}(V_m, w) \phi_j, \text{ for } j = 1, \dots, N, \quad (2.19)$$

where the ϕ_j form a piecewise linear basis function associated to their respective nodes \mathbf{x}_j , and that satisfies $\phi_j(\mathbf{x}_i) = \delta_{ji}$ where δ_{ji} is the Kronecker delta. Considering the membrane potential directly on the nodal values $\mathbf{V}_m = (V_{m,1}, \dots, V_{m,N})'$, the weak form (2.19) can be written as:

$$\int_{\Omega} A_m C_m \frac{\partial V_m}{\partial t} \phi_j - \sum_{i=1}^N \int_{\Omega} V_{m,i} (\sigma \nabla \phi_i) \cdot \nabla \phi_j = \int_{\Omega} A_m i_{ion}(V_m, w) \phi_j, \text{ for } j = 1, \dots, N, \quad (2.20)$$

Using a semi-implicit scheme, based on backward difference formula (BDF) for time discretization, the weak form monodomain equation (2.20) can be written as a linear equation:

$$A \mathbf{V}_m^{n+1} = \mathbf{F}^{n+1}. \quad (2.21)$$

Where, the matrix A and the vector \mathbf{F}^{n+1} are defined for $j = 1, \dots, N$:

$$\begin{aligned} A_{ij} &= \int_{\Omega} \frac{A_m C_m}{\Delta t} \phi_i \phi_j - \int_{\Omega} (\sigma \nabla \phi_i) \cdot \nabla \phi_j \\ F_j^{n+1} &= \int_{\Omega} A_m \left(\frac{C_m}{\Delta t} V_m^n - i_{ion}(V_m^n, w^{n+1}) \right) \phi_j \end{aligned} \quad (2.22)$$

As it can be seen from (2.22), the computation of the F vector needs to know the reaction term i_{ion} in the interior of each space elements. To this goal, two principal approaches was implemented: the *ionic current interpolation* (ICI) and the *state variable interpolation* (SVI). In both of those methods, the main approximation is to consider an interpolation of some variables on particular space points. The ICI method is based on a linear interpolation on the nodal values used for the FE approximation. The interpolation method uses the same basis functions as for V_m to define the ionic current (2.23). On other hand, it is V_m and w to be interpolate at the interior of the element.

$$\begin{aligned} i_{ion}^{ICI}(\mathbf{x}) &= \sum_{i=1}^N i_{ion}(V_m^n, w^{n+1}) \phi_i(\mathbf{x}) \\ i_{ion}^{SVI}(\mathbf{x}) &= \sum_{i=1}^N i_{ion}(V_{m,SVI}^n(\mathbf{x}), w_{SVI}^{n+1}(\mathbf{x})) \phi_i(\mathbf{x}) \end{aligned}$$

Where,

$$\begin{aligned} w_{SVI}(\mathbf{x}) &= \sum_j w_j \phi_j(\mathbf{x}) \\ V_{m,SVI}(\mathbf{x}) &= \sum_j V_{m,j} \phi_j \end{aligned} \quad (2.23)$$

Each of those methods possesses some specific advantages and drawbacks that makes them complementary. While, SVI is a more accurate approximation of the ionic current, its large computational cost, due to non-linearity of $i_{ion}(V_m, w)$ (2.15), prevents a direct utilization of that model in all cases. For the ICI case, its computational efficiency makes it a practical choice for the resolution of such problems, even if the precision is much lower than SVI [44]. This problem can lead to difference on physiological results like conduction velocity (CV) or action potential shape [44]. Consequently, the choice among those methods depends generally on the complexity of the ionic model used [44].

Other methods exists in order to compute the coupled PDEs and ODEs system, one important of the most important is the *operator splitting*. This technique separate the ionic term from the PDEs in order to get much simpler expressions, more easy to compute numerically. The advantage of this technique is that enables the use of different numerical integrators for each expression, increasing the computational efficiency. Nevertheless, this technique suffers of a lack of accuracy due to the fact that the dependence between variables are not simultaneously enforced [44].

2.4.2 Ionic Models

General Scope

In order to simulate the complete cardiac tissue, it is necessary to have a mathematical model that reproduces at best the cardiac cell's membrane ionic behavior, the term i_{ion} in the equations (2.16), (2.18). A model which can capture a large part of the conduction'ventricular properties

such as the ionic currents, the AP duration and restitution, or the calcium transient without being computationally expensive would be optimal. Further, the ionic model combined with the equations of isolated heart modelling might reproduce important features on the wave propagation like conduction velocity (CV) and conduction velocity restitution (CVR).

To this goal a large number of models have been implemented reproducing with more or less complexity and realism the conduction of cardiac muscle cells based on different physiological data obtained in various living species (generally mammals in the most recent ones, [22]). In all cases, all ionic models are based initially in the early model implemented on the research of A.L. Hodgkin and A.F. Huxley in 1952 in squid giant axon [15]. The basic principal of their mathematical model is to represent an excitable cell with a biophysically analogue electrical circuit [15]. The lipid bilayer and the channel proteins involved are schematized by a capacitance and respectively a conductance (linear or non-linear, depending on the nature of the channel protein) in the circuit. All ionic pumps are symbolized by current sources. Figure 2.18 presents the original electrical circuit used by Hodgkin & Huxley to describe the conductivity in the squid giant axon.

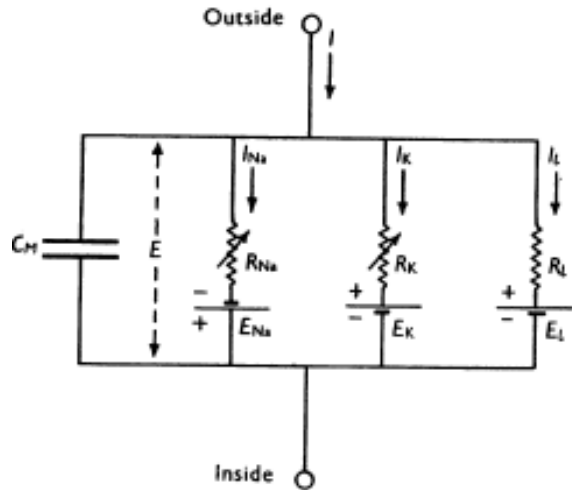


Figure 2.18: Original electrical circuit used by Hodgkin & Huxley to represent the membrane [15].

In the general case, a large part of the analogous circuit elements are functions dependent on both time and membrane potential, which will be different according to the biochemical nature of the transported ion and on the class of the transporter protein [15]. Therefore, and since the work of Hodgkin & Huxley, all the components of the circuit are summarized in a single term I_{ion} by summing together all the currents which take place at the membrane potential. In this manner it was possible to compute the membrane potential of a single cell thanks to the formulation (2.24)

$$\frac{dV_m}{dt} = -\frac{I_{ion} + I_{Stim}}{C_m}, \quad (2.24)$$

where I_{Stim} acts as an external stimulus that induce the triggers of an action potential when it reaches the threshold potential of the cell and C_m stands for the cell surface membrane capacitance [40]. Consequently, and exploiting this first mathematical model, a large number of different cell models have been implemented which are based more or less on biophysical features (*phenomenological* and *physiological* models). The evolution of these models has generally been followed by an increase of the complexity level. Starting from the Hodgkin & Huxley model with three currents (I_{Na} , I_K , I_L) and three gating variables (m , h , n) [15], nowadays some of recent models possess more than 20 different variables, including ionic currents, fluxes, subcellular space

and ionic concentrations. For example, one of the chosen model in this work and implemented by Jafri Rice & Winslow (1998) tracks 30 time-dependent variables solution of a dynamic problem which contains 4 ionic pumps, 10 channel proteins, 2 fluxes and 4 subcellular spaces ([45], Fig. 2.21).

But before introducing the two models implemented, let's focus on the basic Hodgkin & Huxley model to introduce some terminology that are typically encountered in ionic models. As mentioned before, Hodgkin & Huxley dissociated the ionic currents (I_{ion} , (2.16) and (2.18)) in three components: I_{Na} , I_K and I_L . Generally, in much more complex models, each ionic current is associated with a specific channel protein or transporter existing in the muscular cell that is simulated (see Tables 2.2 and 2.3). However, for phenomenological models, the currents represent only the current carried by its respective ion. The I_L current defines a *leakage* or *background* current, in other words a current that is carried by unspecified ions [15]. One important feature that will be found in all following models, is the fact that the ionic currents are described by the product of the conductance G_i and the difference between the transmembrane potential and the resting potential (2.25).

$$I_i = G_i (V_m - E_i), \text{ where } i \text{ is the associated current subscript.} \quad (2.25)$$

Equation (2.25) is quite general and can be used both for voltage-dependent ionic channels and for leak channels. The reversal potential on equation (2.25) depends on the specific permeability of the channel as it was explained in Section 2.3.1. In the case of a single ionic species permeability, the equilibrium potential can be described by Nernst-like equation (2.8). On the other hand, with permeability to more than one ion, the GHK equation (2.12) is used instead.

The conductance of the specific ionic current depends mostly on the nature of activation of the channel. Since the work of Hodgkin-Huxley, voltage-dependent ionic channels are represented by nonlinear electrical conductances, meaning that the conductance G_i is a function of time and voltage. In order to describe the temporal dependency, Hodgkin and Huxley introduce the concept of *gating variables*, which will be denoted as y . Those variables are based on the concept that ionic channels state depends on an opening probability which increases with specific environmental conditions. In the Hodgkin-Huxley formalism the conductance variable can be described by the relation (2.26).

$$G_i = \bar{G}_i \cdot \prod_{j=1}^{n_i} y_j^{\alpha_j}, \text{ where } \alpha_j \in \mathbb{N}^*. \quad (2.26)$$

Here \bar{G}_i is the maximum conductance and y_j corresponds to the j -th gating variable. Each of them is dynamically related to the ODE (2.27).

$$\begin{aligned} \frac{dy_j}{dt} &= \frac{y_{j,\infty} - y_j}{\tau_{y_j}} \\ &= \alpha_{y_j} (1 - y_j) - \beta_{y_j} y_j, \\ \text{where } y_{j,\infty} &= \frac{\alpha_{y_j}}{\alpha_{y_j} + \beta_{y_j}} \text{ and } \tau_{y_j} = \frac{1}{\alpha_{y_j} + \beta_{y_j}}. \end{aligned} \quad (2.27)$$

According to (2.26) and (2.27), it can be seen that to describe correctly the open and close state, the ionic current may require more than one gating variable. These variables, which describe a probability, are consequently bounded between 0 and 1. Indeed, where G_i depends only on one gating variable y_i , the ionic channel's state depends directly on y_i . When $y_i = 0$, the probability value indicates that the ionic channel is closed and the current will drop to zero. On the other hand, the conductance reaches its maximum value (\bar{G}_i) and the associated ionic current's value will evolve according to the difference between the transmembrane potential and

the reversal one. In more complex conductance relations, as (2.26), the ionic current will evolve according to the relative value of each of the gating variables that can be defined in order to catch, for example, the activation or inactivation kinetics of the channel [40]. The exponent α_j is generally obtained in order to fit correctly the kinetics of the channel against experimental data. Leakage current I_L in Hodgkin & Huxley model or other type of ionic channel, which are not voltage-dependent, are described by linear electrical conductance. In linear conductance regime, the current follows exactly the Ohm's law and consequently the conductance G_i is constant (noted generally \bar{G}_i in order to keep the same notation as in (2.26)).

In most of the ionic models, the constants that specify the dynamics of the gating variables are typically related to empirical formula based on interpolation of experimental data. These ODEs are usually in the mathematical form given by one of the two right hand sides of (2.27). In the perspective of the first right hand side, the equation tells us that the evolution of the gating variable is only a deviation of the steady-state of the variable given by $y_{j,\infty}$. The aptitude of the gating variable to return to that variable is expressed by the time constant τ_{y_j} .

Even if the Hodgkin-Huxley model was implemented in order to express mathematically the electrical behavior of a nerve fiber, it lays the foundation of the future models used to describe neuronal, cardiac or muscular conduction. The new models created are largely based on the mentioned work and it is not astonishing to find mathematical relations quite identical with this model. To increase the knowledge of this conductive system and in order to capture good physiological results, additional currents are implemented. In this work, two particular models are used in order to simulate the cellular membrane of cardiomyocytes of the ventricle: the model of Jafri, Rice & Winslow (JRW, 1998 [45]) based on data of guinea pig and the ten Tusscher, Noble, Noble & Panfilov model (TNNP, 2004, [24]) based on human ventricular cells (epicardial, endocardial and M cells). In the next sections, the basic hypothesis of those models will be introduced, the employed currents will be described and a schematic presentation of the cell will be given according to the specific model.

ten Tusscher, Noble, Noble & Panfilov model

The ten Tusscher, Noble, Noble & Panfilov model is one of the very few models focused on results obtained from human ventricular cells. Moreover, it has the special particularity to reproduce the electrical behavior of three special kind of ventricular cells: the epicardial, the endocardial and the M cells (also called subepicardial cells, [46]). M cells are special ventricular cells situated between the endocardial and epicardial layer (Fig. 2.19) and which differ on their electrophysiology and pharmacology characteristics [46].

To this goal, they propose a model composed of 12 different ionic currents (Table 2.5) the time evolution of 12 gating variables $y = \{m, j, h, X_{r1}, X_{r2}, X_s, d, f, f_{Ca}, r, s, g\}$, and 4 ionic concentrations $[X^{z+}] = \{[Ca_i^{2+}], [Ca_{SR}^{2+}], [Na_i^{2+}], [K_i^+\}$.

Figure 2.20 presents a schematic view of the ventricular cells used in the ten Tusscher & al. model, summarizing all the different elements introduced. The detailed equations of this model can be found in the Appendix part.

The principal point of the scheme in Fig. 2.20 is that the calcium system is modeled by a phenomenological formulation. Firstly, all the buffers are assembled in two categories whatever their chemical nature: Bu_{fC} for the cytoplasmic part and the Bu_{fSR} for the sarcoplasmic reticulum. Secondly, the L-type Ca^{2+} channel is described as a phenomenological relation (2.28) inspired by the Luo-Rudy phase II (LRII) model.

$$I_{Ca,L} = G_{Ca,L} \cdot d \cdot f \cdot f_{Ca} \cdot 4 \frac{VF^2}{RT} \frac{[Ca_i^{2+}] e^{\frac{2VF}{RT}} - 0.341 [Ca_o^{2+}]}{e^{\frac{2VF}{RT}} - 1}. \quad (2.28)$$

This formulation allows describing the dynamics of L-type channel correctly while maintaining a low complexity [24]. The activation and inactivation process of the L-type Ca^{2+} is described

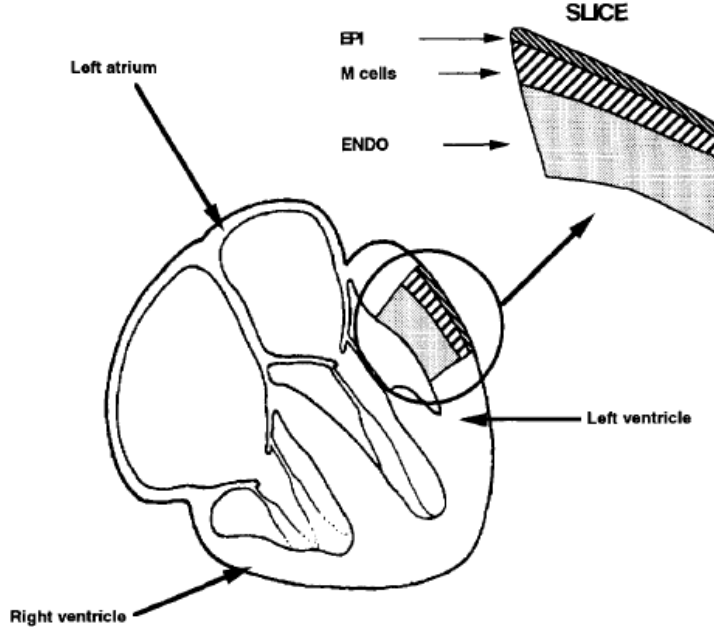


Figure 2.19: Representation of the heart organ with a slice of the ventricular muscle and the respective proportion of different cells [16].

simply by means of three gating variables: d (resp. f) stands for a voltage-dependent activation (resp. inactivation) gate while f_{Ca} models the intracellular calcium-dependent inactivation [24]. Each of these variables are described by a Goldmann-Hodgkin-Katz formulation (equation 2.27, see Appendix) where the parameters y or τ_y are fitted according to recent data from human ventricular cells [24]. The incorporation of the f_{Ca} term is crucial to simulate correctly the inactivation process of $I_{Ca,L}$. Indeed, some experiments show that the slow inactivation time have dependence both on voltage and extracellular calcium concentration [35]. For this reason, the ten Tusscher & al. model assumes that the inactivation process depends on these two variables and it can be modeled as a simple product of purely Ca^{2+} -dependent (f_{Ca}) and a purely voltage-dependent part (f). Moreover, the inactivation part is constructed in order to make the calcium the dominant mechanism of $I_{Ca,L}$ [24]. Although some of the ionic models also incorporated the small permeability of the channel to Na^+ and K^+ , here is ignore to only for sake of simplicity [24]. The calcium-induced calcium-release process (represented as J_{rel} in Appendix) has been described also by a simple phenomenological equation.

Contrary to the LRII or the JRW models, TNNP incorporates a complete description of the potassium currents separated into four different ionic channels (table 2.5, equation (2.29)).

$$\begin{aligned}
 I_{to} &= G_{to} \cdot r \cdot s(V - E_K) \\
 I_{Ks} &= G_{Ks} X_s^2 (V - E_{Ks}) \\
 I_{Kr} &= G_{Kr} \sqrt{\frac{[K_o^+]}{5.4}} X_{r1} X_{r2} (V - E_K) \\
 I_{K,1} &= G_{K,1} \sqrt{\frac{[K_o^+]}{5.4}} X_{K1\infty} (V - E_K)
 \end{aligned} \tag{2.29}$$

As presented in Table 2.2, all these ionic channels are voltage-dependent. Consequently, all the gating variables employed in those channels are functions of membrane potential only. All of them are described by a GHK formalism seen in (2.27). In order to simulate correctly the

<i>Current</i>	<i>Description</i>	<i>Current</i>	<i>Description</i>
I_{Na}	Fast inward Na^+ current	$I_{K,1}$	Inward rectifier K^+
I_{to}	Transient outward current	I_{Kr}	Rapid delayed rectifier current
I_{Ks}	Slow delayed rectifier current	$I_{Ca,L}$	L-type Ca^{2+} current
I_{NaCa}	Na^+/Ca^{2+} exchanger current	I_{NaK}	Na^+/K^+ pump current
$I_{p(Ca)}$	Sarcolemmal Ca^{2+} pump current	I_{Kp}	Plateau K^+ current
$I_{Ca,b}$	Background Ca^{2+} current	$I_{Na,b}$	Background Na^+ current

Table 2.5: Ionic currents used in the TNNP model (2004).

conduction dynamics for the different cells, some of these currents presented a difference in the dynamics of the gating variable or/and in their maximal conductance. This is the case of I_{to} current, where the voltage-dependent inactivation gate s is treated differently between epicardial (which include also the M cell) and the endocardial cells. Indeed, Nabauer & al. [47] shows that the parameters gate (s and τ_{Xs}) display a significant difference according to the type of cell. For I_{Ks} ionic channel, only the parameter G_{Ks} differs between the endocardial/epicardial myocytes and the M cells. This is done in order to get the right APD prolongation for the M cell which is longer than the other two [36]. Ten Tusscher & al model includes also the dependence of the channel to extracellular potassium through the $\sqrt{\frac{[K_o^+]}{5.4}}$ term in I_{Kr} and $I_{K,1}$.

Finally, the other currents are simply based on the original LRII model, so we refer the reader to [24] to more information.

Jafri, Rice & Winslow model

Jafri, Rice and Winslow model (JRW) is one of the model focused on the ventricular cells' conduction data for guinea pig. It has the particularity to be one of those models that coupled a detailed mathematical model for the Ca^{2+} regulation with the mathematical description of the membrane cell [45]. Contrary to ten Tusscher & al. model, the JRW model does not used a phenomenological model in order to simulate the Ca^{2+} subsystem, and particularly to modelize CICR process (Section 2.2.4). This is an important point, if you want to simulate correctly the possible effect of drugs on the Ca^{2+} channels encountered in the sarcoplasmic reticulum.

JRW model is based principally on the mentioned Luo-Rudy Phase II model [48]. The LRII model describes the electrophysiology of a ventricular cell for mammalian species (principally on guinea pig results, [48]). One of the principal innovation of this model is to include a simple mathematical model that reproduce the calcium-induced calcium-release process [45], which explains the choice for a base model in the JRW work. From this model, JRW introduces some modifications in order to construct a physiological model of the calcium regulation. The principal modifications are the following [45]

- LRII L-type Ca^{2+} current is modified to include mode-switching behavior [49]
- LRII calcium SR release mechanism is altered with the Keizer-Levine RyR model with adaptation.

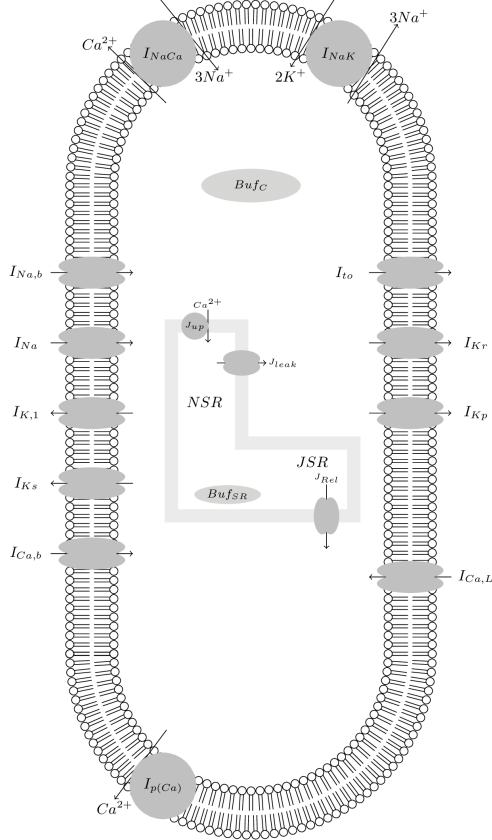


Figure 2.20: Scheme of the cell used in the ten Tusscher, Noble, Noble & Panfilov model. Each of the ionic current and the subcellular space are presented. The Buf_C resp. Buf_{SR} represented the buffer molecules situated in the cytosolic resp. sarcoplasmic reticulum compartments.

- A new subcellular space (called SS) was introduced. It serves as a representation of the restricted subspace located between the SR and the T-tubules. Moreover, the L-type Ca^{2+} channel release the calcium in that region and not directly in the cytoplasm in accordance with various anatomical researches [45].
- Takes into account the presence of some Ca^{2+} -buffer in the system, including the presence of troponin-sites of high and low affinity.

Due to this modification, some of the LRII ionic currents are just rescaled in order to preserve the physiological ionic concentrations and the action potential shape. As a large part of those currents are identical to the LRII model and the ten Tusscher & al model, we do not spend time to discuss them one more time. We will focus instead in the following paragraphs in the Ca^{2+} subsystem which is the main point of the model.

All the variables and the mentioned modifications just before are summarized in the scheme 2.21. As it can be seen, the Ca^{2+} system is much more complex than the ten Tusscher & al. model. In the previous model, the calcium is confined in two principal part: the sarcomplasmic reticulum and the myoplasm, and therefore, only two dynamical variables are necessary to describe the Ca^{2+} evolution. In the JRW case, the system is separated in four non-equivalent subspaces. Non-equivalent means the these regions differs in their chemical composition, their volume and also in the presence of some specific ionic channels. The sarcoplasmic reticulum is treated as two compartments: the junctional (JSR) and the network (NSR) sarcoplasmic reticulum. These compartments serve principally for the buffering of calcium ions by calsequestrin. In the model, the Ca^{2+} enters via the NSR into the sarcoplasmic reticulum and diffuse to the

JSR following a monoexponential function ([45], [48], equation 2.27). The calcium release, after electrical stimulation, occurs then in the JSR part.

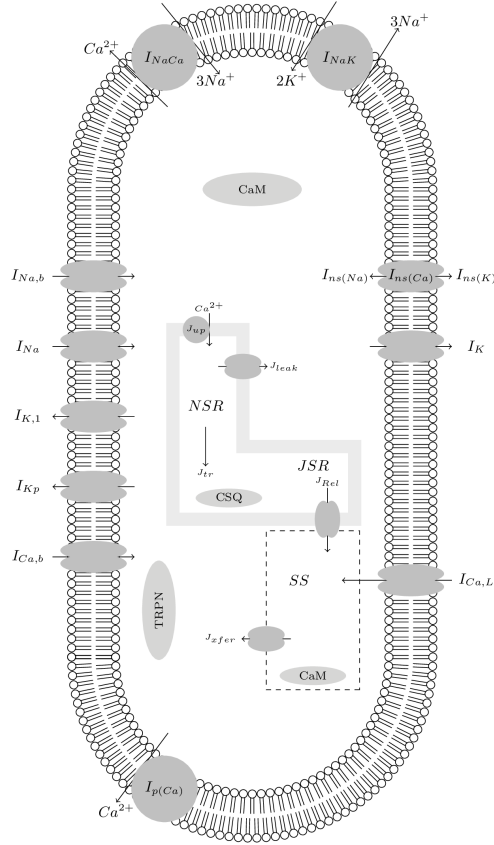


Figure 2.21: Scheme of the cell used in the Jafri, Rice & Winslow model (1998). Each of the ionic current and the subcellular space are represented. The *TRPN*, *CaM* and *CSQ* defines the three kind of buffers: troponin, calmodulin and calsequestrin.

From the complex scheme 2.21, the JRW stimulates the conduction cardiac cell by means of a system of 22 differential equations highly coupled, which includes:

- Gating variables:
 - L-type Ca^{2+} channel: $C_0, C_1, C_2, C_3, C_4, O, C_{Ca0}, C_{Ca1}, C_{Ca2}, C_{Ca3}, C_{Ca4}, O_{Ca}$
 - Na^+ current: m, h, j
 - K^+ current: x
 - RyR channel: $P_{C1}, P_{C2}, P_{O1}, P_{O2}$
- Ionic concentration:
 - Intracellular sodium: Na_i^+
 - Intracellular and extracellular potassium: K_i^+, K_o^+
 - Calcium subsystem: $Ca_i^{2+}, Ca_{NSR}^{2+}, Ca_{JSR}^{2+}, Ca_{ss}^{2+}$

The mathematical details of the model could be find in the APPENDIX part in the respective section.

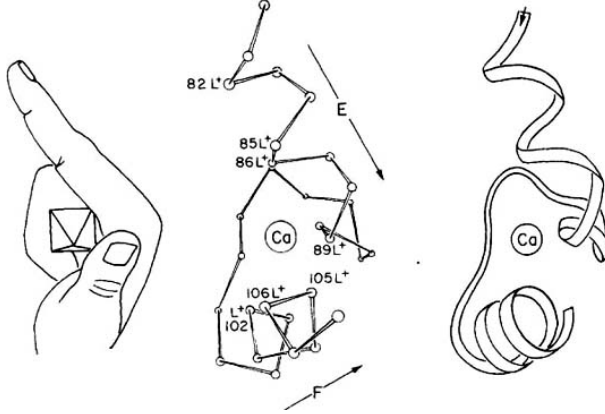


Figure 2.22: Protein structure of the EF hand calcium-binding domain with hand representation.

L-type Ca^{2+} channel Some of the recent studies have shown that the inactivation of L-type channels is mediated by the local calcium concentration which binds in a site of the channel which presents a motif EF-hand (REF, Fig. 2.22).

This inactivation leads the channel to switch from a normal mode characterizes by dense bursts of activity to a mode Ca where the probability to change from a close to an open state varies extremely slowly (infrequent openings, [45], [49]). The Imredy and Yue model, which the work of Jafri & al was inspired, states that the probability that L-type channel is controlled by the combination of two independent inactivation processes which includes this Ca^{2+} -mediated inactivation and a voltage-dependent inactivation. The channels' sensitivity for the membrane potential can be seen as a reduction in the overall availability of the channel to open at all [49]. Imredy and Yue predicts also that inactivation process happens with some delay after channel activation (REF) and the recovery to mode normal is not immediate when the $[Ca^{2+}]$ returns to its resting value. The JRW model takes into account these inactivation behavior by incorporating the model of Imredy and Yue (1994) citeJafri. Nonetheless, Jafri & al improves the original Imredy and Yue by incorporating the following points:

- Additional states
- Improved Ca^{2+} inactivation
- Improved voltage-dependent inactivation and activation
- Open-channel ion permeation

The complete L-channel states model is represented in Figure 2.23. Each of the channels is assumed to be composed of four sub-units which can lead to close the channel individually. To simulate those subunits five mode normal closed states C_i , $i = \{1, 2, 3, 4\}$ and their respective mode Ca are created. The voltage-dependence on the inactivation or the activation is introduced through the parameters α and β , which are increasing resp. decreasing functions of membrane voltage. In the other hand, the inactivation gating variable is modeled as a Hodgkin-Huxley-type gate (see equation (2.27)) which depend on the membrane potential (see Appendix).

The transitions between C_4 to O (or C_{Ca_4} to O_{Ca}) are in contrast voltage-independent. The calcium dependence part of the diagram is introduces by the γ parameter which depends on the Ca_{ss}^{2+} concentration. Moreover, in order to increase the transition rate to mode Ca at high voltages, an incremental augmentation of the exponent's multiplier of γ and the divisor of ω is introduced [45]. The rate constants are constructed in order to satisfy some constraints like thermodynamic microreversibility. Microreversibility is a general concept that declares that each process at the microscopic point of view is reversible leading to the fact that in thermodynamic

equilibrium the global rate in one direction is equal to the global rate in the reverse direction. This results in the fact that for each transition's cycle, the product of all the rates in Figure 2.23 might be equal whatever the direction process is taken in a sense or in the opposite one.

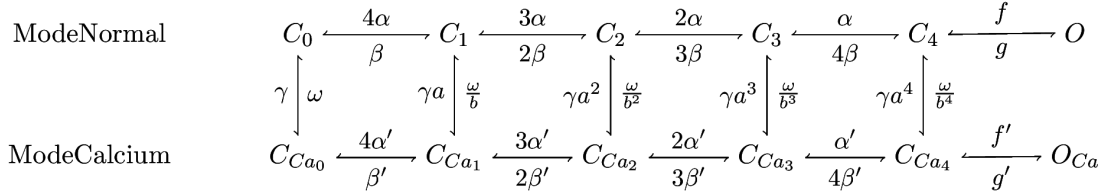


Figure 2.23: Transitions' diagram of the L-type Ca^{2+} channel's states. The subscript Ca indicates the mode Ca transitions while numerical subscripts represent the number of permissive subunits. The C respectively O states corresponds to the close resp. open states. The detailed mathematical model is presented in Appendix.

Finally, the JRW model take also into account the permeability properties of the L-type channel by introducing a new permeation model where it is assumed that:

- Ca^{2+} current follows the constant field theory (Section 2.3.1)
- Ca^{2+} current is the unique inward current that pass across the channel
- K^+ permeability decreases with increasing Ca^{2+} current.

Ryanodine Receptors One another important aspect of the JRW model is to model the ryanodine receptors (RyR) channels. This model is based on the model of Keizer and Levine where the receptor presents two open states (P_{O_1} , P_{O_2}) and two closed states (P_{C_1} , P_{C_2}) where the transitions are submitted to the adaptative behavior of RyR channels. These states follows the diagram model presented in 2.24. At rest conditions, the ionic channel states begins with the first closed state, called P_{C_1} . When $[Ca^{2+}]$ augments, RyR switches first at all and briefly to state P_{O_1} , allowing the calcium to cross the SR membrane. During this short cytosolic Ca^{2+} -elevation, the channel adapts and moves consequently from the P_{O_1} to the P_{C_2} .

During this process, the RyR channel states change from P_{O_1} to P_{C_2} . The channels reopen by its transition to P_{O_2} upon additional Ca^{2+} concentration augmentation [50]. This states presents an adaptive behavior [50].

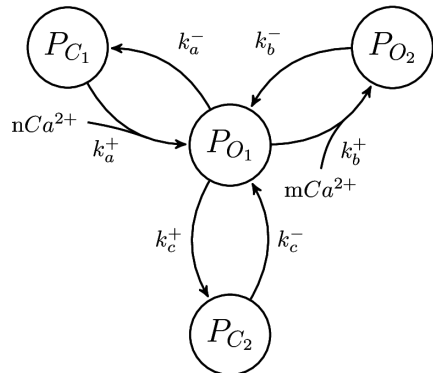


Figure 2.24: Transitions' diagram of the RyR's states. The subscript C (resp. O) indicates closed (resp. opened) states while numerical subscripts represent the subtype of closed or opened state. The detailed mathematical model is presented in Appendix.

2.4.3 Contraction Simulation

One major aspect in the simulation of the heart function is the coupling of the bioelectrical phenomena with the contraction of myocytes (*excitation-contraction coupling*). The calcium dynamics are of paramount importance on models since they allow possible simulation of this contraction coupling. Contrary for those ionic models, the number of silico experiments developed in order to obtain a general model (which can reproduce a maximum of the experimental measurements on the muscle behavior [17]), lags behind the number of these last ones. Despite that a large class of experiments were performed, the biochemical details of the myosin-actin contraction system is still not well understood [51], which increases the difficulty to implement a universal and “correct” model. In general cases, the developed models try to catch only few mechanical features of the sarcomere, and for instance up to date, no complete excitation-contraction model is available [51].

Nonetheless, one of the most influential theory on this area is the crossbridge theory introduced in the Huxley model in 1957 [17]. This theory postulates that each crossbridges (the head of the globular myosin, see 2.13) acts as independent simple springs and the total force is generated by the proportion of bounded crossbridges in the overlap A-band of the sarcomere. In a mathematical perspective, the Huxley model schematizes the sarcomere unit as presented in Fig. 2.25 [17].

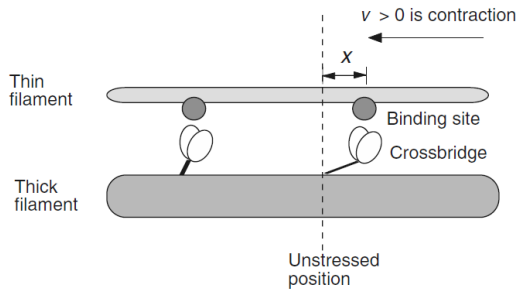


Figure 2.25: Diagram of the Huxley crossbridge model [17].

This description supposes that myosin heads can bind to actin filaments at a position x corresponding to the distance between the base of the myosin and the binding site on the thin filament. Furthermore, Huxley supposed that each binding site is sufficiently far away leading to the fact that each crossbridge is bounded to an unique site. In this model, the dynamics of the crossbridges are simply based on two states: bounded and detached [17]. The rates between these two states was considered as functions of x , which might be reasonably choosen in order to capture the dynamics of the contraction [17]. This model enables to predict that an increase on the contraction velocity leads to a force’s diminution due to the decrease of attached crossbridges and the decrease of the averaged elongation of the crossbridges to the binding sites. However, the model fails to capture some more recent experimental observations, as force transient due to a rapid sarcomere length.

A large number of works improved this model by either incorporating dependence on the crossbridges binding, or increasing the number of possible states, or finally changing the transition rates functions by taking into account thermodynamic considerations of the ATPase part into the contraction cycle [51].

One of those models is the Negroni-Lascano (NL) model (1995) which take into account the control mechanism of the troponin into the binding states of the crossbridges to the thin actin filament [18]. The NL model postulates that a half-length sarcomere is structured as a compound of an inextensible thick and thin filaments in parallel, able to slide over each other conjugated

with an elastic internal load (see Figure 2.26). This load represents (in the NL perspective) the intracellular components and the collagen cobweb around the cells [18].

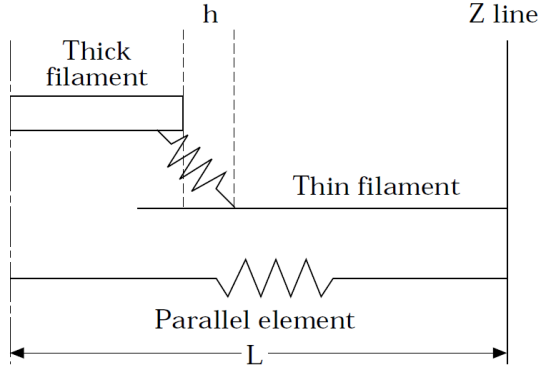


Figure 2.26: Half muscle structure diagram of the Negroni Lascano crossbridge model [18]. L stands for the half-length sarcomere while h represents the myosin head elongation from the no force position $h = 0$.

As others crossbridges models, NL assumes that the binding of the myosin heads happens independently of each other in the A-band. Besides, they assume a list of four principal points in the dynamics of the myosin heads [18]:

- Force is induced only by the number of attached crossbridges, which depends on the sarcomere length.
- The elongation of the elastic structure of the myosin head triggers the formation of a force.
- For each steady sarcomere length, the elongation exists on a unique configuration. Any change in sarcomere length induces a simultaneous change of the crossbridge elongation to the steady-state value, by a mechanism of detachment-attachment in a distinct position of the thin filament.
- Finally, the velocity of the detachment process during any length modifications is a function of the re-adjusted crossbridges elongation rate.

Based on these assumptions, each crossbridge is represented as a linear elastic spring (see Figure 2.26) with one extremity attached to the thick filament and the other that can slide along the thin filament. One particular point of this model is to consider for simplicity an equivalent crossbridge that summarized all the attached myosin heads. The elongation h in this perspective represents the average distance between the equilibrium position (no net forces) and the position of attachment. Mathematically, this is described by the following formulation:

$$h = L - X \quad (2.30)$$

Here X stands for the half-length of the thick filaments plus the thin filament length which is not located in the overlapping zone [18]. At steady-state conditions, h equals to a constant length given by h_c . Any step length changes induces a corresponding change on h , given by $h = h_c - \Delta L$. From the crossbridges theory, any changes in the sarcomere structure are accompanied by a force which does not present any fluctuations. This is due to the fact, that in cardiac muscle, all the crossbridges are not in the same configuration state of the mechanical cycle (Section 2.2.4) leading to the fact that the detachment and re-attachment process is done asynchronously [18]. In the NL model, the asynchronous behavior is simulated by shifting the attached point of the equivalent

crossbridge which it is accompanied by a change in X length mathematically described by the ODE (2.31) which expresses the motion velocity of the myosin head extremity.

$$\begin{aligned}\frac{dX}{dt} &= B(h - hc) \\ &= B(L - X - hc)\end{aligned}\quad (2.31)$$

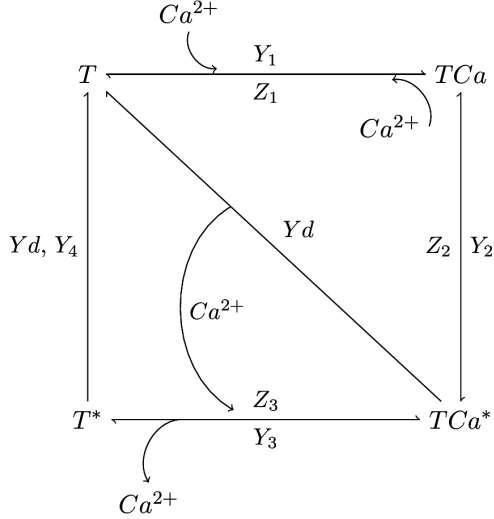


Figure 2.27: Diagram of the Ca^{2+} -kinetics used in the Negroni Lascano model.

The last part of the model is the contribution of the Ca^{2+} dynamics into the myofilament activation. To this end, Negroni & Lascano use a four-states system of binding sites on the actin filament associated with that of the troponin C molecule [18]. The system is schematized in Fig. 2.27. The states that constitute the system can be classified in two principal class: T -states which stands for sites with free troponin C and TCa for sites with bounded Ca^{2+} -troponin C complex. The $*$ superscript indicates sites where crossbridges are attached. During rapid release of Ca^{2+} in the intracellular space, the ion binds to T to form, in a first step, a complex TCa . This binding enables the crossbridges in the A-band to bind to the thin filament (TCa^*), each of them is associated to a unique TCa complex. In a third step, the Ca^{2+} is released of the complex Ca^{2+} -troponin C. However, the crossbridges stay fixed to the thin filament and gives rise to the T^* state. Consequently, the force is generated in the NL model during contraction by the TCa^* and T^* . The evolution of Ca^{2+} is described by a small system of coupled ODEs which depends on the transition rates between the states (equation (2.32))

$$\begin{aligned}Q_b &= Y_1[Ca^{2+}][T] - Z_1[TCa] \\ &= Y_1[Ca^{2+}]([T]_t - [TCa] - [TCa^*] - [T^*]) - Z_1[TCa] \\ Q_a &= Y_2[TCa]_{eff} - Z_2[TCa^*] \\ Q_r &= Y_3[TCa^*] - Z_3[T^*][Ca^{2+}] \\ Q_d &= Y_4[T^*] \\ Q_{d1} &= Y_d \left(\frac{dX}{dt} \right) [T^*] \\ Q_{d2} &= Y_d \left(\frac{dX}{dt} \right) [TCa^*],\end{aligned}\quad (2.32)$$

where $[T]_t$ is the total troponin C concentration and $[TCa]_{eff}$ represents the concentration of complex Ca^{2+} -troponin C located in the overlap zone. It is defined as $[TCa]e^{-R(L-L_a)^2}$, where

the gaussian term scales the true concentration of states involved in the contraction system. The use of a gaussian function allows to consider a symmetric length effect around the L_a value which represents the length of ideal overlapping to obtain the maximum of Ca^{2+} -troponin C complex concentration. The states Q_{d1} and Q_{d2} enable to take into account the detachment of certain proportion of the crossbridges represented as a change in the X value. Then the ODEs associated are:

$$\begin{aligned}\frac{d[TCa]}{dt} &= Q_b - Q_a \\ \frac{d[TCa^*]}{dt} &= Q_a - Q_r - Q_{d2} \\ \frac{d[T^*]}{dt} &= Q_r - Q_d - Q_{d1}\end{aligned}\tag{2.33}$$

In order to complete the mathematical model that describes the excitation-contraction coupling, we might include these transition rates in the dynamics of the Ca^{2+} in the ionic model. For a general ionic model, the Ca^{2+} ODE is defined as:

$$\frac{d[Ca_i^{2+}]}{dt} = g(V_m, w_{Ca}) - F(Q_b, Q_r, Q_{d2}),\tag{2.34}$$

where $g(V_m, w_{Ca})$ is a non-linear function that depends on the membrane potential V_m and w_{Ca} (the ionic states variables associated to the dynamics of the intracellular calcium, including ionic concentration and gating variables). Here $F(Q_b, Q_r, Q_{d2})$ is some linear or non-linear function of the associated fluxes that satisfies a consistent formulation according to the form of g .

According to these definitions and the Ca^{2+} -kinetic model, it was now possible to compute the total muscle force of a single cell according to the formulas given in (2.35).

$$\begin{aligned}F &= F_p + F_b \\ F_b &= A([TCa^*] + [T^*]) \cdot (L - X),\end{aligned}\tag{2.35}$$

where A , L_0 and K are model parameters. In (2.35), F_p represents the force developed by the elastic load element, while F_b is the force generated by all the attached crossbridges represented by the concentration of states $[TCa^*]$ and $[T^*]$. In the case of muscle contraction the force might include the compliant ends of the muscle [18]. For that, the model includes an additional elastic element in series with the muscle which is formulated as the length L_{sm} . This length is linked to the force generated through the following expression:

$$F = F_s = \alpha(e^{L_{sm}} - 1)\tag{2.36}$$

By definition, the total length of the muscle is now defined as $F_{tm} = L_m + L_{sm}$, with $L_m = N_0 \cdot L$. The equation (2.36), combined with the previous equations, gives us the relation between the force and length variable for the simulation of several contraction scenarios.

Chapter 3

Numerical Analysis and Implementation

This brief chapter will introduce some numerical details and main methods used in order to solve all the systems introduced in Section 2.4.1. We will encounter a brief description of the used numerical integrator and their respective parameters. Initial conditions and intrinsic parameters of the respective ionic or electro-mechanical model will be provided also in this chapter. In the two main parts of this chapter, all the protocols (stimulation, mechanical) implemented will be summarized. For sake of clarity, the description will be separated between the electrical and electro-mechanical simulations.

3.1 Electrophysiological simulation

3.1.1 Ionic models

In general, all codes for the ionic model simulations were written in C++, in the framework of the LifeV finite element library [52].

The TNNP model was solved numerically by a combination of Rush and Larsen [53] scheme and forward Euler method with a constant time step of $\Delta t = 0.01$ ms. The forward Euler method is a basic and explicit integrator, which has the property to be easily implemented and also not to be computationally expensive. However, due to its explicit nature, it is submitted to time step restriction and can lead to instabilities particularly for stiff problems that can be usually encountered in the ODEs systems describing ionic models. Some preliminary tests are made in order to find the largest time step where the numerical solution remains stable. The time step used is found to be the largest possible value that can be safely used for the simulations.

The other important numerical integrator used to solve the ionic model is the Rush and Larsen integration scheme. It was applied to solve the ODEs for gating variables in TNNP model. As it was explained in the section 2.4.1, since Hodgkin & Huxley model was implemented, many of recent models keep the same structure in order to describe the ionic currents, especially for its mathematical description. In general, the conductances G_i are expressed as a proportional function of some gating variables \mathbf{y} [53]

$$G_i = \bar{G}_i \cdot f_i(y_1, y_2, \dots, y_n) = \bar{G}_i \cdot f_i(\mathbf{y}) \quad (3.1)$$

The gating variables depend non-linearly on time and in most of the cases, only implicitly through the transmembrane voltage variable V_m . [53]

$$\frac{dy_j}{dt} = a_j(V_m(t))y_j - b_j(V_m(t)), \quad j = 0, 1, \dots, n \quad (3.2)$$

Based on (3.2), the integration of the differential equation can not be computed straightforwardly due to the presence of the non-linear terms ($a_j(V_m(t))$ and $b_j(V_m(t))$). According to the ODE (3.2), different approximation schemes can be used in order to obtain numerical integrators which approximate the true solution with the smallest error and a minimum computational cost.

The Rush and Larsen scheme, which is of the class of non-standard finite-differences (NSFD) ODE solvers, is based on the fact that we consider that $a_j(V_m(t))$ and $b_j(V_m(t))$ to be constant throughout one step duration Δt [53]. In this case, we can compute easily and analytically the differential equation (3.2) and find the associated Rush and Larsen scheme (eqn. (3.3))

$$y_j^{n+1} = e^{a_j^n \Delta t} \left(y_j^n - \frac{b_j^n}{a_j^n} \right) + \frac{b_j^n}{a_j^n}, \quad j = 0, 1, \dots, n, \quad (3.3)$$

where the index n (resp. $n + 1$) stands for time t^n (resp. t^{n+1}).

The Rush and Larsen (RL) integrator is particularly popular for solving ODEs based on ionic models for cardiac electrophysiology [53]. Indeed, this scheme, which is numerically as simple to implement as the forward Euler method, has proved to be significantly better in some aspects than the standard Euler method. First at all, the method possesses a stability bound which is less restrictive than the forward Euler method even if it is always an explicit scheme [53]. Hence, it allows using larger time step. This property is important by the fact that the ODEs of the ionic model is coupled with the PDEs of the continuous approximation of cardiac tissue, and large time step allows to compute the overall system with a smaller computational cost. Then, RL scheme has the property that the numerical solution belongs to the interval $[0, 1]$ when it was applied on differential equations linked to gating variables [53]. Nonetheless, it still has an overall accuracy of first order as the explicit Euler method.

Throughout all the simulations, the ten Tusscher & al. model was implemented by using the parameters of Table 3.1. A physiological description of the parameters was added in the table for sake of clarity. All modified parameters from the original paper [24] are indicated by the presence of the original ones in parenthesis. Moreover, the initial conditions used in the ODEs system was taken from the cellML Project models repository in the category electrophysiology, section, ten Tusscher, Noble, Noble, Panfilov, 2004 [54].

Table 3.1: Table of the parameters used for Ten Tusscher ionic model. The values in parenthesis are the original values of the K.H.W.J. ten Tusscher & A.V. Panfilov paper (2004).

<i>Parameter</i>	<i>Definition</i>	<i>Value</i>
R	Ideal gas constant	$8314.472 \text{ mJ} \cdot \text{K}^{-1} \cdot \text{mol}^{-1}$
F	Faraday constant	$96485.3415 \text{ C} \cdot \text{mol}^{-1}$
T	Absolute temperature	310 K
C_m	Cell capacitance	$5 \cdot 10^3 \text{ fF}$ $(2 \mu\text{F} \cdot \text{cm}^{-2})$
V_c	Cytoplasmic volume	$16404 \mu\text{m}^3$
V_{SR}	Sarcoplasmic reticulum volume	$1094 \mu\text{m}^3$
$[K_o^+]$	Extracellular K^+ concentration	5.4 mM
$[Na_o^+]$	Extracellular Na^+ concentration	140 mM
$[Ca_o^{2+}]$	Extracellular Ca^{2+} concentration	2 mM
G_{Na}	Maximal I_{Na} conductance	$14.838 \text{ nS} \cdot \text{pF}^{-1}$
$G_{K,1}$	Maximal $I_{K,1}$ conductance	$5.405 \text{ nS} \cdot \text{pF}^{-1}$
$G_{to \text{ epi, M cell}}$	Maximal epicardial and M cell I_{to} conductance	$0.294 \text{ nS} \cdot \text{pF}^{-1}$
$G_{to \text{ endo}}$	Maximal endocardial I_{to} conductance	$0.073 \text{ nS} \cdot \text{pF}^{-1}$
G_{Kr}	Maximal I_{Kr} conductance	$0.096 \text{ nS} \cdot \text{pF}^{-1}$
$G_{Ks \text{ endo, epi}}$	Maximal endocardial and epicardial I_{Ks} conductance	$0.322 \text{ nS} \cdot \text{pF}^{-1}$ $(0.245 \text{ nS} \cdot \text{pF}^{-1})$
$G_{Ks \text{ M cell}}$	Maximal M cell I_{Ks} conductance	$0.098 \text{ nS} \cdot \text{pF}^{-1}$

$p_{Na,K}$	Relative I_{Ks} permeability to Na^+	(0.062 $nS \cdot pF^{-1}$) 0.01833 (0.03)
$G_{Ca,L}$	Maximal $I_{Ca,L}$ conductance	$9.25 \cdot 10^{-5} L \cdot F^{-1} \cdot ms^{-1}$ ($1.75 \cdot 10^{-4} cm^3 \cdot \mu F^{-1} \cdot s^{-1}$)
k_{NaCa}	Maximal I_{NaCa}	1000.0 $pA \cdot pF^{-1}$
γ	Voltage dependance parameter of I_{NaCa}	0.35
$K_{m,Ca}$	Ca_i^{2+} half-saturation constant for I_{NaCa}	1.38 mM
$K_{m,Nai}$	Na_i^+ half-saturation constant for I_{NaCa}	87.5 mM
k_{sat}	Saturation factor for I_{NaCa}	0.1
α	Factor enhancing outward nature of I_{NaCa}	2.5
P_{NaK}	Maximal I_{NaK}	2.724 $pA \cdot pF^{-1}$ (1.362 $pA \cdot pF^{-1}$)
$K_{m,Ko}$	K_o^+ half-saturation constant for I_{NaK}	1.5 mM (1.0 mM)
$K_{m,Nai}$	Na_i^+ half-saturation constant for I_{NaK}	10.0 mM (40.0 mM)
G_{Kp}	Maximal I_{Kp} conductance	0.00828 $nS \cdot pF^{-1}$ (0.0146 $nS \cdot pF^{-1}$)
$G_{p(Ca)}$	Maximal $I_{p(Ca)}$ conductance	0.1238 $nS \cdot pF^{-1}$ (0.0025 $nS \cdot pF^{-1}$)
$K_{p(Ca)}$	Ca_i^{2+} half-saturation constant for $I_{p(Ca)}$	0.0005 mM
$G_{Na,b}$	Maximal $I_{Na.b}$ conductance	0.00141 $nS \cdot pF^{-1}$ (0.00029 $nS \cdot pF^{-1}$)
$G_{Ca,b}$	Maximal $I_{Ca,b}$ conductance	0.003016 $nS \cdot pF^{-1}$ (0.000592 $nS \cdot pF^{-1}$)
$V_{max,up}$	Maximal J_{up}	0.006375 $mM \cdot ms^{-1}$ (0.000425 $mM \cdot ms^{-1}$)
$K_{m,up}$	Half-saturation constant for J_{up}	0.00025 mM
a_{rel}	Maximal Ca_{SR}^{2+} -dependent J_{rel}	0.016464 $mM \cdot ms^{-1}$
b_{rel}	Ca_{SR}^{2+} half-saturation constant for J_{rel}	0.25 mM
c_{rel}	Maximal Ca_{SR}^{2+} -independent J_{rel}	0.008232 $mM \cdot ms^{-1}$
V_{leak}	Maximal J_{leak}	0.00036 ms^{-1} (0.00008 ms^{-1})
$[Buf_c]_T$	Total cytoplasmic buffer concentration	0.2 mM (0.15 mM)
K_{Buf_c}	Ca_i^{2+} half-saturation constant for cytoplasmic buffer	0.001 mM
$[Buf_{sr}]_T$	Total sarcoplasmic buffer concentration	10.0 mM
$K_{Buf_{sr}}$	Ca_{SR}^{2+} half-saturation constant for sarcoplasmic buffer	0.3 mM

For the case of the JRW model, the simulations was performed also with a forward Euler method with constant time step of 10^{-4} ms. As for the previous model, the time step was tested in order to verify the stability of the numerical method during simulations with large time horizons. For this purpose, and to compare with the FE numerical results, a classical Runge-Kutta method (RK4) was implemented. RK4 is an explicit fourth order integrator which is formulated for a general ODE $\dot{y} = f(t, y)$, $y(t_0) = y_0$ as:

$$y_{n+1} = y_n + \frac{1}{6} (K_1 + 2K_2 + 2K_3 + K_4) \text{ for } n \in \mathbb{N},$$

where

$$\begin{aligned} K_1 &= f(t_n, y_n) \\ K_2 &= f\left(t_n + \frac{\Delta t}{2}, y_n + \frac{\Delta t K_1}{2}\right) \\ K_3 &= f\left(t_n + \frac{\Delta t}{2}, y_n + \frac{\Delta t K_2}{2}\right) \\ K_4 &= f(t_n + \Delta t, y_n + \Delta t K_3) \end{aligned} \quad (3.4)$$

In this case the results for different time steps will be presented in Section 4.1.2. The parameters used for the conduction simulation in the JRW model are summarized in Table 3.2. As in Table 3.1, the original parameters of Jafri & al. work [45] are presented in parenthesis if modified. The initial conditions are taken as in the Jafri & al. paper. However, some adjustments in the units are made in order to be consistent between all the variables of the model. Therefore, the initial concentration of *LTRPN**Ca* or *HTRPN**Ca* complexes are taken in mM. Furthermore, the initial intracellular calcium concentration, $[Ca_i^{2+}]$, was equal in our simulation to $9.94893 \cdot 10^{-5}$ mM.

Table 3.2: Table of the parameters used for Jafri Rice Winslow ionic model. The values in parenthesis are the original values of the M.S Jafri, J.J. Rice & R.L. Winslow model (1998).

Parameter	Definition	Value
R	Ideal gas constant	$8314.5 \text{ mJ} \cdot \text{K}^{-1} \cdot \text{mol}^{-1}$
F	Faraday constant	$96485 \text{ C} \cdot \text{mol}^{-1}$
T	Absolute temperature	310 K
A_{cap}	Capacitive membrane area	$1.534 \cdot 10^{-2} \text{ mm}^2$
C_m	Cell surface capacitance	$0.01 \mu\text{F} \cdot \text{mm}^{-2}$
V_{myo}	Myoplasmic volume	$25.84 \cdot 10^{-6} \mu\text{L}$
V_{JSR}	Junctional sarcoplasmic volume	$0.12 \cdot 10^{-6} \mu\text{L}$
V_{NSR}	Network sarcoplasmic volume	$2.098 \cdot 10^{-6} \mu\text{L}$
V_{ss}	Subspace volume	$1.485 \cdot 10^{-9} \mu\text{L}$
$[Na^+]$	Extracellular Na^+ concentration	140 mM
$[Ca_o^{2+}]$	Extracellular Ca^{2+} concentration	1.8 mM
$[LTRPN]_{Tot}$	Total myoplasmic troponin low-affinity site concentration	0.07 mM
$[HTRPN]_{Tot}$	Total myoplasmic troponin high-affinity site concentration	0.14 mM
k_{HTRPN}^+	Ca^{2+} on rate constant for troponin high-affinity sites	$20 \text{ mM}^{-1} \cdot \text{ms}^{-1}$
k_{HTRPN}^-	Ca^{2+} off rate constant for troponin high-affinity sites	$6.6 \cdot 10^{-5} \text{ ms}^{-1}$
k_{LTRPN}^+	Ca^{2+} on rate constant for troponin low-affinity sites	$40 \text{ mM}^{-1} \cdot \text{ms}^{-1}$
k_{LTRPN}^-	Ca^{2+} off rate constant for troponin low-affinity sites	0.04 ms^{-1}
$[CMDN]_{Tot}$	Total myoplasmic calmodulin concentration	0.05 mM
$[CSQN]_{Tot}$	Total myoplasmic calsequestrin concentration	15 mM
K_m^{CMDN}	Ca^{2+} half saturation constant for calmodulin	$2.38 \cdot 10^{-3} \text{ mM}$
K_m^{CSQN}	Ca^{2+} half saturation constant for calsequestrin	0.8 mM
G_{Na}	Maximal I_{Na} conductance	$0.128 \text{ mS} \cdot \text{mm}^{-2}$ $(12.8 \text{ mS} \cdot \mu\text{F}^{-1})$
\bar{G}_{K_p}	Maximal I_{K_p} conductance	$8.28 \cdot 10^{-5} \text{ mS} \cdot \text{mm}^{-2}$ $(0.00828 \text{ mS} \cdot \mu\text{F}^{-1})$
$P_{Na,K}$	Na^+ permeability of K^+ channel	0.01833
k_{NaCa}	Scaling factor of Na^+ - Ca^{2+} exchange	$100 \mu\text{A} \cdot \text{mm}^{-2}$ $(5000 \mu\text{A} \cdot \mu\text{F}^{-1})$

$K_{m,Na}$	Na^+ half saturation constant for I_{NaCa}	87.5 mM
$K_{m,Ca}$	Ca^{2+} half saturation constant for I_{NaCa}	1.38 mM
k_{sat}	Saturation factor for I_{NaCa}	0.1
η	Voltage dependance parameter of I_{NaCa}	0.35
\bar{I}_{NaK}	Maximum I_{NaK} current	$0.013 \mu A \cdot mm^{-2}$ ($1.3 \mu A \cdot \mu F^{-1}$)
K_{m,Na_i}	Na^+ half saturation constant for I_{NaK}	10 mM
K_{m,K_o}	K^+ half saturation constant for I_{NaK}	1.5 mM
$P_{ns(Ca)}$	Nonspecific current channel permeability	$0.0 mm \cdot ms^{-1}$
$K_{m,ns(Ca)}$	Ca^{2+} half saturation constant for $I_{ns(Ca)}$	$1.2 \cdot 10^{-3} mM$
$\bar{I}_{p(Ca)}$	Maximum $I_{p(Ca)}$ current	$1.15 \cdot 10^{-2} \mu A \cdot mm^{-2}$ ($1.15 \mu A \cdot \mu F^{-1}$)
$K_{m,p(Ca)}$	Ca^{2+} half saturation constant for $I_{p(Ca)}$	$0.5 \cdot 10^{-3} mM$
$\bar{G}_{Ca,b}$	Maximal $I_{Ca,b}$ conductance	$6.032 \cdot 10^{-5} mS \cdot mm^{-2}$ ($0.006032 mS \cdot \mu F^{-1}$)
$\bar{G}_{Na,b}$	Maximal $I_{Na,b}$ conductance	$1.41 \cdot 10^{-5} mS \cdot mm^{-2}$ ($0.00141 mS \cdot \mu F^{-1}$)
ν_1	Maximum RyR channel Ca^{2+} permeability	$1.8 ms^{-1}$
ν_2	Ca^{2+} leak rate constant from the NSR	$5.8 \cdot 10^{-5} ms^{-1}$
ν_3	SR Ca^{2+} -ATPase maximum pump rate	$1.8 \cdot 10^{-3} mM \cdot ms^{-1}$
$K_{m,up}$	Half saturation constant for SR Ca^{2+} -ATPase pump	$0.5 \cdot 10^{-3} mM$
τ_{tr}	Time constant for transfer from NSR to JSR	34.48 ms
τ_{xfer}	Time constant for transfer from subspace to myoplasm	3.125 ms
k_a^+	RyR $P_{C1}-P_{O1}$ rate constant	$1.215 \cdot 10^{10} mM^{-4} \cdot ms^{-1}$
k_a^-	RyR $P_{O1}-P_{C1}$ rate constant	$0.1425 ms^{-1}$
k_b^+	RyR $P_{O1}-P_{O2}$ rate constant	$4.05 \cdot 10^6 mM^{-3} \cdot ms^{-1}$
k_b^-	RyR $P_{O2}-P_{O1}$ rate constant	$1.93 ms^{-1}$
k_c^+	RyR $P_{O1}-P_{C2}$ rate constant	$0.018 ms^{-1}$
k_c^-	RyR $P_{C2}-P_{O1}$ rate constant	$0.0008 ms^{-1}$
n	RyR Ca^{2+} cooperativity parameter $P_{C1}-P_{O1}$	4
m	RyR Ca^{2+} cooperativity parameter $P_{O1}-P_{O2}$	3
f	Transition rate into open state	$0.3 ms^{-1}$
g	Transition rate out of open state	$2 ms^{-1}$
f'	Transition rate into open state for mode Ca^{2+}	$0 ms^{-1}$
g'	Transition rate out of open state for mode Ca^{2+}	$0 ms^{-1}$
a	Mode transition parameter	2
b	Mode transition parameter	2
ω	Mode transition parameter	$0.01 ms^{-1}$
\bar{P}_{Ca}	L-type Ca^{2+} channel permeability to Ca^{2+}	$54.0 \cdot 10^{-6} mm \cdot ms^{-1}$ ($33.75 \cdot 10^{-6} mm \cdot ms^{-1}$)
\bar{P}_K	L-type Ca^{2+} channel permeability to K^+	$1.0 \cdot 10^{-9} mm \cdot ms^{-1}$
$I_{Ca,L,half}$	$I_{Ca,L}$ level that reduces \bar{P}_K by half	$-4.58 \cdot 10^{-3} \mu A \cdot mm^{-2}$ ($-0.458 \mu A \cdot \mu F^{-1}$)

3.1.2 Pacing protocols

In order to compute the AP duration and amplitude, some of the standard protocols have been implemented through a stimulation C++ class. The three major kinds of pacing protocols, that we have coded, are listed below:

- Fixed Cycle Length (FCL)
- Standard S1-S2 restitution protocol (S1S2Pro)
- Dynamic restitution protocol (DynPro)

Briefly, the S1-S2 restitution protocol consists of a protocol scheme where a premature applied current is triggered at regular beats number. Beginning from an initial S1-S2 interval, the

stimulation interval between normal and the extrastimulus is decreased progressively until a chosen value. In the dynamic protocol, the cells are paced at an initial S1-S1 interval which is diminished after a number of repeated stimuli [55], [56].

In all the implemented protocols, a large part of the coding takes into account a possible tuning of the stimulation parameters such as the time or the amplitude of the stimulation current for example. This restriction enables a general use in the cardiac simulation context and allows modification of the pacing protocol without changing all the time the implemented code. All definitions of the parameters can be found in Table 3.3. Some of them present different definitions according to the pacing protocol context and hence all their significations will be listed also on Table 3.3. In all cases, the methods need some variables as input: the time t , the time step Δt , a stimulation counter $N_{Stimulus}$ and the applied current for stimulation I_{app} , that will be used in the solver of the ionic model.

<i>Attribute</i>	<i>Definition</i>
M_{timeSt}	Stimulation time
$M_{StimDuration}$	Applied current stimulation duration
M_{Istim}	Amplitude of the applied current
$M_{nbStimMax}$	FCL: Maximum number of stimulation
	S1S2Pro: Number of stimulation for stabilization
M_{stInt}	S1-S1 time interval
$M_{stIntS1S2}$	S1-S2 time interval
$M_{stIntS1S2Min}$	Minimum S1-S2 time interval
$M_{repeatSt}$	S1S2Pro: Number of S1-S1 stimulations between S2 stimulation
	DynPro: Number of S1-S1 stimulations before S1-S1 interval
$M_{tShortS1S1}$	time shortening
$M_{stIntMin}$	Time of first S1-S1 interval diminution
	Minimum S1-S1 time interval

Table 3.3: Definition table of the pacing protocol class' attributes encountered in the Appendix.

All the different methods used for the stimulation pacing protocol can be found in the Appendix.

3.2 Electro-mechanical coupling

3.2.1 Parameters and numerical solver

The study of the electro-mechanical coupling will be separated in two parts. The first one will be a validation of the parameters listed on Table 3.4. We simulate the contraction mechanism subject to a constant calcium concentration of $2 \mu M$ (tetanized muscle,). As this part does not require the computation of the ionic model evolution, it was computed with a simple code in MATLAB version 7.11.0.584 (R2010b, 32-bit). The associated script is in the Appendix. In this script, and also for the coupling part, the ODEs system of the crossbridges dynamics (2.33) was solved by a predictor-corrector scheme: (the Heun's method) the prime superscript for the Q terms indicated that they were computed using the results of the predictor step:

For $k \in \mathbb{N}$:

$$\begin{aligned}
[TCa]^{k+1,\prime} &= [TCa]^k + \Delta t \left(Q_b^k - Q_a^k \right) \\
[TCa^*]^{k+1,\prime} &= [TCa^*]^{k,\prime} + \Delta t \left(Q_a^k - Q_r^k - Q_{d2}^k \right) \\
[T^*]^{k+1,\prime} &= [T^*]^k + \Delta t \left(Q_r^k - Q_d^k - Q_{d1}^k \right) \\
[TCa]^{k+1} &= [TCa]^k + \frac{\Delta t}{2} \left(Q_b^{k,\prime} - Q_a^{k,\prime} + Q_b^k - Q_a^k \right) \\
[TCa^*]^{k+1} &= [TCa^*]^k + \frac{\Delta t}{2} \left(Q_a^{k,\prime} - Q_r^{k,\prime} - Q_{d2}^{k,\prime} + Q_a^k - Q_r^k - Q_{d2}^k \right) \\
[T^*]^{k+1} &= [T^*]^k + \frac{\Delta t}{2} \left(Q_r^{k,\prime} - Q_d^{k,\prime} - Q_{d1}^{k,\prime} + Q_r^k - Q_d^k - Q_{d1}^k \right)
\end{aligned} \tag{3.5}$$

This is an explicit method which has the advantage to be second order in Δt preventing large errors propagation between the crossbridges and the ionic model. The time step used to solve (3.5) was 10^{-1} ms. In the electro-mechanical models, the time step is respectively 10^{-2} ms for TNNP, and 10^{-4} for the JRW model. A more restrictive time step was necessary in order to compute correctly the ionic part. The computation of the X variable (2.31) was performed with an implicit Euler method.

Parameters	Value	Parameters	Value
Y_1	$39 \cdot 10^{-3} \mu M^{-1} \cdot ms^{-1}$ (TNNP)	Y_2	$1.3 \cdot 10^{-3} ms^{-1}$
	$40 \cdot 10^{-3} \mu M^{-1} \cdot ms^{-1}$ (JRW)	Y_4	$40 \cdot 10^{-3} ms^{-1}$
Y_3	$30 \cdot 10^{-3} ms^{-1}$	Z_1	$30 \cdot 10^{-3} ms^{-1}$ (TNNP)
Y_d	$9000 ms \cdot \mu m^2$	Z_1	$40 \cdot 10^{-3} ms^{-1}$ (JRW)
Z_2	$1.3 \cdot 10^{-3} ms^{-1}$	Z_3	$1.56 \mu M^{-1} \cdot ms^{-1}$
$[T_t]$	$70 \mu M$	B	$1.2 ms^{-1}$
h_c	$0.005 \mu M$	L_a	$1.17 \mu m$
R	$20 \mu m^{-2}$	A	$1800 mN \cdot mm^{-2} \cdot \mu M^{-1} \cdot \mu m^{-1}$
K	$1.4 \cdot 10^5 mN \cdot mm^{-2} \cdot \mu m^{-5}$	L_0	$0.97 \mu m$
α	$0.5 mN \cdot mm^{-2}$	β	$100 \mu m^{-1}$

Table 3.4: Table of the electro-mechanical coupling parameters based on the crossbridges model of Negroni & Lascano [18]. Y_1 and Z_1 have been modified for the JRW model in order to be consistent with the original equations.

The coupling term between the ionic and the crossbridges model was implemented differently between the two ionic models. In TNNP, the coupling was computed according to relation (3.6).

$$\begin{aligned}
F(Q_b, Q_r, Q_{d2}) &= (\beta_i (-Q_b + Q_r) + Q_{d2}) \cdot 10^{-6} \\
\beta_i &= \left(1 + \frac{[Buf_c]_T K_{Buf_c}}{(K_{Buf_c} + [Ca_i^{2+}])^2} \right)^{-1}
\end{aligned} \tag{3.6}$$

The β_i term was added in order to be consistent with the evolution of intracellular calcium ODE by incorporating the fluxes scale due to *rapid buffering approximation*. Rapid buffering approximation is based on the fact that the Ca^{2+} binding to the different buffers in the intracellular space is rapid with respect to diffusion time [57]. This leads to scale the different current and fluxes, which depend explicitly on $[Ca_i^{2+}]$, with β_i in order to incorporate the equilibrium between Ca_i^{2+} and buffers at each spatial point. That is why only Q_b and Q_r are scaled due to

their dependence on Ca_i^{2+} concentration. The term 10^{-6} in (3.6) was added in order to adjust the function to the same units of the Ca_i^{2+} ODE of the respective ionic model.

For the JRW model, two important points were taken into account. Firstly, as for the TNMP model, an extra term B_i (equation (3.6)) was also added to take into account the buffering of the intracellular calcium. The function $F(Q_b, Q_r, Q_{d2})$ is almost identical to (3.6). Only β_i is modified and defined by the respective relation (3.7) (the relation takes into account the buffers implemented originally on the JRW model).

$$\beta_i = \left(1 + \frac{[CMDN]_{Tot} K_m^{CMDN}}{(K_m^{CMDN} + [Ca_i^{2+}])^2} \right)^{-1}. \quad (3.7)$$

Secondly, the treatment of the crossbridges dynamics requires the modification of some equations of the ionic model. Indeed, the original model takes into account the presence of high- and low-affinity binding sites of the troponin, involved on the muscular contraction into the calcium dynamics. Some studies [58], [59] concludes that the regulation of the contraction is related to the low-affinity binding sites. Consequently the ODE linked to $[LTPRNCA]$ might be modified in order to include the mechanical influence on the fraction of occupied low-affinity binding sites. To this end, the equation was modified in the following manner:

$$F(Q_b, Q_r, Q_{d2}) = (\beta_i (-Q_b + Q_r) + Q_{d2}) \cdot 10^{-6}$$

$$J_{LTPRN} = Q_b = Y_1[Ca^{2+}] ([T]_t - [TCa] - [TCa^*] - [T^*]) - Z_1[TCa], \quad (3.8)$$

where Y_1 and Z_1 denote the k_{LTPRN}^+ and k_{LTPRN}^- parameters on the original ionic model. Consequently, their values are modified to follow those of the ionic model (Table 3.3).

3.2.2 Contraction protocols

The last important point to mention is the implementation of the contraction protocols used in this work. The following protocols have been implemented:

- Isometric contraction
- Isosarcometric contraction
- Isotonic contraction

Isometric contraction is based on the fact that the muscle dynamics is done at constant muscle length (L_m), while isosarcometric contraction keep the half-sarcomere length (L) under constant value. Dynamics at a constant force load are called isotonic contractions. In our case, the isotonic contraction regroups two different mechanical experiments, where one of their step follows an isotonic experiment. The two experiments are called: *afterloaded contraction* (AC) and *quick-release* (QR). Those experiments follow the typical procedure described below:

- **AC:** isometric → isotonic → isometric
- **QR:** isometric → force step (ΔF), isotonic → isometric

The principal difference (from a numerical point of view) between all contraction protocols is how the respective lengths (L_m and L) are computed. According to the contraction experiment simulated and NL model equations (Section 2.4.3), we implemented a particular Newton algorithm to compute the evolution of the muscle length. The two main equations that link L_m

to L are described in equations (2.35) and (2.36). Another formulation can be made in order to emphasize the lengths coupling and to facilitate the description of the Newton methods used. This formulation is given in (3.9).

$$\begin{aligned} F_s(L_m, L) &= \alpha \left(e^{\beta(L_m - L)} - 1 \right) \\ F_m(L) &= \hat{A} \cdot (L - X) + K(L - L_0)^5. \end{aligned} \quad (3.9)$$

Here \hat{A} is a time dependent constant equal to $A \cdot ([TCA^*] + [T^*])$ and F_s is modified by replacing L_s from (2.36) with $L_s = L_m - L$. In a isosarcometric experiment, the computation of L_m at time t^{k+1} is easily implemented by replacing the constant value L on F_s and solving the equation $F_m(L) = F_s(L_m^{k+1}, L)$. After some algebra, the following relation is obtained:

$$L_m^{k+1} = L + \frac{1}{\beta} \ln \left(1 + \frac{F_m^{k+1}(L)}{\alpha} \right) \text{ for } k \in \mathbb{N}. \quad (3.10)$$

The $k+1$ superscript of $F_m(L)$ indicates that the force is evaluated at time t^{k+1} through the \hat{A} parameter. However, and due to the fact that a pure implicit method requires the solution of a non-linear system, F^{k+1} is replaced by $F^{k+1,\prime}$ which it is computed after the predictor step given in (3.5).

In an isometric regime, the muscle length is kept constant at each time step $L_m^{k+1} = L_m^k = L_m$, for $k \in \mathbb{N}$. The sarcomere length, due to the mechanical activation by Ca^{2+} ions, will decrease and increase repeatedly according to the intracellular calcium concentration dynamics. To compute the length L , a Newton algorithm is employed to solve the non-linear function associated to isometric contraction ($i_{max} = 10$ in our case): (3.9).

$$\begin{aligned} G_{isometric}(L^{k+1}) &= F_m^{k+1,\prime}(L^{k+1}) - F_s(L_m, L^{k+1}) = 0 \\ G'_{isometric}(L^{k+1}) &= 5K(L^{k+1} - L_0)^4 + \hat{A}^{k+1,\prime} + \alpha\beta e^{\beta(L_m - L^{k+1})}. \end{aligned}$$

For $0 \leq i < i_{max}$:

$$L_{i+1}^{k+1} = L_i^{k+1} - \frac{G_{isometric}(L_i^{k+1})}{G'_{isometric}(L_i^{k+1})}, \text{ with } L_0^{k+1} = L^k. \quad (3.11)$$

In isotonic condition, only the force is kept constant and consequently all lengths can vary. Their computations are basically a combination of the two previous methods. The major difference resides on the fact that the F_m term, which represents the total force, is constrained to a constant value F_c . Therefore, the associated numerical algorithm is summarized in (3.12).

$$\begin{aligned} G_{isotonic}(L^{k+1}) &= F_m^{k+1,\prime}(L^{k+1}) - F_c = 0 \\ G'_{isotonic}(L^{k+1}) &= 5K(L^{k+1} - L_0)^4 + \hat{A}^{k+1,\prime}. \end{aligned}$$

For $0 \leq i < 10$:

$$L_{i+1}^{k+1} = L_i^{k+1} - \frac{G_{isometric}(L_i^{k+1})}{G'_{isometric}(L_i^{k+1})}, \text{ with } L_0^{k+1} = L^k.$$

Finally,

$$L_m^{k+1} = L^{k+1} + \frac{1}{\beta} \ln \left(1 + \frac{F_m^{k+1,\prime}(L^{k+1})}{\alpha} \right) \quad (3.12)$$

As for equation (3.11), the prime subscript indicates that \hat{A} is computed from the predictor step. One major difficulty in the implementation of AC and QR experiments is the transitions between the different steps of the procedure. These transitions were enabled by different conditions which are summarized on the following updated procedures (k , and l indicates some different time step in the simulation):

- **AC:** isometric $\xrightarrow{\text{if } F^{k+1} > F_c}$ isotonic $\xrightarrow{\text{if } L_m^{l+1} \geq L_m^0}$ isometric
- **QR:** isometric $\xrightarrow{\text{if } t_{change} \leq t^{k+1} \leq t_{change} + \Delta t}$ force step (ΔF), isotonic $\xrightarrow{\text{if } L_m^{l+1} \geq L_m^0}$ isometric

The transition between isometric and isotonic regime for the two experiments is done after that the dynamic system reaches a threshold value (as e.g. a constant force on AC or a specified time for the QR experiment, here taken at the time of maximum force). The time step on the condition transition for QR was added simply to ensure that the simulation time falls into the time interval and enables the contraction switch condition. The return to isometric conditions is allowed when the muscle goes back, after a contraction, to its initial length L_m^0 . At this time step, the length is kept constant and forced to be equal to L_m^0 .

Chapter 4

Results

4.1 Ionic Models

In the following Sections we will present some results obtained via the simulation data from the details presented in Chapter 3. The differences between our results and those provided in the literature will be presented and a validation of the quality of the simulated currents and potentials will be commented according to the theoretical part introduced in Chapter 2.

4.1.1 Ten Tusscher Model

Figure 4.1 presents the potential profile for the different ventricular cell types simulated by the TNTP model. Each of them exhibits the steady-state membrane potential for four different pacing frequencies (stimulation interval): 2.5 Hz (400 ms), 1.67 Hz (600 ms), 1.25 Hz (800 ms) and finally 1 Hz (1000 ms). The steady-state conditions are obtained by pacing the cell at a constant frequency during 67 seconds in order to stabilize the dynamics of the ODEs system. The resulting AP and Ca^{2+} curves are then selected from the last and complete action potential obtained from those simulation parameters. As it can be observed, the increase of the frequency affects both the steady-state AP duration and maximum depolarization potential obtained, irrespective of the kind of tissue. However, the effect is much more important in the M cells than in the others. This can be explained by the fact that M cell differs from epicardial and endocardial cells by presenting a smaller density on its I_{Ks} current [46]. As it was explained in 2.2.3, the I_{Ks} current plays a role in the repolarization phase together with an effect on the plateau phase duration. The small density of that current increases the time of phase 2, increasing as well the time of one cycle of the dynamical process. By a diminution of the diastolic interval, the system variables cannot reach their respective resting states and attain a lower frequency, leading to a decreasing in the amplitude of the response. This is observed in Figure 4.1f where the decrease of the diastolic interval leads to a decrease and a small phase shift on the calcium response. Moreover, it can be seen in Figures 4.3c and 4.3e, that the two repolarizing currents present a small shift in their rapid increase, delaying the repolarization of the membrane potential of M cells.

The difference between the potential profiles of the distinct cells is presented in Figure 4.2 for one specific pacing frequency (1.67 Hz). The APD of the M cell ($APD_{95} = 377.82$ ms) is bigger than those of the epicardial (310.60 ms) and endocardial (306.96 ms) cells as it was expected [36]. Contrary, the endocardial and epicardial cells do not present important differences. We only observe disappearance of the small peak after the rapid 0 phase depolarization. This is due to the fact that, in the model, the outward K^+ current (I_{to}) presents a lower density in the endocardial case [36]. The difference in APD between epicardial and endocardial is not observed as normally expected [19] and it is probably due to the fact that the I_{Ks} ionic current is slightly larger for the endocardial than for the epicardial one (Fig. 4.3d), even if the $I_{Ca,L}$ density drops (Fig. 4.3a).

Based on the parameters used in the simulation, the plateau phase is not clearly obtained. We observed from 4.1a, 4.1c and 4.1e an excessive increase of the potential after the spike, in contrast to the original paper of ten Tusscher & al. [24]. The main explanation that can be postulated is that the set of parameters used is not the same than those of the original paper (Table 3.1). Indeed, the parameters have an important influence on the shape and the dynamics of the curve, even if they affect only the maximal conductivities of the ionic currents, as it was seen for the M cell dynamics (Figures 4.2 and 4.3). However, the original parameters fail to provide a physiologically correct AP (data not shown). Furthermore, the original set of initial conditions was not provided and can, therefore, affect the dynamics of the ODEs system.

In order to have satisfactory results in the electro-mechanical coupling, one major point is the validity of the Ca^{2+} transient curves. Figures 4.1b, 4.1d and 4.1f present the results obtained at different frequencies. The rounded-off triangular shape is reproduced and the diastolic and systolic calcium concentration is on the range of experimental data measurements [24]. The major difference between the cells in the Ca^{2+} profiles is situated into the larger systolic peak and duration on the midmyocardial cells (Figure 4.2b). The maximum systolic concentration reaches in the M cell case: $1.2 \mu M$ while epicardial and endocardial is equal to $0.995 \mu M$. This small difference is principally due to the fact that the $I_{Ca,L}$ current (which is the major contributor) is open during a larger period than in the others myocardial cells (Fig. 4.3a). Moreover, the time of the inversion polarity of the Na^+-Ca^{2+} exchanger current occurs later than in the case of epicardial and endocardial cells. The inversion is synonym of the Ca^{2+} pumping outside of the cell leading to a diastolic calcium concentration. The larger time duration before returning to the rest conditions is due principally to the delayed phase 3 initiated by the rapid increase of the I_{Kr} (Fig. 4.3c) and $I_{K,1}$ currents (Fig. 4.3e).

Figure 4.4 presents the APD restitution curves obtained from the pacing protocols implemented and described in Chapter 3 (the basic cycle length for the standard protocol is equal to 600 ms). The use of the two models enables to verify that the results on the AP dynamics are consistent whatever the method used to stimulate the cell. As it can be seen in Figure 4.4, the restitution curve presents the same evolution of the APD_{95} for the three types of cell. The small decrease observed at lower frequencies (larger diastolic intervals) is only due to numerical instability, produced following a change on the stimulation interval. A larger number of S1 stimulus between variations on the diastolic interval could increase the results on the asymptotic behavior of those curves. Nevertheless, the typical curve shape and the results obtained are correct if we compare with the original paper [24]. The APD restitution curves shows more clearly the bigger AP duration and the rate dependance of the M cells. The respective maximum APD_{95} is reached at 403.3 ms in the standard protocol, while the dynamical one is equal to 412.0 ms. This small difference is probably due to the in silico conditions used in order to simulate the two distinct protocols. The results for the epicardial and endocardial cells are presented in Table 4.1.

<i>Cells type</i>	<i>Maximum APD_{95} from standard protocol [ms]</i>	<i>Maximum APD_{95} from dynamical protocol [ms]</i>
Epicardial	322.8	330.0
Endocardial	320.3	327.0
M cell	403.3	412.0

Table 4.1: Table of the maximum APD_{95} of the different simulated cells for the two kind of pacing protocols.

Figure 4.4 presents the maximum amplitude of the action potential throughout the different stimulation protocols, computed in different manners. In the S1-S2 standard protocol, the maximum potential is obtained by searching the highest depolarized potential triggered by the S2 stimuli. In the dynamical case, the maximum is obtained by the last S1 stimulus before the diastolic interval reduction. In the two cases, we observe that the potential reaches more or less

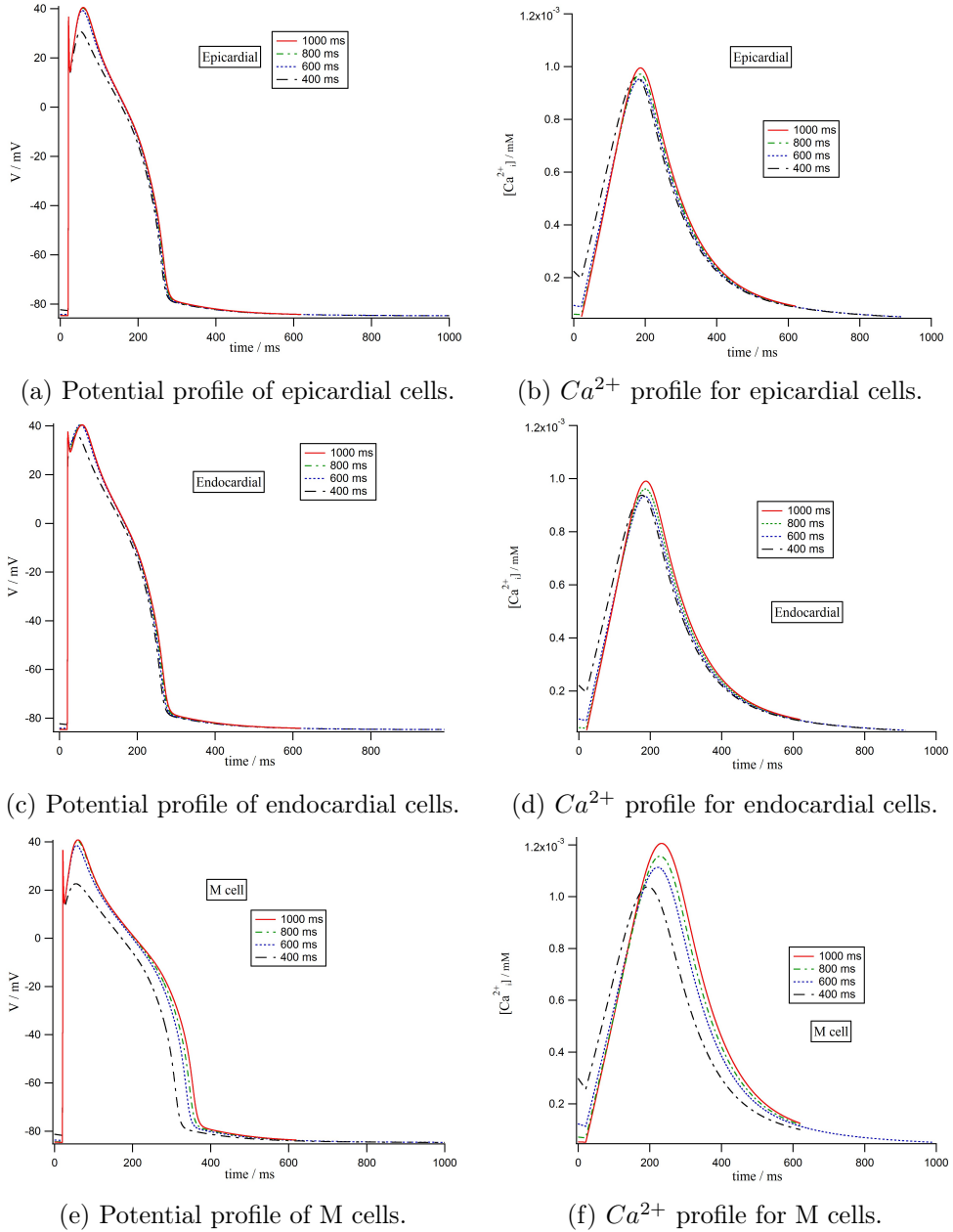
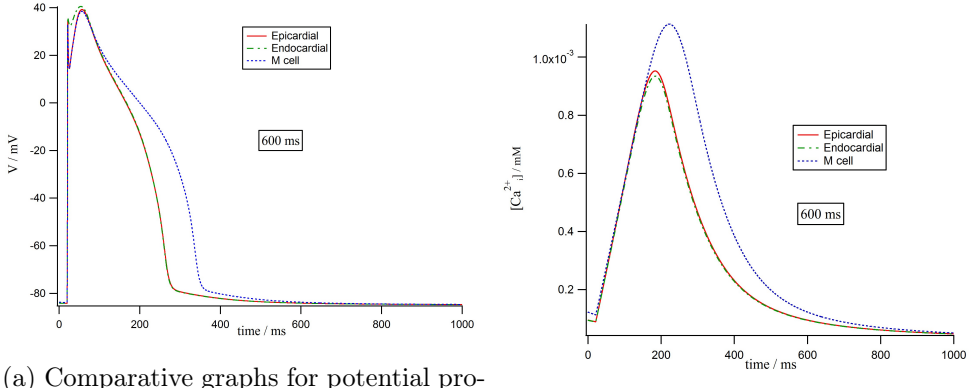


Figure 4.1: Steady-state potential (left panels) and Ca^{2+} profile (right panels) for the three kind of ventricular cells by ten Tusscher & al model simulations. The profiles have been computed for 400, 600, 800 and 1000 ms stimulation intervals.



(a) Comparative graphs for potential profile of ventricular cells.

(b) Comparative graphs for Ca^{2+} profile

Figure 4.2: Comparative graphs of the steady-state potential (left) and Ca^{2+} profile (right). The profiles have been computed for 600 ms stimulation interval (1.67 Hz).

the same value for the three kinds of cells, which differs from experimental observations [36]. Indeed, the error is largely associated to the spike-dome problem mentioned before, which alters the exact results on the maximum potential computed. Indeed, in physiological conditions, the maximum of the potential is normally reached at the end of the phase 0 of the action potential. However, the epicardial seems to have a smaller amplitude than the M cells as it was observed previously. Nonetheless, the somewhat contradictory results for the endocardial cells between the two methods do not allow to draw substantial conclusions. One point that can be confirmed is the general trend that the maximum potential increase with a decrease of pacing frequencies until reaching an asymptotic value. This kind of behavior was observed in various experimental results [55], [56].

Figure 4.5 presents the gating variables associated with their respective ionic currents obtained from the same simulation parameters as in Figure 4.1, for the epicardial cell at 600 ms stimulation interval. As expected, the I_{Na} presents a rapid peak shape, synonym a rapid Na^+ flux, during the phase 0 part of the action potential. Observing the I_{Na} gates dynamics in Figure 4.5a, we observe that the activation gate m rapidly increased while the j and h inactivation gate drops to zero. These features reproduce correctly some recent studies that suggest that the activation and fast inactivation gates are coupled, rather than sequential [35]. This property of sodium channel explains the rapid increase and drop of the inward sodium current. Further, the simulation reproduces correctly the inactivation rates of the channel according to the dynamics of j and h . Indeed, some experimental results confirm the fact that the inactivation process can be decomposed into two regimes: fast and slow inactivation [35], which is quite well described by the two respective variables.

The delayed rectifier currents are also quite well reproduced according to the data obtained with the original paper [24]. The difference in the time interval response is largely due to the fact that the simulation in the original paper is done at 1 Hz pacing while the results presented here is around 1.67 Hz.

The rapid spike current in the I_{Kr} is as the sodium current causes by the coupled and rapid increase-decrease of the gating variables associated. These fast activation gate process is typical of the rapid component of delayed rectifier current [60]. The decrease of the activating gate variable leads to the diminution of the rapid inward current, after the inactivation gate returns to resting values. The slow component presents an initial slow rate activating process together with a rapid decrease of the activating gate, commonly measured in experiments [60]. This dynamics leads to have a slow increase of ionic current compared to I_{Kr} , but oppositely to a faster deactivation of I_{Ks} than the rapid component. Finally, the transient outward current (I_{to}) displays an evolution quite similar to the I_{Na} current resulting to the same kind of peak shape

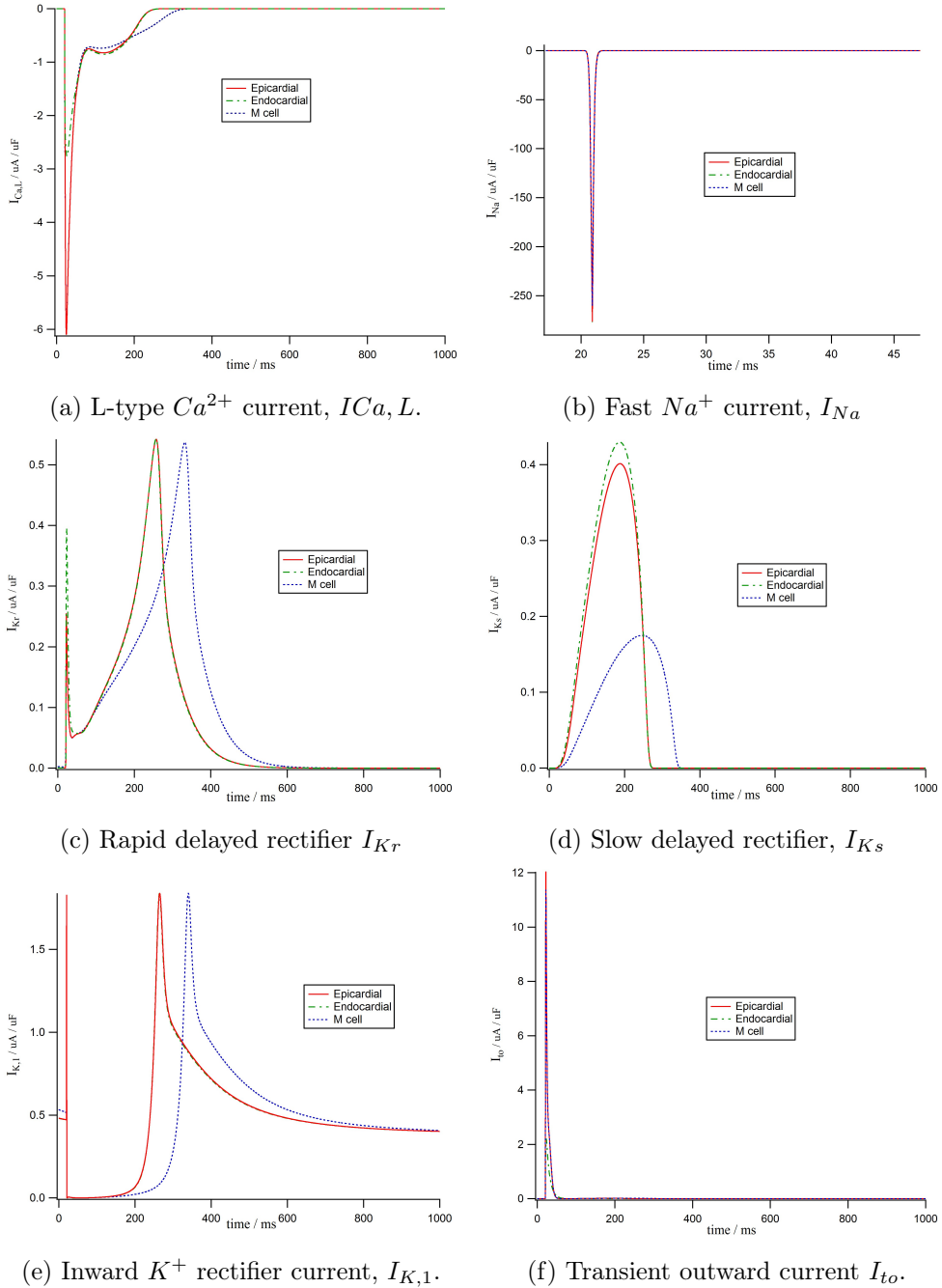


Figure 4.3: Comparative graphs of the steady-state currents dynamics for the three ventricular cells.

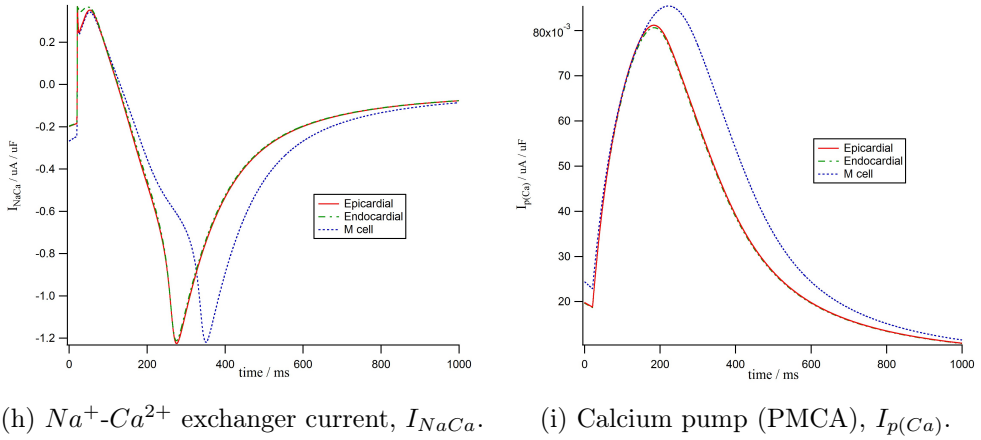


Figure 4.3: Comparative graphs of the steady-state currents dynamics for the three ventricular cells (continued).

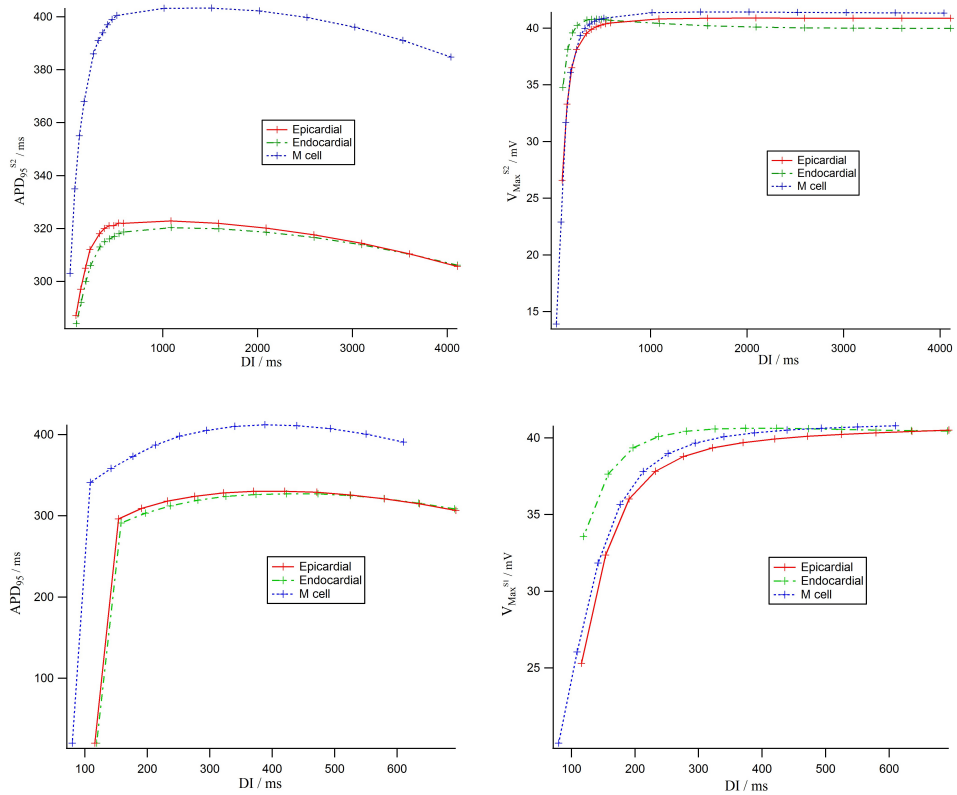


Figure 4.4: Action potential duration restitution curves (left) and AP amplitude profiles (right) obtained via the two pacing protocols : S1-S2 standard restitution (top) and dynamic protocols (bottom).

profile, and a little contribution to the phase 3 repolarisation phase [60].

Finally, the dynamics of the L-type calcium current is presented in Figures 4.5k and 4.5j. As it was mentionned in Section 2.4.2, d , f and f_{Ca} represents respectively the activation, the voltage-dependent and calcium-dependent inactivation gates. As observed in Figure 4.5j, after the triggered depolarization, the activation gate augments instantaneously while the f and f_{Ca} inactivation gates decrease slower. This rapid modification leads to the rapid increase of calcium diffusion into the cell, leading to the spike-dome phase 1 repolarization process in the membrane potential. Then, the activating gate begins to diminish before the inactivation gating variables reach their minima. The final increase of f and f_{Ca} makes the channel impermeable to calcium, stopping therefore the respective current.

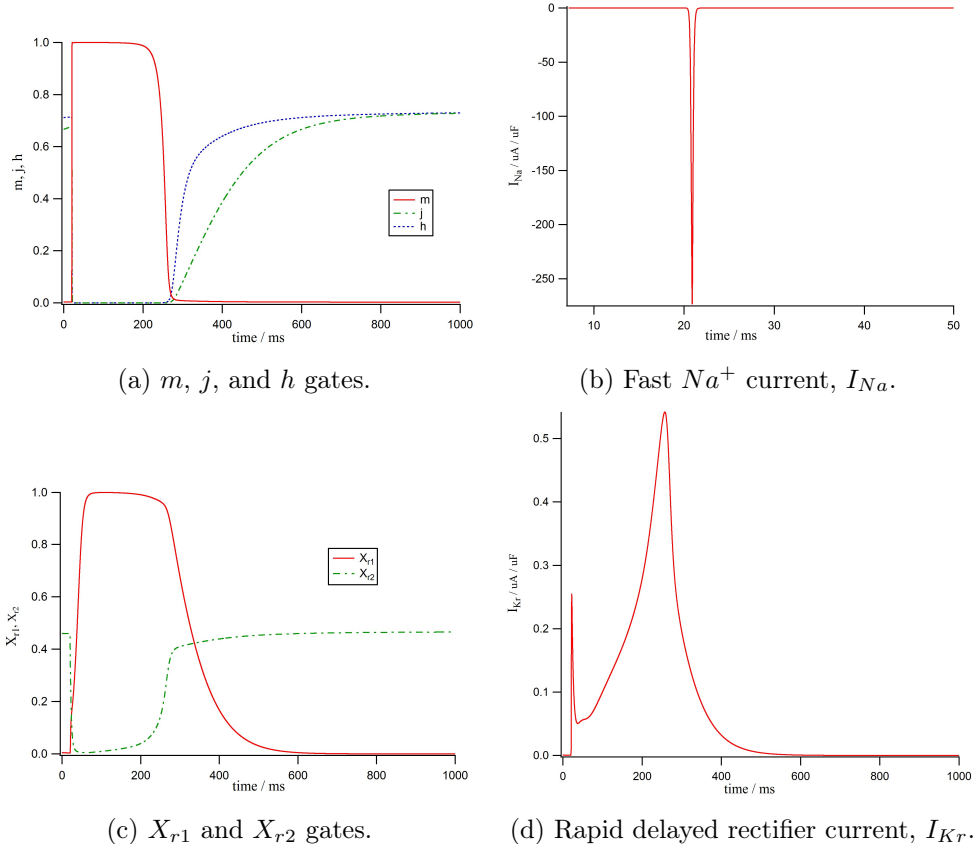


Figure 4.5: Gating variables and associated currents obtained by simulation of ten Tusscher & al. model at 600 ms stimulation interval for the epicardial cell.

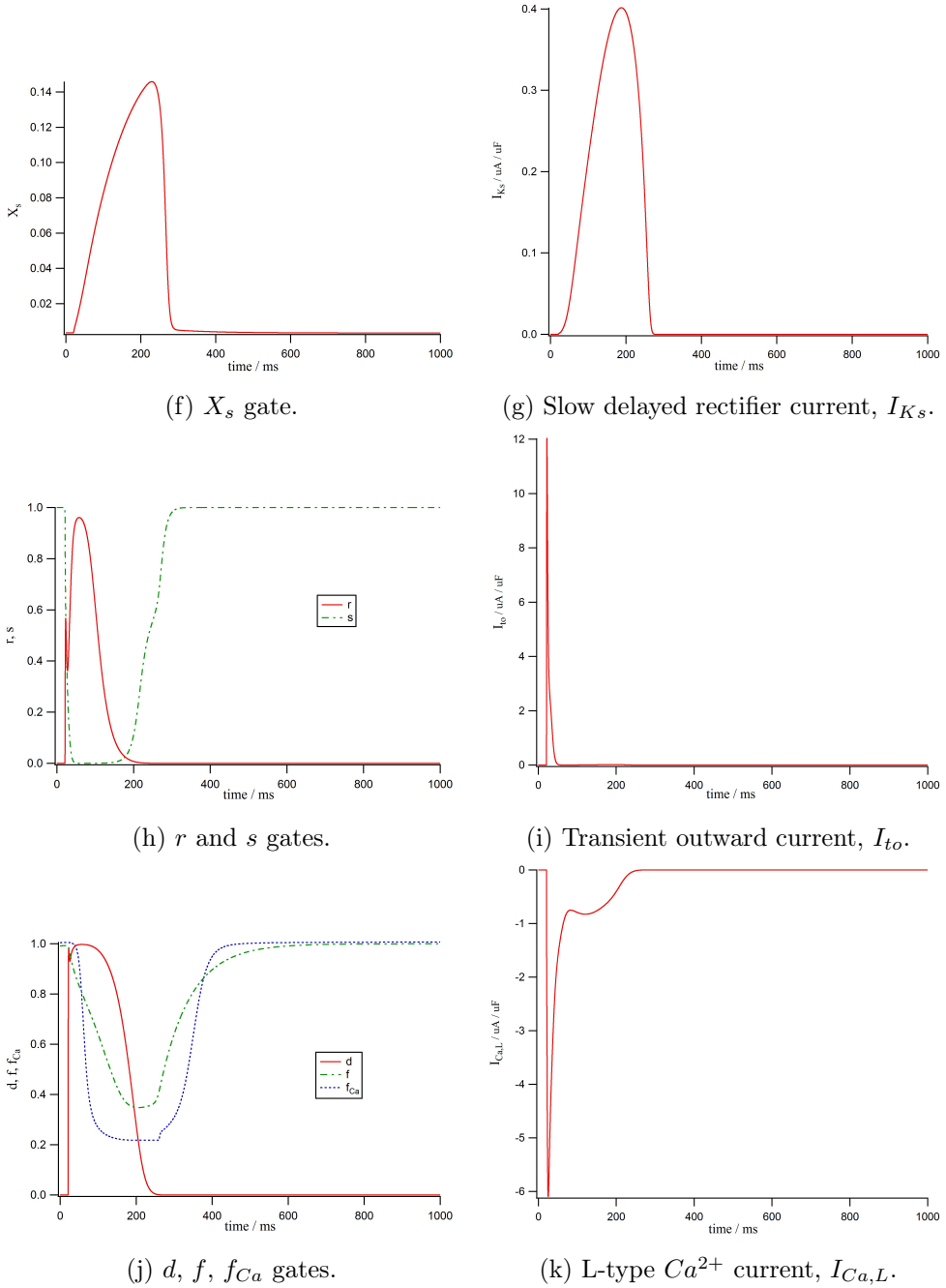


Figure 4.5: Gating variables and associated current obtained by simulation of ten Tusscher & al model at 600 ms stimulation interval for the epicardial cell (continued).

4.1.2 Jafri-Rice-Winslow model

Before presenting the different results obtained by the JRW model, let us focus on the numerical analysis of the results obtained. As said in Section 3.1.1, the choice of the used time step was enabled by comparison of results between the FE and the RK4 numerical integrators. In TNNP model, the analysis was performed with a FE method where only the time step was modified. The results obtained (not shown) have not displayed significant difference between those results (the interval time step used spreads over 10^{-2} and 10^{-3}). Here the analysis emphasizes a particular problem obtained with this cell model. Indeed, it can be observed that the intracellular calcium dynamics does not return to identical diastolic concentrations after each action potential as it can be seen in Figure 4.6. Furthermore, we observe that the systolic peak increases also (but more rapidly than the diastolic one) throughout the simulation time. To ensure that it is not only due to the numerical integrator, a comparison between two explicit integrators was made. The choice to use explicit methods is to avoid large computational cost to solve the 30 nonlinear ODEs system by using implicit methods, even if they present better stability domain. However, the results obtained display that these abnormal behaviors on the calcium dynamics are observed whatever the numerical integrator used and no matter how small the time step can be (the time step has been decreased until $7.5 \cdot 10^{-5}$, without particular improvements).

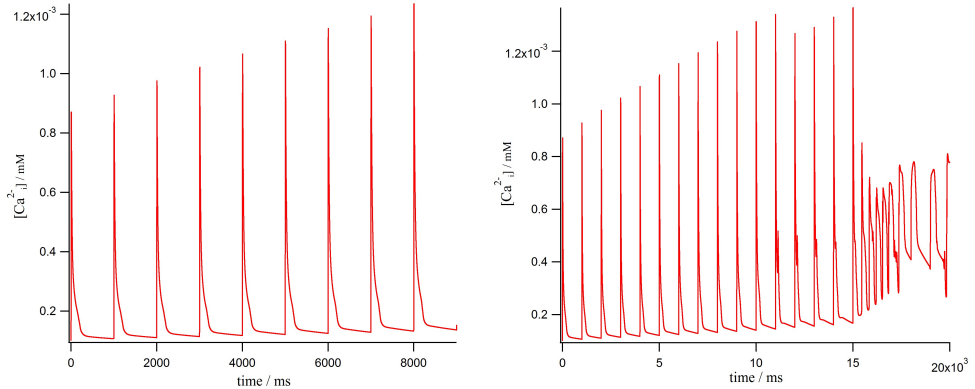


Figure 4.6: Ca_i^{2+} profiles obtained from JRW model computed with FE (left) and RK4 (right) method with constant time step $\Delta t = 10^{-4}$.

Figure 4.7 presents the different Ca_{NSR}^{2+} - Ca_{JSR}^{2+} profiles obtained with both implemented numerical integrators. It was obtained (as the results for Fig. 4.6) with a simulation performed with a constant time step of $\Delta t = 10^{-4}$, a total time simulation of 100000 ms and with a stimulation frequency of 1 Hz. The observation of Fig. 4.7 explains, partially, why the systolic Ca_i^{2+} peak increases with time. Indeed, we observe an incremental augmentation of the sarcoplasmic calcium concentration due mainly of both the too slow recovery for the Ca_{NSR}^{2+} and the fast one of Ca_{JSR}^{2+} , which leads to tend to increase the diastolic level of those ions. This augmentation leads finally to instability of the solution and finally to blows up around 4000 ms for FE and 20000 ms for RK4 method. This time difference might be explained by the better absolute stability of RK4 method compared to FE one [61], and its better numerical precision.

Those results lead to the conclusion that the ionic model can present some problems on its parameter values or initial conditions. Indeed, some of them have been modified due to the fact that the original ones fail to provide physiological results. Unfortunately, we have not been able to find the correct parameters value in order to correct these problems and get correct physiological data.

Despite this major problem, a large part of the simulated results are, however, consistent with experimental ones and those of the original paper of the JRW model. For that reason, we will describe despite the difference and the results obtained throughout all cell simulations and

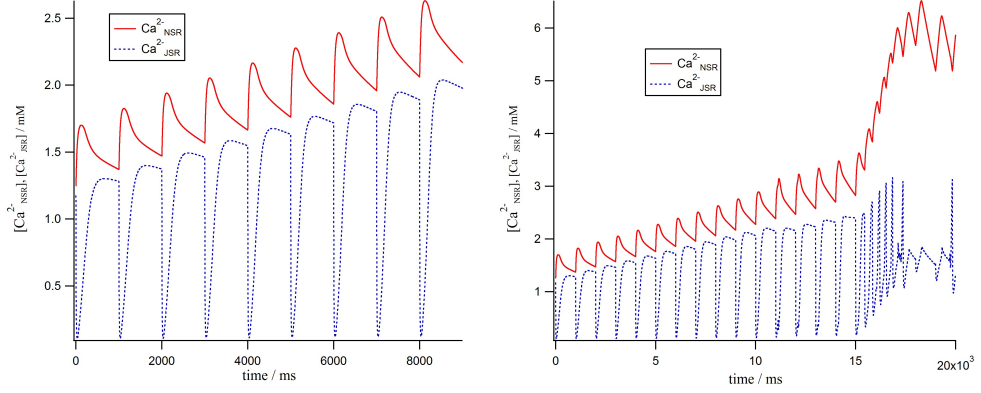
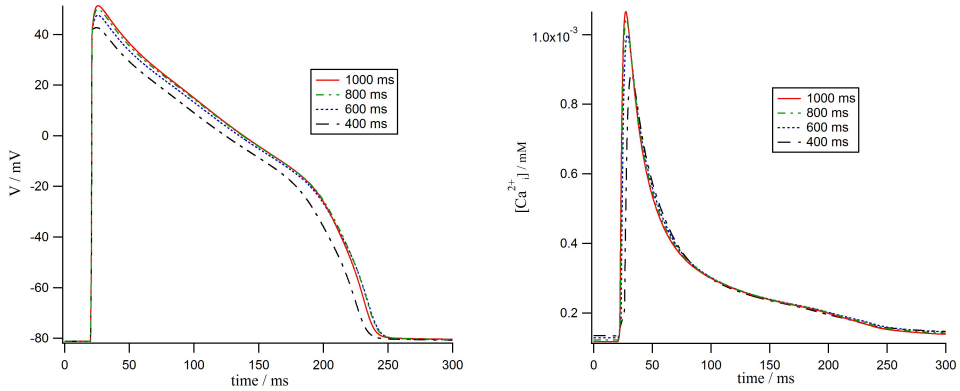


Figure 4.7: Ca_{NSR}^{2+} - Ca_{JSR}^{2+} profiles obtained from JRW model computed with FE (left) and RK4 (right) method with constant time step $\Delta t = 10^{-4}$.

compare them with those of TNNP.

As in the ten Tusscher model & al., the pacing frequency affects the AP, as described in Figure 4.8. Due to the previous problem, it was not possible to use the data after a long and constant pacing protocol, in order to stabilize the output. Therefore, the data presented in Figure 4.8 are selected from the 3rd stimuli for all the selected frequencies. The choice was taken in order to avoid the non-steady potential profiles that the first stimuli presents (data not shown) while keeping as much as possible concentrations in the physiological range. As it can be seen in Fig. 4.8a, the modification of the frequency affects slightly the AP duration and amplitude of the cell. An increase of the frequency leads to a parallel decrease of the action potential duration and amplitude as seen for the previous model. In the same time, the stimulation interval affects weakly the calcium transient dynamics of the cell by decreasing the systolic peak concentration and affecting slightly the time delayed for the bigger pacing frequency (400 ms) as it was reported in [45].



(a) Potential profiles for different pacing frequencies. (b) Ca^{2+} profiles for different pacing frequencies

Figure 4.8: Comparative graphs of the steady-state potential (left) and Ca^{2+} profiles (right). The profiles have been computed for 400, 600, 800 and 1000 ms stimulation intervals.

One major point of the JRW model is its detailed model of the calcium sub-system including a large system of channel states. For this reason, and in order to verify the results according to the theory, the evolution of the major components was presented in Figure 4.9. The results presented have been computed in the same way as the Figure 4.8. Figures 4.9a and 4.9b displays

the proportion of the L-type Ca^{2+} channel in one of the states described in Section 2.4.2. A first point to mention is the important value taken from the variables C_0 and C_4 , which spread over the $[0, 1]$ interval. This is due to the gradual increase of the diastolic calcium concentration. However, the evolution of those variables seems to be correct from a biological point of view. Indeed, after the triggering of the stimulus, the channel evolves rapidly from closed state C_0 to the closed state C_4 promoting a large portion of the ionic channels to a states which can make transitions to the open state O or the mode Ca^{2+} closed state C_{Ca4} . These rapid transitions can be seen in figures and 4.9a and 4.9b by the parallel augmentation of the respective channel states. This effect, which presents some delay from the stimuli time, leads to the release of calcium from the sarcoplasmic reticulum during the phase 1 and 2 of the action potential (see figure 4.9d). During the liberation of Ca^{2+} in the sub-space part, the γ term (see equation (5.30)) lead to an increase of the proportion of mode Ca^{2+} in parallel to the redistribution of the channel states through the different states. This mode presents a very infrequent opening (here, horizontal line equal to 0, due to the chosen parameters). These observations are in accordance to experimental results [45] which found that the L-type Ca^{2+} type is inactivated by local calcium concentration. As it was described in Section 2.4.2, the mathematical formulation of the transitions between states favors the mode Ca^{2+} with the depolarization of the cell, in order to simulate the voltage-dependence of the channel. This is displayed by the rapid increase of C_{Ca4} state in figure 4.9b. The voltage-dependent part is also modeled through the y gating variable for the $I_{Ca,L}$ current. The diastolic (0.499) and systolic value (0.019) are consistent with the values obtained from the original paper [45].

The second aspect of the calcium system is the CICR (calcium-induced calcium-release) modeled through the RyR channel and a four states system that the results are presented in Figure 4.9e and its respective current in 4.9f. At low Ca^{2+} concentration, the channel is largely on P_{C1} closed state preventing possible calcium release from the junctional sarcoplasmic reticulum [50] and illustrates by a zero flux value. When the L-type channel opens around 50 ms and leads to a rapid increase of calcium in the sub-space part, the RyR receptors react by a rapid and short transition from P_{C1} state to the first open state, P_{O1} . This is represented in the channel states' profile (Fig. 4.9e) by a peak of P_{O1} and P_{O2} states population and a parallel decline in the proportion of receptors in the P_{C1} state. After a short delay, a part of the channel inactivates slowly the P_{C2} state. This transition between close-open-close pathway illustrated the adaptation characteristics of the ryanodine receptor and constitutes the base of the CICR phenomenon [50]. The high dependence on calcium concentration (equation (5.47), paragraph 2.4.2) of the transitions' rates for P_{C1} to P_{O1} and P_{O1} to P_{O2} enables the receptor to establish a positive feedback mechanism according to the level of Ca^{2+} .

Figure 4.10 presents the different principal currents obtained with JRW model. Figure 4.10 presents the two last ionic channel currents where their conductance are directly dependent on the evolution of the gating variables. We can observe that the results are consistent with physiological experiments and those obtained with TNNP model. Indeed, the dynamics of m , j and h gates associated to the fast Na^+ channel is very similar with those obtained with TNNP. Due to the depolarization of the membrane, m activation gate population increase rapidly while the two others drop quickly leading to a transient and rapid release of sodium ion. This can be explained mainly to the fact that the dynamics of that channel is described by quite identical relations based on the Luo-Rudy model [45], [48] (see Appendix). The time dependent K^+ current is almost similar to the I_{Ks} one described in TNNP model. It displays the typical slow deactivation kinetics associated to slow rectifier current (Fig. 4.10c) [60]. Moreover, this amplitude is situated on the range given by the original paper [45].

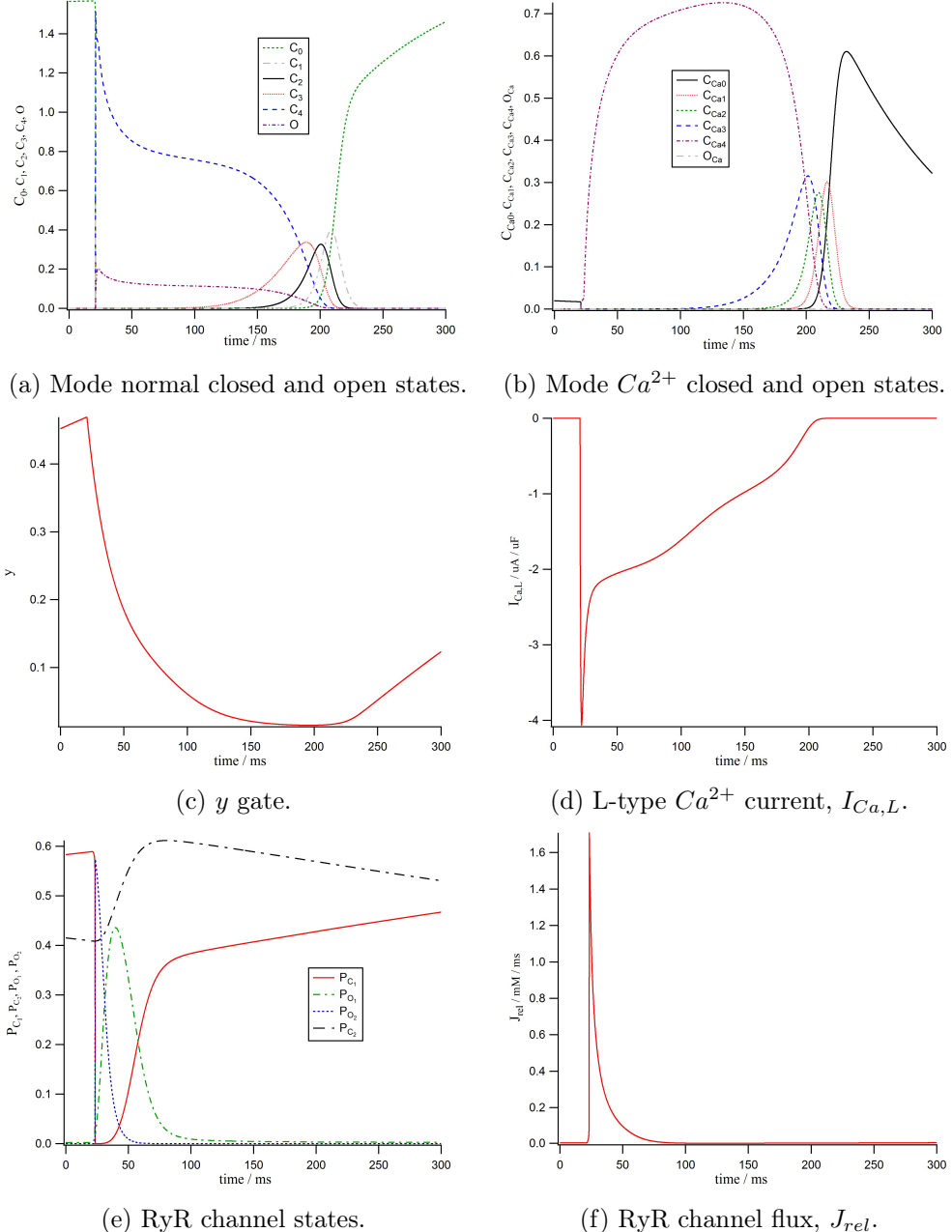


Figure 4.9: Dynamics of the calcium sub-system simulated by the JRW model at 600 ms stimulation interval.

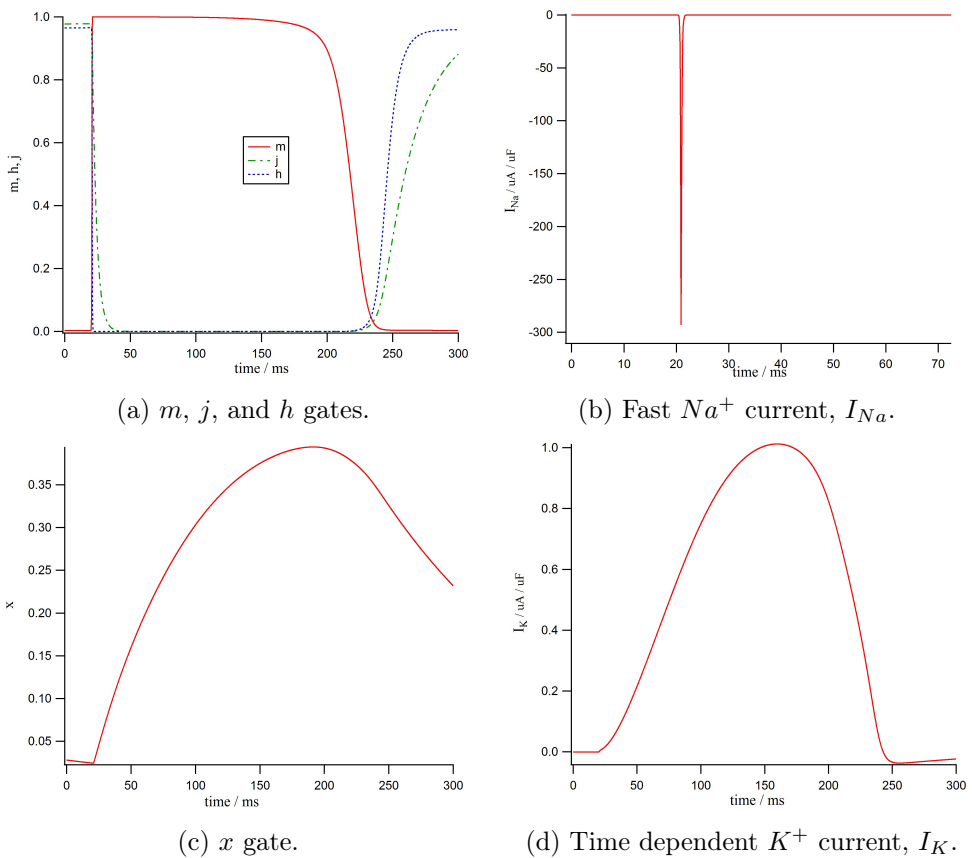


Figure 4.10: Gating variables and associated currents obtained by simulation of JRW model at 600 ms stimulation interval.

4.2 Cardiac Electromechanical model

This Section will present the different results computed from the NL model coupled with the two ionic ones described above. We will begin with a brief discussion of the tetanic calcium concentration results in order to check the reproducibility of the model and compare it to the obtained results on the NL paper [18]. Secondary, we will introduce the results obtained from the different contraction protocols described in Section 3.2.2 and compare them to reference [18] and some physiological experiments. We finally compare the results between each of the coupled models and provide some possible explanations on the difference that will be observed.

4.2.1 Dynamic behavior with constant $[Ca^{2+}]$

The first step of the analysis of the mechanical model is to ensure that the model parameters, and more importantly, the model itself can be reproduced with our simulations. For this purpose, we perform a simulation of a cardiac muscle in tetanized conditions ($[Ca_i^{2+}] = 2\mu M$) as [18]. Two principal contraction experiments have been performed: an isometric contraction with step length (ΔL) ranging from -0.005 to 0.001 μm and an isotonic contraction with force step decrease ranging from -75 to 0 $mN \cdot mm^{-2}$.

Figure 4.11 presents the results obtained from the first contraction protocol. As expected, we observe the four phases of force response observed in [18]. After an abrupt change on the half-sarcomere length (here: $-0.003\mu m$) (L), the force decreases rapidly to a minimum value, noted F_1 (phase 1). Then and quickly, the force recovers to a partial value (F_2) defined at the point where the slope recovery changes drastically (Fig. 4.11) as reported in different references [17], [62]. Finally, tension restores slowly to a new isometric force, whose value depends on the final half-sarcomere length and troponin states distribution reached after the end of the step length (phases 3 and 4). The rapid decrease of length provides a parallel diminution of the tension on the crossbridges' arm, that leads to the observed tension diminution. This was observed by the rapid increase of T_{Ca} population with an opposite decrease of T_{Ca}^* and T^* concentration (data not presented). Indeed, the diminution of the tension enables the crossbridges to detach, leading to new distribution of the troponin state populations, which can be observed by the rapid change in the crossbridge elastic elongation h ([18], Fig. 4.12), which represent the elongation of the equivalent crossbridge defined on Section 2.4.3. The rapid phase 2 recovery was the consequence of the recovery of h to its resting position h_c . As reported [18], the phase 3, which corresponds to a slight decrease after the partial recovery, is also not observed by this model.

The different force response to a step length is summarized in the stiffness diagram given in Figure 4.11 (right). As expected, we observe a linear behavior of F_1 (open circles) as function of step length. Moreover, and as reported in [62], F_2 is almost horizontal for small values of ΔL , indicating that the recovery is almost complete when the perturbation is small enough [62], given this nonlinear shape of the curve.

The other experiment consists of a rapid decrease of an initial and constant force value F_m , taken here equal to 90 $mN \cdot mm^{-2}$. The different force steps ($\Delta F \in [-75, 0]$) and the resulting effect on the half-sarcomere length is summarized in Figure 4.13. As it can be seen, isotonic contraction leads to a respective decrease of L where the shortening speed depends on the force step applied. This effect reflects the elastic properties of the attached crossbridges of the model [18]. After this rapid change on the sarcomere length, a more slowly shortening is observed. This phase is mainly due to both the dynamics of h , which returns to its steady state value h_c , and the troponin C states where the proportion of detached myosin heads increases with the value of ΔF [63]. However, the different dynamic phases observed in [64] was not well reproduced and can be due to an oversimplification of crossbridges dynamics, as suggested in [65].

Even if some physiological results have not been reproduced exactly, the results are in agreement with those obtained in the original NL model and can consequently be used for the coupling

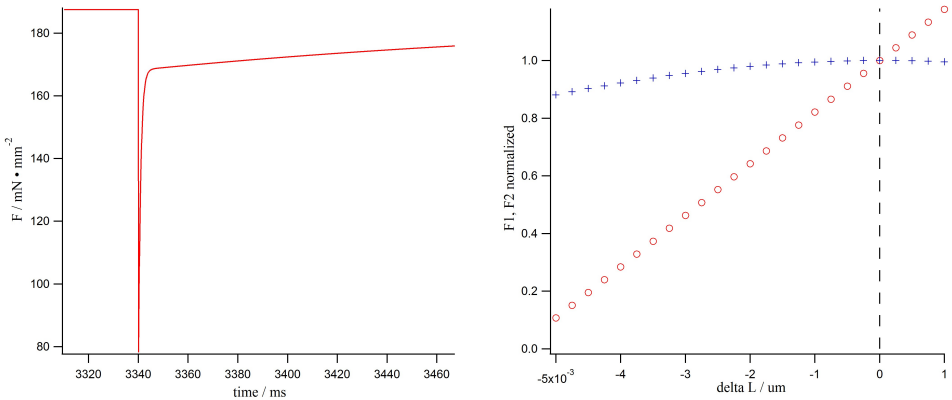


Figure 4.11: Left: Muscle force response (F_m) to a step length (L). The step amplitude is equal to $-0.003 \mu\text{m}$ for a duration of 0.02 ms . Right: Stiffness diagram obtained from step length ΔL ranging from -0.005 and $0.001 \mu\text{m}$. Open circles represent the minimum drop force (F_1), while crossed points represents the force from quick partial recovery F_2 . F_1 and F_2 was normalized with respect to steady state isometric force.

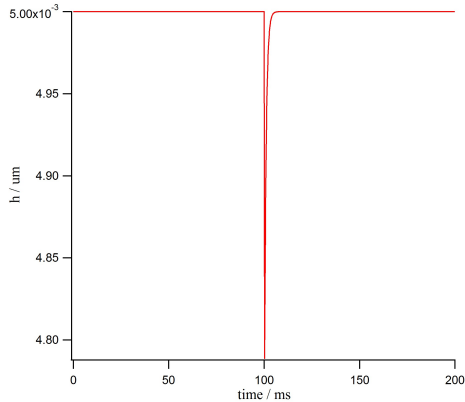


Figure 4.12: Profile of the crossbridges elastic elongation h for a length step of $-0.003 \mu\text{m}$ and $[Ca^{2+}] = 2 \mu\text{M}$.

part in order to simulate the interaction between the ionic model and the contraction one.

4.2.2 Dynamics of electro-mechanical coupled models

Firstly, and before making any experimental contraction, it is important to described the results obtained at isometric contraction and see their relevance according to theoretical considerations. One major point to reproduce is the delay time interval that governs the different part of the contraction mechanism (Section 2.4.3): the formation of an AP triggers a rapid release of sarcoplasmic calcium on the cytosolic part. The calcium diffuse finally to the troponin complex and enables the formation of muscular contraction. As Figures 4.14 and 4.15 present, these different components of the contraction mechanism are well reproduced for the two different coupled model. The force and the potential curves are normalized with maximum peak value, for sake of clarity. Those figures present the results of an isometric contraction simulation of three cardiac beats at 1 Hz pacing frequency, at $1.05 \mu\text{m}$ half muscle length (L_m). We can observe that the first cardiac beat presents a different behavior on the force response, mainly due to the non-steady stimulation response of the ionic model. Moreover, the slight increase of muscle force observed on the JRW model is due to the incremental increase of the calcium systolic peak, that was mentioned above. The first difference that exists between the two different models is the

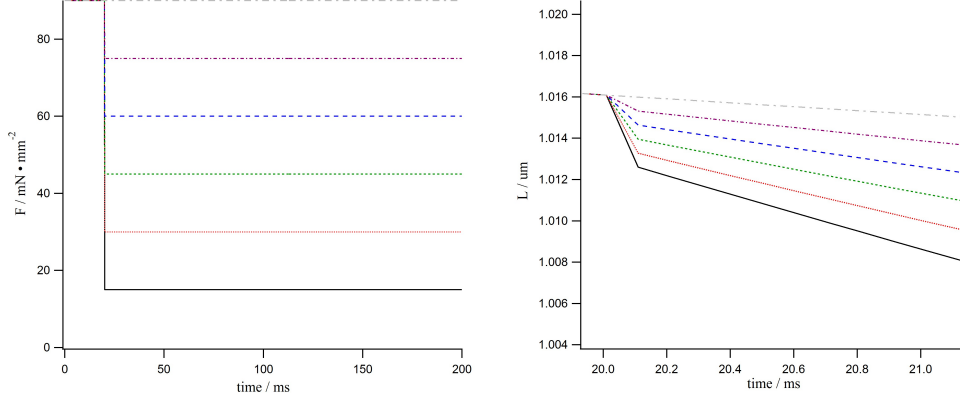


Figure 4.13: Left: Different isotonic force step applied ranging from -75 mN to $0 \text{ mN} \cdot \text{mm}^{-2}$. Right: Associated half sarcomere L response to force step.

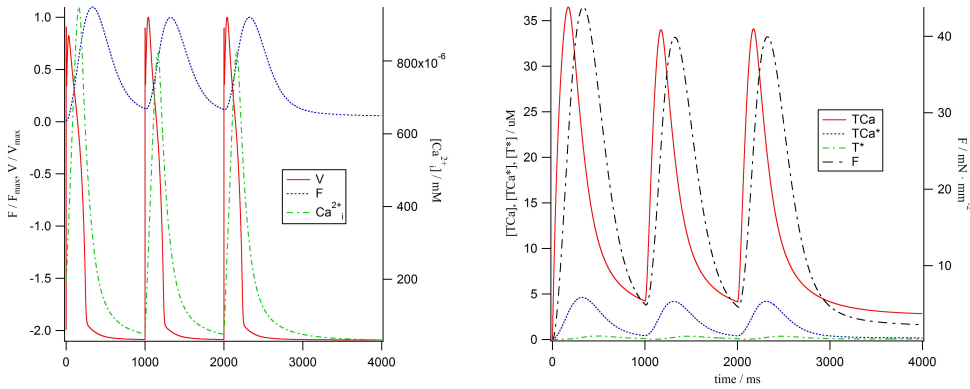


Figure 4.14: Isometric contraction at 1 Hz pacing frequency for the TNNP coupled model. Left: Simulation V , Ca_i^{2+} and F profiles. The force and the potential are normalized by their respective maximum value. Right: Respective TCa , TCa^* , T^* troponin state evolution with total force profile.

duration and the amplitude of the force generated by the muscle. Indeed, it can be observed on the left Figures 4.14 and 4.15 that the force reaches a systolic peak of around $39.93 \text{ mN} \cdot \text{mm}^{-2}$ for the TNNP and around $20.41 \text{ mN} \cdot \text{mm}^{-2}$ for the JRW models. This difference is mainly due to the transient calcium dynamics which presents a lower duration on the JRW model. Indeed, we can observe from the left panels of Figures 4.14 and 4.15 that the proportion of active states does not reach subsequent concentration values high enough to lead to great force generation. This is explained by the fact that the delay on the formation of active states prevents a rapid increase of their population during the time where intracellular calcium concentration is sufficiently high for activating the contraction. This can be seen by the comparison on the TCa and TCa^* evolution for both ionic models. The proportion of TCa stays high for sufficient time in the TNNP model while it presents a rapid transient peak on the JRW case. This rapid evolution does not allow to form sufficient active states (TCa^* , T^*), which returns rapidly to diastolic level, contrary to the TNNP model. This results confirm some biological results that the calcium dynamics can influence the developed force of the contractile unit [66].

Another point important to measure is the contribution of total muscle length on the total force F profile, measured at isometric contraction. It was now well known that the preload state (initial muscle length) of the cardiomyocytes can alter the contractile performance of the muscle [67], [68]. From a biological point of view, preload state is defined according to the amount of filling of the heart during the diastolic interval. The qualitative measure of this effect is generally

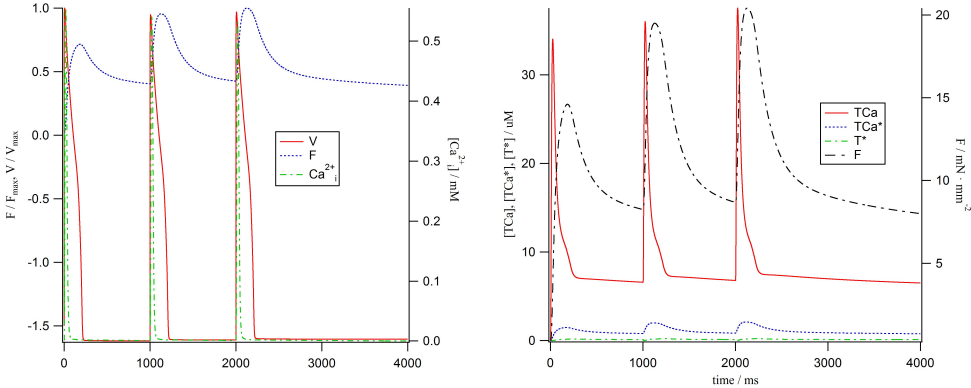


Figure 4.15: Isometric contraction at 1 Hz pacing frequency for JRW coupled model. Left: Simulation V , Ca_i^{2+} and F profiles. The force and the potential are normalized by their respective maximum value. Right: Respective TCa , TCa^* , T^* troponin state evolution with total force profile.

presented on an *isometric-length tension curve*. This curve presents the value of the systolic and diastolic force of the cell with respect to the initial preload. In order to check if the model suited well physiological results, a series of 13 isometric contractions were performed form different L_m values, ranging from 0.85 to 1.15 μm . The associated results for both coupled models are presented on Figures 4.16 and 4.17. As expected, the gradual increase of the initial preload value leads both to systolic peak and diastolic level force augmentation [67], [68]. However, and it was observed in Figure 4.17, the resting force value of the JRW model simulation increases too rapidly with L_m , which does not agree with physiologically data. This problem is principally due to the incremental augmentation of intracellular calcium peak for each contraction beats simulated. This increase leads the active states to reach bigger systolic values leading to the normal increase of generated force. However, due to dynamics of the active states, which follows mainly those of Ca_i^{2+} , the system does not recover entirely to the baseline value at the end of relaxation process. As the force length affects the dynamics of active states through $[TCa]_{eff}$ (equation (2.32)), the augmentation of the active state baseline population is enhanced and leads finally to the observed non-physiological results. However, the trend that efficiency of force increases initially with small length and tends to decrease for bigger length was obtained from both coupled models. Indeed, while the systole force increases directly with length, the diastolic one stays almost constant for lower L_m values (TNNP). At L_m 's values bigger than 1.10 μm the resting force begin to increase rapidly, reducing gradually the generated force efficiency. This is explained largely by the sarcomere structure on general muscles [67]. Indeed, in case of too large muscle length, the superposition of the thick and thin filaments is not optimal and tends to be equal to zero if the associated half sarcomere length is bigger than the normal length of actin filament. Reducing this length allows a superposition of the filaments and then a generated tension created by the crossbridges attached. On the other hand, too small muscle length tends to produce non-optimal conditions on the overlapping of both protein filaments [69]. In our case, this effect is modeled through the effective rate of crossbridges' attachment through $[TCa]_{eff}$ (2.32), which is reduced in a symmetrical way when the half-sarcomere length L gets away from the optimal one L_a taken equal to 1.17 μm .

A further experiment from [18] is the estimation of TCa (troponin Ca^{2+} complex) time course by using a ΔL_m pulses step. As in [18], pulses of total muscle length ($\Delta L_m = 0.04$, time duration: 20 ms) have been performed at different times during the course of a isometric contraction ($t_{step} = 2024.5 + 100k$, $k = 1, \dots, 7$). The two models presents a similar of behavior to muscle length pulses (Fig. 4.18a and 4.19a). The sudden change on muscle total length leads to a rapid force response that follows the different phases explained on the tetanized model

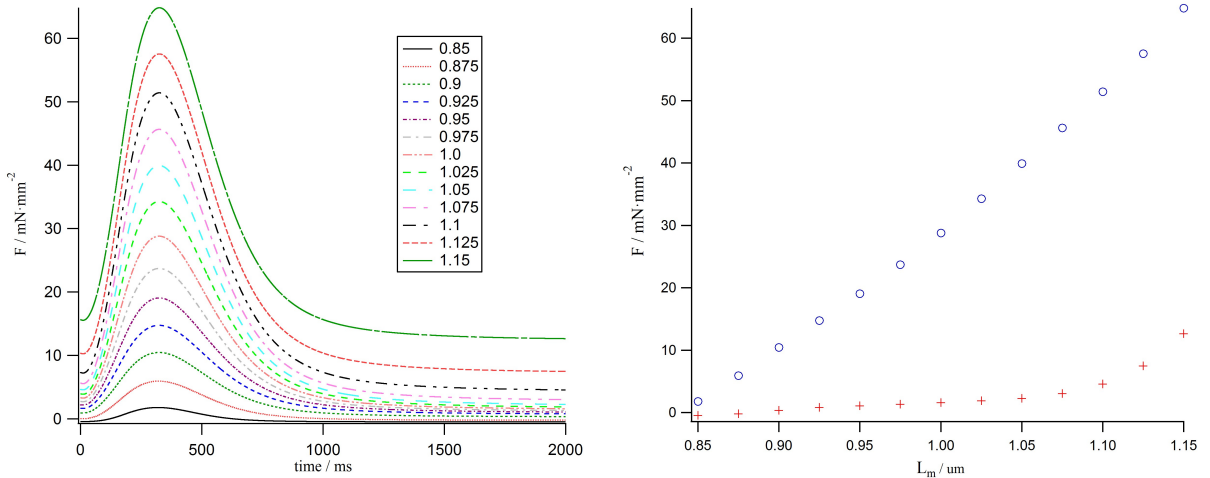


Figure 4.16: Isometric contraction at 1 Hz pacing frequency for TNNP model. The total muscle length is ranging from 0.85 and 1.15 μm . Left: Total muscle force profiles. Right: Elastic behavior of the cardiac muscle. (○) points represent the maximum peak force value of F , while (+) data are the resting value.

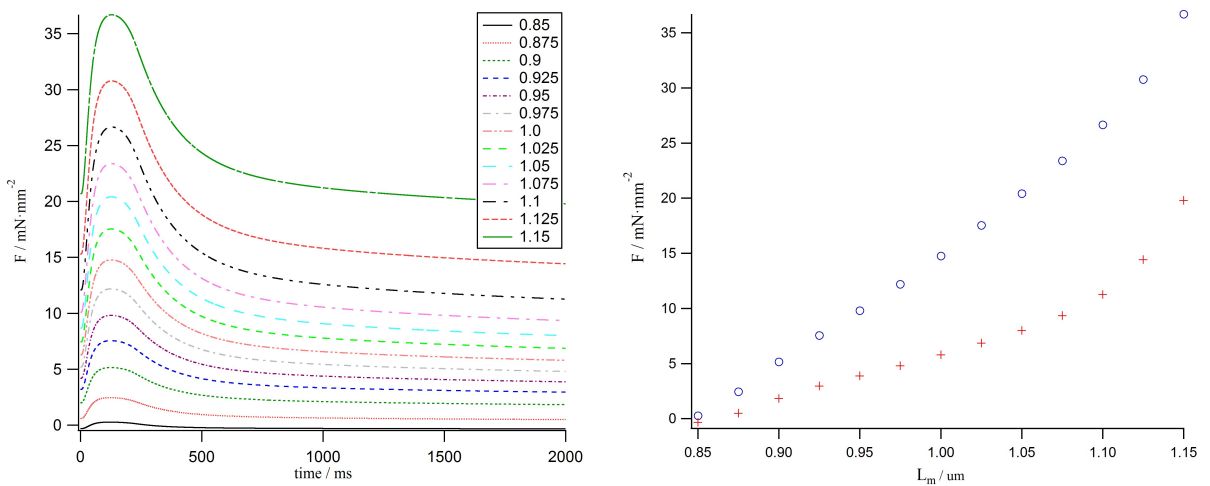


Figure 4.17: Isometric contraction at 1 Hz pacing frequency for JRW model. The total muscle length is ranging from 0.85 and 1.15 μm . Left: Total muscle force profiles. Right: Elastic behavior of the cardiac muscle. (○) points represent the maximum peak force value of F , while (+) data are the resting value.

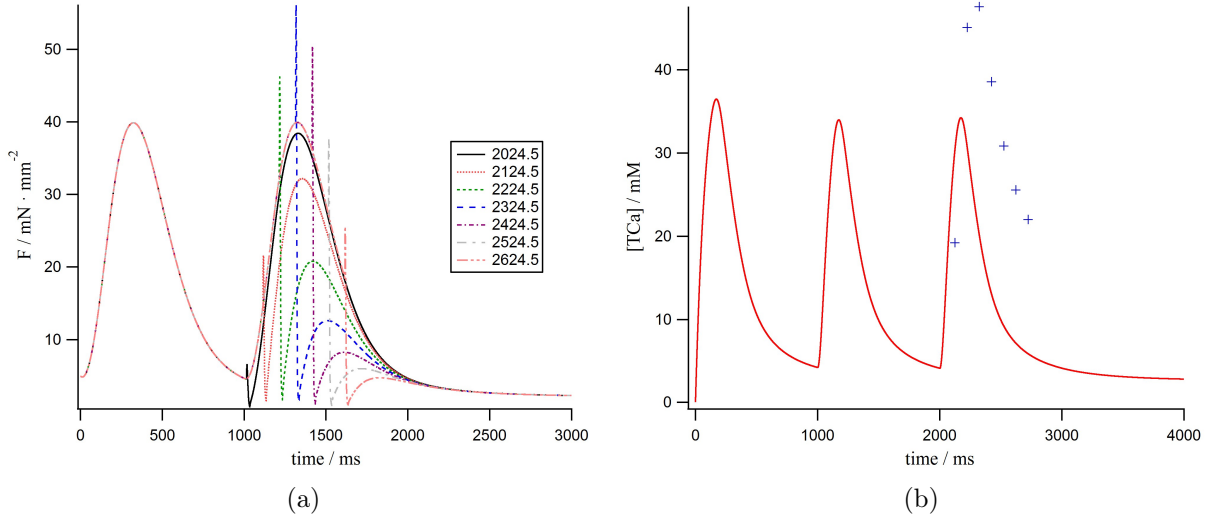


Figure 4.18: Estimation of $[TCa]$ time evolution for TNNP model. The data was obtained from a $0.04 \mu\text{m}$ length pulse of length 0.02 s. (a): Isometric force response to different muscle length pulse applied at different time course. (b): Estimated TCa time course (+) with the associated TCa profile from normal isometric contraction.

(Section 4.2.1). Furthermore, we observe a typical decrease of the systolic peak force for step length occurring before the time of maximum systolic force [18]. This decrease tends to be small when the step length happens at early time of the isometric twitch. This is explained by the fact that when the pulse if triggered at early time, the dynamic of the system enables the part of crossbridges detached to return to an active state before the beginning of the muscle relaxation. This can be confirmed by the force response to pulses done after the systolic peak, where the recovery does not attain large force values and return rapidly to diastolic level. The estimated TCa time course for the different models are presented on Figures 4.18b for TNNP and 4.19b for JRW model. It presents the normal time course of TCa in isometric twitch (solid line) and the estimated values (\circ) computed from the relation: $F'(t)/(Y_2 \cdot A \cdot h_c)$. The derivative is calculated by central finite differences after the length pulse, at the time of rapid force recovery. We can see that the typical TCa time course is reproduced with reasonable accuracy. Even if the concentration level is too high for both ionic models, the dynamics are well reproduced and follow the associated TCa evolution from an normal isometric contraction. The observed difference on the concentration levels might be caused by the large time step between points (data was saved at each 0.1 ms) that can lead to inaccuracy on the approximated time derivative.

One last point to mention is the effect on $[Ca^{2+}]$ due to length step or pulses applied on the course of an isometric contraction, which have been reported in some experimental results [70]. In our models, any influence was not observed during the protocol length step pulses displayed in Figures 4.18 and 4.19. This is mainly due to the too small contribution of the coupling part on the dynamics of the Ca_i^{2+} concentration as it was reported on Figure 4.20. The effect of step pulses can be seen directly on those graphs, but the low values obtained (around 10^{-6} - 10^{-7}) do not lead to influence the calcium transient dynamics. We can conclude that the coupled relation defined in Section 3.2 can be improved and some of the coupling effects between the calcium dynamics and the mechanical contraction are missing in such a simple description.

During heart contraction the muscle passes through a series of particular steps [71] firstly the muscle, from an initial force and length condition, begins to contract isometrically following a stimulus excitation. Then, when the generated tension reaches its load value (induced mainly by the ventricular or aortic pressure caused by their filling [67], [68]), the muscle begins to shorten while maintaining the force constant (isotonic contraction). This load is typically called afterload

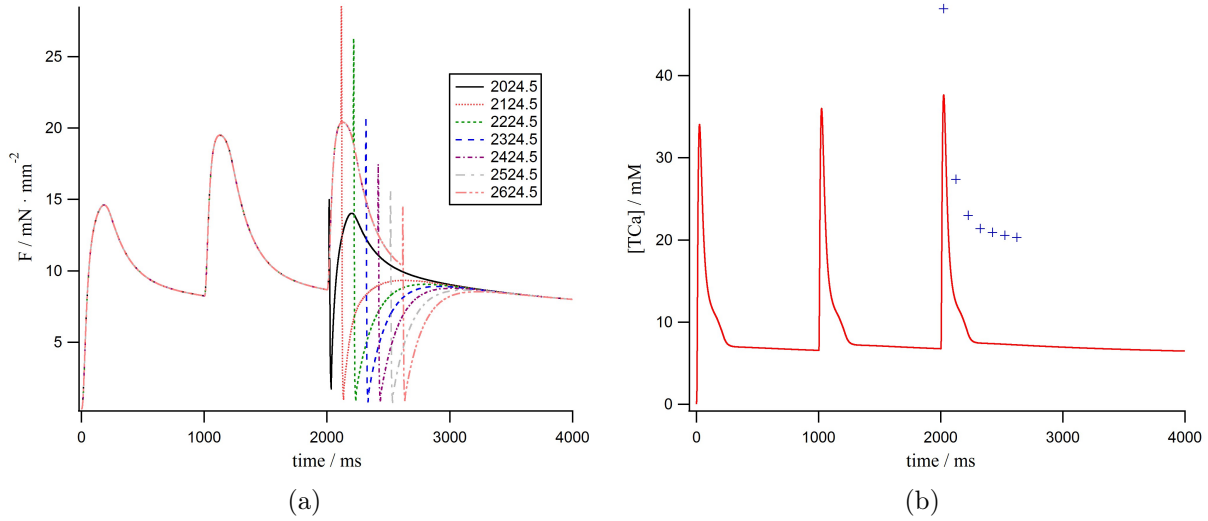


Figure 4.19: Estimation of $[TCa]$ time evolution for JRW model. The data was obtained from a $0.04 \mu\text{m}$ length pulse of length 0.02 s. (a): Isometric force response to different muscle length pulse applied at different time course. (b): Estimated TCa time course (+) with the associated TCa profile from normal isometric contraction.

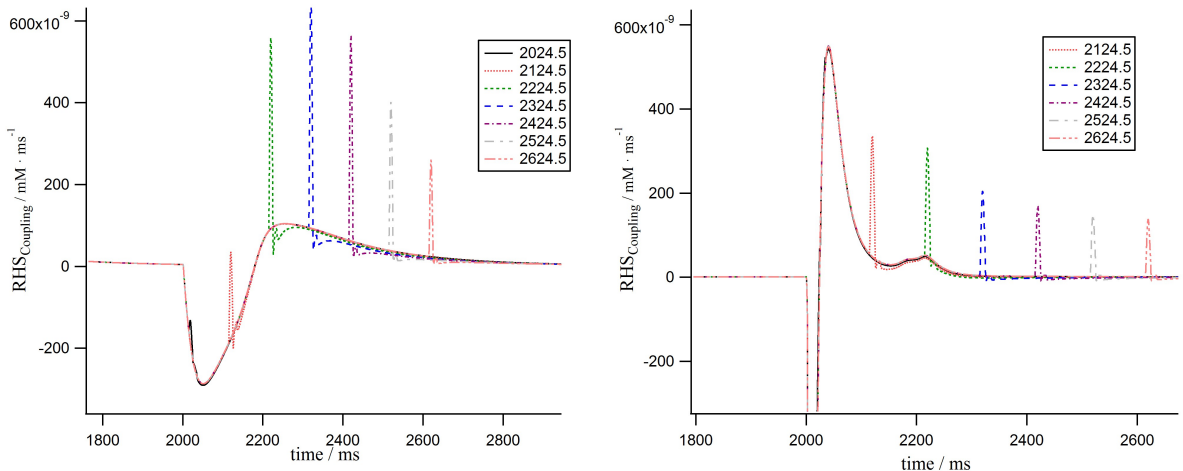


Figure 4.20: Values of the $F(Q_b, Q_r, Q_{d2})$ coupling term for TNNP (left) and JRW (right) obtained from an isometric contraction response to the different pulses length.

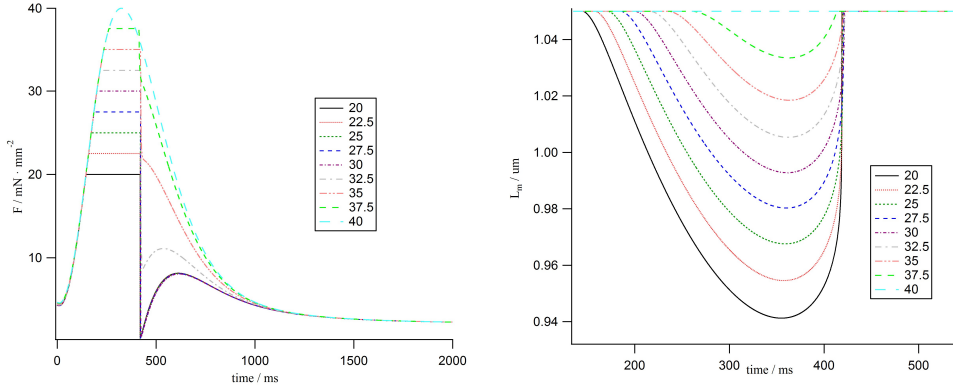


Figure 4.21: Series of afterloaded contraction experiments for the TNNP model. The results were obtained from clamp isotonic force ranging from 20 to 40 $\text{mN} \cdot \text{mm}^{-2}$. Left: F_m force muscle length. Right: L_m total muscle length.

and represents the load (or weight¹) that the muscle length experiences after it starts shortening [68]. After the necessary decrease, the muscle relaxes firstly by an isotonic, then by an isometric contraction.

A way to simulate these mechanical dynamics is by the afterloaded contraction protocols described on Section 3.2.2. The results obtained are displayed on Figures 4.21 and 4.22. As it can be observed on Figures 4.21 and 4.22, the different level of afterload determines both the maximum and the speed of the muscle shortening. At low afterload level, the maximum speed and shortening are observed in both ionic coupled models, and tend to decrease with higher afterload. Furthermore, the abrupt fall of isometric force at the end of the isotonic lengthening relaxation is observed and reproduces well known experimental results [72]. The typical effect on the length contraction due to isotonic contraction can be explained by the length-tension relationship depicted in left Figures 4.16 and 4.17 [68]. When the tension generated by the sarcomere and the parallel elastic element (for a specific initial length) is equal to the afterload applied, the muscle begins to decrease in length until it reaches a particular one, denoted L_{min}^{Short} . This L_{min}^{Short} length is defined as the length such that its maximum isometric force matches the value of the applied afterload [67]. Consequently, when the afterload tends to be equal to the maximum isometric force ($39.93 \text{ mN} \cdot \text{mm}^{-2}$ for TNNP and around $20.41 \text{ mN} \cdot \text{mm}^{-2}$ at $1.05 \mu\text{m}$ preload), the shortening will abbreviate earlier because the length will reach faster the corresponding L_{min}^{Short} .

The second influence of afterload level on the contraction of the muscle length is the increase of shortening velocity. This behavior fits well to the well-known force-velocity relation which states that the velocity is inversely related to the generated tension during an isotonic contraction [73].

The last contraction protocol implemented consist of a quick-release of the muscle tension applied at the systolic peak force of an isometric contraction. The results are depicted on Figures 4.23 and 4.24 for the same afterloads used on the previous protocol. Quick-release is a typical experiment used to eliminate the contribution of the parallel elastic elements, which absorbs a part of the tension generated by the contractile element of the muscle [74]. Consequently, it enables to study directly the dynamics of the sarcomere and how fast it can induces a length contraction on the muscle. These experiments are almost equivalent to those presented on the first part of Section 4.2.1, and it is not surprising that the response of L_m follows the typical phases described earlier. Indeed, we observe firstly a rapid decrease of the length L_m , followed by a slower shortening speed as the previous results displayed in Fig 4.13. As for [18], it can be

¹Earlier, experiments on muscle physiology were usually done by applying a weight at one end of the muscle fibers and measuring the displacement of the fiber following a stimulation [68].

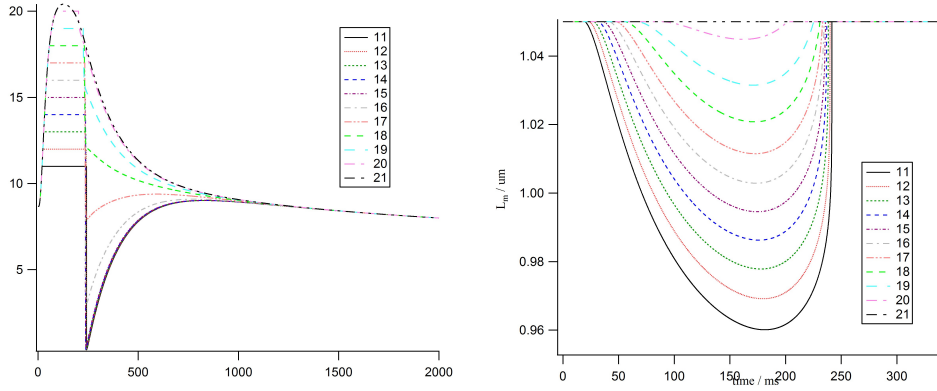


Figure 4.22: Series of afterloaded contraction experiments for the JRW model. The results were obtained from clamp isotonic force ranging from 20 to 40 $\text{mN}\cdot\text{mm}^{-2}$. Left: F_m force muscle length. Right: L_m total muscle length.

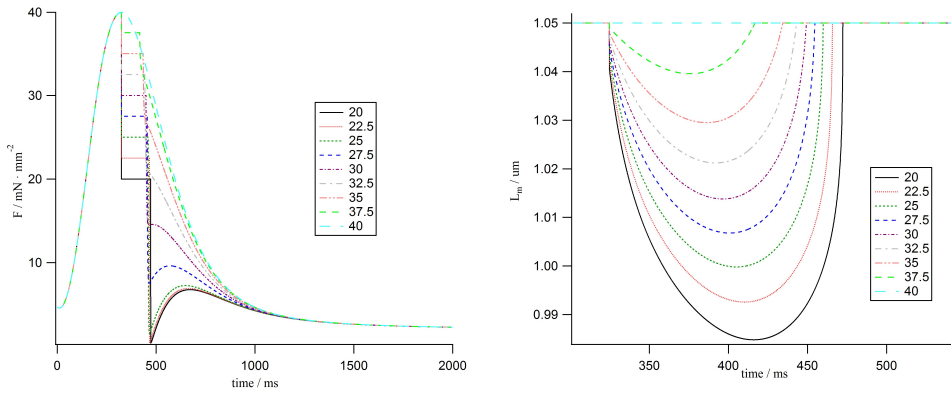


Figure 4.23: Series of quick-release contraction experiments for TNNP model. The results was obtained from clamp isotonic force ranging from 20 to 40 $\text{mN}\cdot\text{mm}^{-2}$ at the maximum isometric force F_m . Left: F_m force muscle length. Right: L_m total muscle length.

seen that for low afterloads, the relaxation starts earlier than the isometric contraction, except for the highest afterload. Indeed, it can be seen that the position of the maximum shortening displays a time shift from high to low afterload values. Moreover, the force profiles show that, at equivalent level of force, its decrease occurs earlier on time, synonym of a deactivation of the muscle length contraction. This effect is mainly due to rapid deactivation of the active states which can be observed in Figure 4.25 (only the TNNP results are presented). After the quick-release, the independent active state decrease rapidly due to the rapid shortening velocity created and the fact that their deactivation rate depends on $(dX/dt)^2$. Nevertheless, this deactivation effect is for instance not well determined [69], but two main theories are accepted. On one hand, it is suggested that the shortening contraction causes a momentary diminution of Ca^{2+} -troponin affinity [69]. On the other hand, the deactivation could be caused by a mechanical stress mechanism [69] [63] that leads to the uncoupling of the crossbridges. In our case, the NL model takes into account the first mechanism, simulated through the effective $T\text{Ca}$ (see Section 3.2.2).

We can observe also that, in the two coupled models, the force response is almost similar with respect to their own isometric profiles. In order to show more accurately the similar behavior, muscle velocity at the beginning of the contraction and the maximum length shortening are presented in Figure 4.26. As observed earlier, the velocity of initial shortening, together with the maximum stretching, diminish with the afterload applied after the quick-release, irrespective of

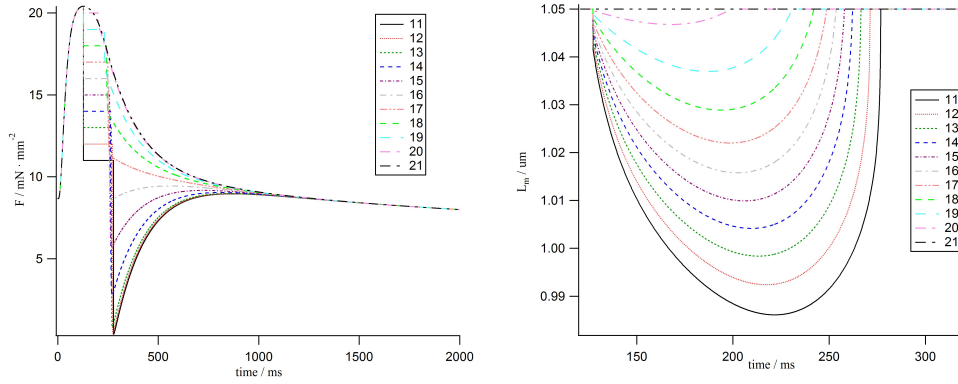


Figure 4.24: Series of quick-release contraction experiments for JRW model. The results was obtained from clamp isotonic force ranging from 20 to 40 $\text{mN} \cdot \text{mm}^{-2}$ at the maximum isometric force F_m . Left: F_m force muscle length. Right: L_m total muscle length.

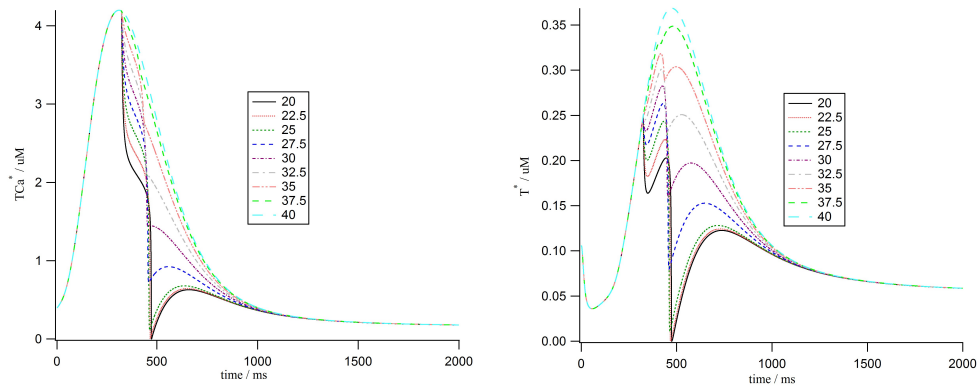


Figure 4.25: Active state profiles for different afterload quick-release contraction simulated with TNNP coupled model.

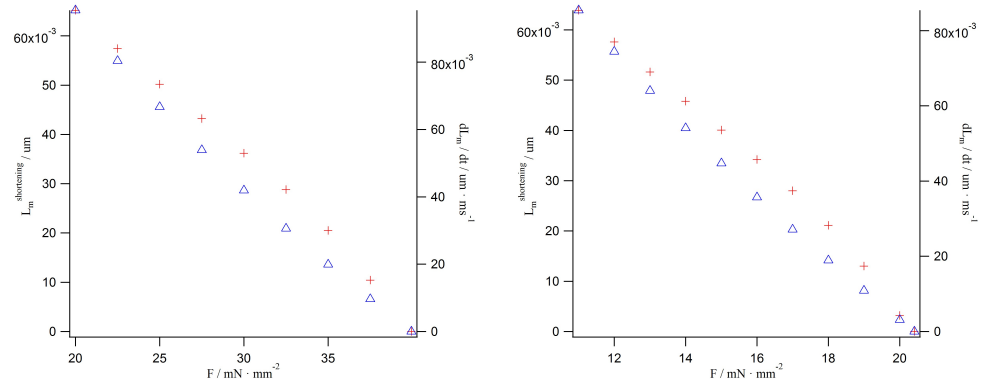


Figure 4.26: Muscle velocity shortening $\frac{dL_m}{dt}$ and maximum length shortening $L_m^{shortening}$ as a function of afterloaded F for TNNP model (left) and JRW model (right).

the model at hand.

Chapter 5

Conclusion and Perspectives

5.1 Conclusion

In order to create a complete multi-scale mathematical model for the heart physiology, the investigation of electromechanical coupled models is one of the challenges that might be treated. In our project, we focus on the implementation of two complete coupled-models, based on one hand on the ten Tusscher, Noble, Noble & Panfilov (2004) and the Jafri, Rice and Winslow (1998) model for the electrophysiological part and on the other hand based on the Negroni & Lascano (1995) for the mechanical part.

In chapter 4, we study the different models based on biological and physiological knowledge in order to investigate their validity. The results obtained are in a large part consistent with experimental results. The dynamics of the ionic channels (related to the gating variables) and the duration and amplitude of the ionic currents are well reproduced in both of the ionic models. Consequently, the different phases of the action potential have been observed and the difference between ventricular cells are consistent with reported results. Nonetheless, the simulated electrophysiology of ventricles display some specific errors with respect to the ionic model used. Indeed, the results of TNNP model presents a too high potential value which hinds partially the plateau phase of the action potential. It was postulated that this error might be mainly due to the choice of the parameters, which affects strongly the resolution of the ODE system. In the JRW case, the implemented model suffer from a non-steady calcium concentration. It was observed that the concentration into the sarcoplasmic reticulum increased with pacing. To ensure that the problem is not exclusively a numerical problem, two different integrators were used to compare the results on the calcium dynamics. Even if RK4 presents a better stability issue, the two integrators leads to the same abnormal evolution of the calcium, which enables to conclude that some parameters or equations are not correctly implemented.

In a second part of the chapter 4, the electromechanical model was tested. Despite the errors induced by the ionic model, the results are concordant to experimental results. The reproductive results of the NL model (at constant calcium concentration) gives similar value than the original paper. It enables also to give some hints that the NL model does not reproduce completely the muscle response to rapid force step (different phases) which is reported on some experimental works. It suggests that some kind of crossbridges states might be missing in this particular model.

Concerning the coupling part, the delay between the different components (potential, calcium, force) are reproduced. However, the created force, triggered by calcium transient concentration, presents some difference on the shape and amplitude. We have determined that these differences are mainly due to the respective differences on calcium dynamics between the two models, leading to different crossbridges activation. The effect of preload and afterload on the mechanical properties of the muscle are also correctly reproduced. Higher preload values leads to an increase

of diastolic but also systolic force contraction in both models. The problem of JRW, linked to Ca^{2+} concentration, induces however some errors on the diastolic evolution on the length-force profile. We observe also that the length pulse protocols does not lead to estimate correctly the concentration level of active states but reproduce well its respective time course. This protocol highlights also the weakness of electro-feedback coupling in both models and consequently the lack of accuracy of the coupled function $F(Q_b, Q_r, Q_{d2})$ used. Finally, the contraction protocols, which involve an isotonic contraction, were investigated. It displays the influence of afterloads on the dynamics of the active states, which leads to particular force and length response of the muscle to such perturbation.

5.2 Perspectives

One major difficulty, and time consuming, of the project is the research of adequate parameters needs to solve the ODEs associated to the ionic model. This point is particularly crucial in the context of a generalized multi-scale model of the heart in order to simulate data from different kind of patients or cells type. To this goal, some automatic parameter algorithm might be implemented to reduce the time spend on this particular work. However, up to date, such procedures is focused almost on phenomenological models, and the implementation for biological-based models still represents an important challenge [75], [76].

Another point that might be investigated is to electro-feedback coupling, which appears too small in our work. It seems that the coupling part implemented in the NL cannot suited for more complex ionic models, or that some of the feedback interaction sources are not taken into account. Changes in intracellular calcium handling or mechano-sensitive ions channels are such of underlying mechanisms that are not treated by our model, and influence conduction of cardiac cells [77]. Inclusion of thermodynamics aspects, through the ATP regulation, might also be included in order to correctly described the biochemistry, that form the base of the crossbridges movement on the thin filaments.

Finally, the indirect effects of drugs on the contraction muscle phenomenon might be investigated on the perspective of coupled models. Indeed, a large part of those substances acts mainly on the conductive part of cardiomyocytes but acts finally on the contraction rhythm or force of the heart as see in Tables 2.2 and 2.3. Such simulations will allow to understand more clearly the direct interactions between the drugs and the phenomenological response of the cardiac muscle.

Appendix

Ionic Models

ten Tusscher & al. model

We presented here the set of equations used in the TNNP model introduced in section 2.4.2

Differential Equations

$$\frac{dV}{dt} = -(I_{Na} + I_{K,1} + I_{to} + I_{Kr} + I_{Ks} + I_{Ca,L} + I_{NaCa} + I_{NaK} + I_{p(Ca)} + I_{p(K)} + I_{Ca,b} + I_{Na,b} + I_{stim}) \quad (5.1)$$

$$\frac{dX}{dt} = k_X \frac{X_\infty - X}{\tau_X}$$

For all $X = \{m, j, h, X_{r1}, X_{r2}, X_s, d, f, f_{Ca}, r, s, g\}$

If k_X is not mentionned in the equations below, then it is equal to 1.

$$\begin{aligned} \frac{d[Ca_i^{2+}]}{dt} &= \beta_i \left(\frac{V_{SR}}{V_c} (J_{leak} - J_{up} + J_{rel}) - (I_{Ca,L} + I_{Ca,b} + I_{p(Na)} - 2I_{NaCa}) \frac{C_m}{2V_c F} \right) \\ \frac{d[Ca_{SR}^+]}{dt} &= \beta_{SR} (J_{up} - J_{leak} - J_{rel}) \\ \frac{d[Na_i^+]}{dt} &= -(I_{Na} + I_{Na,b} + 3I_{NaCa} + 3I_{NaK}) \frac{C_m}{V_c F} \\ \frac{d[K_i^+]}{dt} &= -(I_{K,1} + I_{to} + I_{Kr} + I_{Ks} - 2I_{NaK} + I_{p(K)} + I_{stim}) \frac{C_m}{V_c F} \end{aligned} \quad (5.2)$$

Reversal potentials

$$\begin{aligned} E_{Na} &= \frac{RT}{F} \ln \left(\frac{[Na_o^+]}{[Na_i^+]} \right) \\ E_{Ca} &= \frac{RT}{2F} \ln \left(\frac{[Ca_o^{2+}]}{[Ca_i^{2+}]} \right) \\ E_K &= \frac{RT}{F} \ln \left(\frac{[K_o^+]}{[K_i^+]} \right) \\ E_{Ks} &= \frac{RT}{F} \ln \left(\frac{[K_o^+] + p_{Na,K}[Na_o^+]}{[K_i^+] + p_{Na,K}[Na_i^+]} \right) \end{aligned} \quad (5.3)$$

Calcium dynamics

$$\begin{aligned}
J_{rel} &= \left(a_{rel} \frac{[Ca_{SR}^{2+}]^2}{b_{rel}^2 + [Ca_{SR}^{2+}]^2} + c_{rel} \right) d \cdot g \\
J_{leak} &= V_{leak} ([Ca_{SR}^{2+}] - [Ca_i^{2+}]) \\
J_{up} &= \frac{V_{max,up}}{1 + \frac{K_{m,up}^2}{[Ca_i^{2+}]^2}}
\end{aligned} \tag{5.4}$$

$$\begin{aligned}
g_\infty &= \begin{cases} \frac{1}{1 + \left(\frac{[Ca_i^{2+}]}{0.00035}\right)^6} & \text{if } [Ca_i^{2+}] \leq 0.00035 \text{ mM} \\ \frac{1}{1 + \left(\frac{[Ca_i^{2+}]}{0.00035}\right)^{16}} & \text{otherwise} \end{cases} \\
\tau_g &= 2 \text{ ms} \\
k_g &= \begin{cases} 0 & \text{if } g_\infty > g \text{ and } V > -60 \text{ mV} \\ 1 & \text{otherwise} \end{cases} \\
\beta_i &= \left(1 + \frac{[Buf_c]_T K_{Buf_c}}{(K_{Buf_c} + [Ca_i^{2+}])^2} \right)^{-1} \\
\beta_{SR} &= \left(1 + \frac{[Buf_{sr}]_T K_{Buf_{sr}}}{(K_{Buf_{sr}} + [Ca_{SR}^{2+}])^2} \right)^{-1}
\end{aligned} \tag{5.5}$$

L-type Ca^{2+} channel

$$I_{Ca,L} = G_{Ca,L} \cdot d \cdot f \cdot f_{Ca} \cdot 4 \frac{VF^2}{RT} \frac{[Ca_i^{2+}] e^{\frac{2VF}{RT}} - 0.341 [Ca_o^{2+}]}{e^{\frac{2VF}{RT}} - 1} \tag{5.6}$$

$$\begin{aligned}
d_\infty &= \frac{1}{1 + e^{\frac{-V-5}{7.5}}} \\
\alpha_d &= \frac{1.4}{1 + e^{\frac{-V-35}{13}}} + 0.25 \\
\beta_d &= \frac{1.4}{1 + e^{\frac{V+5}{5}}} \\
\gamma_d &= \frac{1}{1 + e^{\frac{-V+50}{20}}} \\
\tau_d &= \alpha_d \beta_d + \gamma_d \\
f_\infty &= \frac{1}{1 + e^{\frac{V+20}{7}}} \\
\tau_f &= 1125e^{-\frac{(V+27)^2}{240}} + \frac{165}{1 + e^{\frac{-V+25}{10}}} + 80 \\
\alpha_{f_{Ca}} &= \frac{1}{1 + \left(\frac{[Ca_i^{2+}]}{0.000325}\right)^8} \\
\beta_{f_{Ca}} &= \frac{0.1}{1 + e^{\frac{[Ca_i^{2+}] - 0.0005}{0.0001}}} \\
\gamma_{f_{Ca}} &= \frac{0.2}{1 + e^{\frac{[Ca_i^{2+}] - 0.00075}{0.0008}}} \\
f_{Ca\infty} &= \frac{\alpha_{f_{Ca}} + \beta_{f_{Ca}} + \gamma_{f_{Ca}} + 0.23}{1.46} \\
\tau_{f_{Ca}} &= 2\text{ms} \\
k_{f_{Ca}} &= \begin{cases} 0 & \text{if } f_{Ca\infty} > f_{Ca} \text{ and } V > -60 \text{ mV} \\ 1 & \text{otherwise} \end{cases} \quad (5.7)
\end{aligned}$$

Fast Na^+ current

$$\begin{aligned}
I_{Na} &= G_{Na} m^3 h j(V - E_{Na}) \\
m_\infty &= \frac{1}{\left(1 + e^{\frac{-V-56.86}{9.03}}\right)^2} \\
\alpha_m &= \frac{1}{1 + e^{\frac{-V-60}{5}}} \\
\beta_m &= \frac{0.1}{1 + e^{\frac{V+35}{5}}} + \frac{0.1}{1 + e^{\frac{V-50}{200}}} \\
\tau_m &= \alpha_m \beta_m \\
h_\infty &= \frac{1}{\left(1 + e^{\frac{V+71.55}{7.43}}\right)^2} \\
j_\infty &= \frac{1}{\left(1 + e^{\frac{V+71.55}{7.43}}\right)^2} \\
\tau_h &= \frac{1}{\alpha_h + \beta_h} \\
\tau_j &= \frac{1}{\alpha_j + \beta_j} \quad (5.8)
\end{aligned}$$

For $V \geq -40\text{mV}$

$$\begin{aligned}\alpha_h &= 0.0 \\ \alpha_j &= 0.0 \\ \beta_h &= \frac{0.77}{0.13 \left(1 + e^{-\frac{V+10.66}{11.1}} \right)} \\ \beta_j &= 0.6 \frac{e^{0.057V}}{1 + e^{-0.1(V+32)}}\end{aligned}\tag{5.9}$$

For $V < -40\text{mV}$

$$\begin{aligned}\alpha_h &= 0.057e^{-\frac{V+80}{6.8}} \\ \alpha_j &= (-2.5428 \cdot 10^4 e^{0.2444V} - 6.948 \cdot 10^{-6} e^{-0.04391V}) \frac{V + 37.78}{1 + e^{0.311(V+79.23)}} \\ \beta_h &= 2.7e^{0.079V} + 3.1 \cdot 10^5 e^{0.3485V} \\ \beta_j &= 0.2424 \frac{e^{-0.01052V}}{1 + e^{-0.1378(V+40.14)}}\end{aligned}\tag{5.10}$$

Transient Outward Current

$$I_{to} = G_{to} \cdot r \cdot s(V - E_K)\tag{5.11}$$

For all cell types

$$\begin{aligned}r_\infty &= \frac{1}{1 + e^{\frac{-V+20}{6}}} \\ \tau_r &= 9.5e^{-\frac{(V+40)^2}{1800}} + 0.8\end{aligned}\tag{5.12}$$

For epicardial and M cells

$$\begin{aligned}s_\infty &= \frac{1}{1 + e^{\frac{V+20}{5}}} \\ \tau_s &= 85e^{-\frac{(V+45)^2}{320}} + \frac{5}{1 + e^{\frac{V-20}{5}}} + 3\end{aligned}\tag{5.13}$$

For endocardial cells

$$\begin{aligned}s_\infty &= \frac{1}{1 + e^{\frac{V+28}{5}}} \\ \tau_s &= 1000e^{-\frac{(V+67)^2}{1000}} + 8\end{aligned}\tag{5.14}$$

Slow Delayed Rectifier Current

$$\begin{aligned}
I_{Ks} &= G_{Ks} X_s^2 (V - E_{Ks}) \\
X_{s\infty} &= \frac{1}{1 + e^{\frac{-V-5}{14}}} \\
\alpha_{Xs} &= \frac{1100}{\sqrt{1 + e^{\frac{-V-10}{6}}}} \\
\beta_{Xs} &= \frac{1}{1 + e^{\frac{V-60}{20}}} \\
\tau_{Xs} &= \alpha_{Xs} \beta_{Xs}
\end{aligned} \tag{5.15}$$

Rapid Delayed Rectifier Current

$$\begin{aligned}
I_{Kr} &= G_{Kr} \sqrt{\frac{[K_o^+]}{5.4}} X_{r1} X_{r2} (V - E_K) \\
X_{r1\infty} &= \frac{1}{1 + e^{\frac{-V-26}{7}}} \\
\alpha_{Xr1} &= \frac{450}{1 + e^{\frac{-V-45}{10}}} \\
\beta_{Xr1} &= \frac{6}{1 + e^{\frac{V+30}{11.5}}} \\
\tau_{Xr1} &= \alpha_{Xr1} \beta_{Xr1} \\
X_{r2\infty} &= \frac{1}{1 + e^{\frac{V+88}{24}}} \\
\alpha_{Xr2} &= \frac{3}{1 + e^{\frac{-V-60}{20}}} \\
\beta_{Xr2} &= \frac{1.12}{1 + e^{\frac{V-60}{20}}} \\
\tau_{Xr2} &= \alpha_{Xr2} \beta_{Xr2}
\end{aligned} \tag{5.16}$$

Inward Rectifier K^+ current

$$\begin{aligned}
I_{K,1} &= G_{K,1} \sqrt{\frac{[K_o^+]}{5.4}} X_{K1\infty} (V - E_K) \\
X_{K1\infty} &= \frac{\alpha_{K,1}}{\alpha_{K,1} + \beta_{K,1}} \\
\alpha_{K,1} &= \frac{0.1}{1 + e^{0.06(V-E_K-200)}} \\
\beta_{K,1} &= \frac{3e^{0.0002(V-E_K+100)} + e^{0.1(V-E_K-10)}}{1 + e^{-0.5(V-E_K)}}
\end{aligned} \tag{5.17}$$

Na^+ - Ca^{2+} exchanger current

$$\begin{aligned}
I_{NaCa} &= k_{NaCa} \frac{1}{K_{m,Na}^3 + [Na_o^+]^3} \frac{1}{K_{m,Ca} + [Ca_o^{2+}]} \\
&\quad \frac{1}{1 + k_{sat} e^{\frac{(\gamma-1)V_F}{RT}}} \left(e^{\frac{\gamma V_F}{RT}} [Na_i^+]^3 [Ca_o^{2+}] - e^{\frac{(\gamma-1)V_F}{RT}} [Na_o^+]^3 [Ca_i^{2+}] \alpha \right)
\end{aligned} \tag{5.18}$$

Na^+ - K^+ pump

$$I_{NaK} = P_{NaK} f_{NaK} \frac{[Na_i^+]}{[Na_i^+] + K_{m,Na_i}} \frac{[K_o^+]}{[K_o^+] + K_{m,K_o}}$$

$$f_{NaK} = \frac{1}{1 + 0.1245e^{-\frac{0.1VF}{RT}} + 0.0353e^{-\frac{VF}{RT}}} \quad (5.19)$$

Sarcolemmal Ca^{2+} pump current

$$I_{p(Ca)} = G_{p(Ca)} \frac{[Ca_i^{2+}]}{[Ca_i^{2+}] + K_{p(Ca)}} \quad (5.20)$$

K^+ plateau current

$$I_{Kp} = G_{Kp} \frac{V - E_K}{1 + e^{\frac{25-V}{5.98}}} \quad (5.21)$$

Ca^{2+} background current

$$I_{Ca,b} = G_{Ca,b}(V - E_{Ca}) \quad (5.22)$$

Na^+ background current

$$I_{Na,b} = G_{Na,b}(V - E_{Na}) \quad (5.23)$$

Jafri Rice & Winslow model

We presented here the set of equations used in the JRW model introduced in section 2.4.2

Ca^{2+} subsystem

$$J_{rel} = \nu_1 (P_{O_1} + P_{O_2})([Ca_{JSR}^{2+}] - [Ca_{ss}^{2+}])$$

$$J_{leak} = \nu_2 ([Ca_{NSR}^{2+}] - [Ca_i^{2+}])$$

$$J_{up} = \nu_3 \frac{[Ca_i^{2+}]^2}{[Ca_i^{2+}]^2 + K_{m,up}^2}$$

$$J_{tr} = \frac{[Ca_{NSR}^{2+}] - [Ca_{JSR}^{2+}]}{\tau_{tr}}$$

$$J_{xfer} = \frac{[Ca_{ss}^{2+}] - [Ca_i^{2+}]}{\tau_{xfer}}$$

$$J_{HTRPN} = k_{HTRPN}^+ [Ca_i^{2+}] ([HTRPN]_{Tot} - [HTRPNCa]) - k_{HTRPN}^- [HTRPNCa]$$

$$J_{LTRPN} = k_{LTRPN}^+ [Ca_i^{2+}] ([LTRPN]_{Tot} - [LTRPNCa]) - k_{LTRPN}^- [LTRPNCa]$$

$$J_{TRPN} = J_{HTRPN} + J_{LTRPN} \quad (5.24)$$

$$\begin{aligned}
B_i &= \left(1 + \frac{[CMDN]_{Tot} K_m^{CMDN}}{(K_m^{CMDN} + [Ca_i^{2+}])^2} \right)^{-1} \\
B_{ss} &= \left(1 + \frac{[CMDN]_{Tot} K_m^{CMDN}}{(K_m^{CMDN} + [Ca_{ss}^{2+}])^2} \right)^{-1} \\
B_{JSR} &= \left(1 + \frac{[CSQN]_{Tot} K_m^{CCQN}}{(K_m^{CSQN} + [Ca_{JSR}^{2+}])^2} \right)^{-1}
\end{aligned} \tag{5.25}$$

$$\frac{d[Ca_i^{2+}]}{dt} = B_i \left(J_{leak} + J_{xfer} - J_{up} - J_{TRPN} - (I_{Ca,b} - 2I_{NaCa} + I_{p,Ca}) \frac{A_{cap}}{2V_{myo}F} \right) \tag{5.26}$$

$$\frac{d[Ca_{ss}^{2+}]}{dt} = B_{ss} \left(J_{rel} \frac{V_{JSR}}{V_{ss}} - J_{xfer} \frac{V_{myo}}{V_{ss}} - I_{Ca,L} \frac{A_{cap}}{2V_{ss}F} \right) \tag{5.27}$$

$$\frac{d[Ca_{JSR}^{2+}]}{dt} = B_{JSR} (J_{tr} - J_{rel}) \tag{5.28}$$

$$\frac{d[Ca_{NSR}^{2+}]}{dt} = (J_{up} - J_{leak}) \frac{V_{myo}}{V_{NSR}} - J_{tr} \frac{V_{JSR}}{V_{NSR}} \tag{5.29}$$

L-type Ca^{2+} channel

$$\begin{aligned}
\alpha &= 0.4 \cdot e^{\frac{V+12}{10}} \\
\beta &= 0.05 \cdot e^{-\frac{V+12}{13}} \\
\alpha' &= a \cdot \alpha \\
\beta' &= \frac{\beta}{b} \\
\gamma &= 0.1875 \cdot [Ca_{ss}^{2+}]
\end{aligned} \tag{5.30}$$

$$\begin{aligned}
\frac{dC_0}{dt} &= \beta C_1 + \omega C_{Ca_0} - (4\alpha + \gamma) C_0 \\
\frac{dC_1}{dt} &= 4\alpha C_0 + 2\beta C_2 + \frac{\omega}{b} C_{Ca_1} - (\beta + 3\alpha + \gamma a) C_1 \\
\frac{dC_2}{dt} &= 3\alpha C_1 + 3\beta C_3 + \frac{\omega}{b^2} C_{Ca_2} - (2\beta + 2\alpha + \gamma a^2) C_2 \\
\frac{dC_3}{dt} &= 2\alpha C_2 + 4\beta C_4 + \frac{\omega}{b^3} C_{Ca_3} - (3\beta + \alpha + \gamma a^3) C_3 \\
\frac{dC_4}{dt} &= \alpha C_3 + gO + \frac{\omega}{b^4} C_{Ca_4} - (4\beta + f + \gamma a^4) C_4 \\
\frac{dO}{dt} &= fC_4 - gO \\
\frac{dC_{Ca_0}}{dt} &= \beta' C_{Ca_1} + \gamma C_0 - (4\alpha' + \omega) C_{Ca_0} \\
\frac{dC_{Ca_1}}{dt} &= 4\alpha' C_{Ca_0} + 2\beta' C_{Ca_2} + \gamma a C_1 - \left(\beta' + 3\alpha' + \frac{\omega}{b}\right) C_{Ca_1} \\
\frac{dC_{Ca_2}}{dt} &= 3\alpha' C_{Ca_1} + 3\beta' C_{Ca_3} + \gamma a^2 C_2 - \left(2\beta' + 2\alpha' + \frac{\omega}{b^2}\right) C_{Ca_2} \\
\frac{dC_{Ca_3}}{dt} &= 2\alpha' C_{Ca_2} + 4\beta' C_{Ca_4} + \gamma a^3 C_3 - \left(3\beta' + \alpha' + \frac{\omega}{b^3}\right) C_{Ca_3} \\
\frac{dC_{Ca_4}}{dt} &= \alpha' C_{Ca_3} + g' O_{Ca} + \gamma a^4 C_4 - \left(4\beta' + f' + \frac{\omega}{b^4}\right) C_{Ca_4} \\
\frac{dO_{Ca}}{dt} &= f' C_{Ca_4} - g' O_{Ca}
\end{aligned} \tag{5.31}$$

$$\begin{aligned}
\frac{dy}{dt} &= \frac{y_\infty - y}{\tau_y} \\
y_\infty &= \frac{1}{1 + e^{\frac{V+55}{7.5}}} + \frac{0.1}{1 + e^{\frac{-V+21}{6}}} \\
\tau_y &= 20 + \frac{600}{e^{\frac{V+30}{9.5}}} \\
P_K &= \frac{\bar{P}_K}{1 + \frac{I_{Ca,L}}{I_{Ca,L,half}}} \\
I_{Ca_{max}} &= \bar{P}_{Ca} 4 \frac{VF^2}{RT} \frac{0.001 e^{\frac{2VF}{RT}} - 0.341 [Ca_o^{2+}]}{e^{\frac{2VF}{RT}} - 1} \\
I_{Ca,L} &= y(O + O_{Ca}) I_{Ca_{max}} \\
I_{Ca,L,K} &= P_K y(O + O_{Ca}) \frac{VF^2}{RT} \frac{[K_i^+] e^{\frac{VF}{RT}} - [K_o^+]}{e^{\frac{VF}{RT}} - 1}
\end{aligned} \tag{5.32}$$

Differential Equations

$$\begin{aligned}
\frac{dV}{dt} &= \frac{1}{C_m} (- (I_{Na} + I_{Ca,L} + I_K + I_{K,1} + I_{K_p} + I_{NaCa} + I_{NaK} \\
&\quad + I_{ns(Ca)} + I_{p(Ca)} + I_{Ca,L,K} + I_{Ca,b} + I_{Na,b}) + I_{stim})
\end{aligned} \tag{5.33}$$

$$\begin{aligned}
\frac{dm}{dt} &= \alpha_m(1 - m) - \beta_m m \\
\frac{dh}{dt} &= \alpha_h(1 - h) - \beta_h h \\
\frac{dj}{dt} &= \alpha_j(1 - j) - \beta_j j \\
\frac{dx}{dt} &= \alpha_x(1 - x) - \beta_x x \\
\frac{d[Na_i^+]}{dt} &= - (I_{Na} + I_{Na,b} + I_{ns(Na)} + 3I_{NaCa} + 3I_{NaK}) \frac{A_{cap}}{V_{myo}F} \\
\frac{d[K_i^+]}{dt} &= - (I_K + I_{K,1} + I_{ns(K)} + I_{K_p} - 2I_{NaK} + I_{Ca,L,K}) \frac{A_{cap}}{V_{myo}F} \\
\frac{d[HTRPNCa]}{dt} &= J_{HTRPN} \\
\frac{d[LTRPNCa]}{dt} &= J_{LTRPN}
\end{aligned} \tag{5.34}$$

Fast Na^+ current

$$\begin{aligned}
I_{Na} &= \bar{G}_{Na} m^3 h j (V - E_{Na}) \\
E_{Na} &= \frac{RT}{F} \ln \left(\frac{[Na_o^+]}{[Na_i^+]} \right) \\
\alpha_m &= 0.32 \frac{V + 47.13}{1 - e^{-0.1(V+47.13)}} \\
\beta_m &= 0.08 \cdot e^{-\frac{V}{11}}
\end{aligned} \tag{5.35}$$

For $V \geq -40$ mV

$$\begin{aligned}
\alpha_h &= 0.0 \\
\alpha_j &= 0.0 \\
\beta_h &= \frac{1}{0.13 \left(1 + e^{-\frac{V+10.66}{11.1}} \right)} \\
\beta_j &= 0.3 \frac{e^{-2.535 \cdot 10^{-7} V}}{1 + e^{-0.1(V+32)}}
\end{aligned} \tag{5.36}$$

For $V < -40$ mV

$$\begin{aligned}
\alpha_h &= 0.135 \cdot e^{-\frac{V+80}{6.8}} \\
\alpha_j &= (-127140e^{0.2444V} - 3.474 \cdot 10^{-5} e^{-0.04391V}) \frac{V + 37.78}{1 + e^{0.311(V+79.23)}} \\
\beta_h &= 3.56e^{0.079V} + 3.1 \cdot 10^5 e^{0.35V} \\
\beta_j &= 0.1212 \frac{e^{-0.01052V}}{1 + e^{-0.1378(V+40.14)}}
\end{aligned} \tag{5.37}$$

Time-dependent K^+ current

$$\begin{aligned}
I_K &= \bar{G}_K x_i x^2 (V - E_K) \\
E_K &= \frac{RT}{F} \ln \left(\frac{[K_o^+] + P_{Na,K}[Na_o^+]}{[K_i^+] + P_{Na,K}[Na_i^+]} \right) \\
\bar{G}_K &= 0.001128 \sqrt{\frac{[K_o^+]}{5.4}} \\
x_i &= \frac{1}{1 + e^{\frac{V-56.26}{32.1}}} \\
\alpha_x &= 7.19 \cdot 10^{-5} \frac{V + 30}{1 - e^{-0.148(V+30)}} \\
\beta_x &= 1.31 \cdot 10^{-4} \frac{V + 30}{-1 + e^{0.0687(V+30)}} \tag{5.38}
\end{aligned}$$

Time-independent K^+ current

$$\begin{aligned}
I_{K,1} &= \bar{G}_{K,1} K_{1\infty} (V - E_{K,1}) \\
E_{K,1} &= \frac{RT}{F} \ln \left(\frac{[K_o^+]}{[K_i^+]} \right) \\
\bar{G}_{K,1} &= 7.5 \cdot 10^{-3} \sqrt{\frac{[K_o^+]}{5.4}} \\
K_{1\infty} &= \frac{\alpha_{K,1}}{\alpha_{K,1} + \beta_{K,1}} \\
\alpha_{K,1} &= \frac{1.02}{1 + e^{0.2385(V-E_{K,1}-59.215)}} \\
\beta_{K,1} &= 0.4912 \frac{e^{0.08032(V-E_{K,1}+5.476)} + e^{0.06175(V-E_{K,1}-594.31)}}{1 + e^{-0.5143(V-E_{K,1}+4.753)}} \tag{5.39}
\end{aligned}$$

Plateau K^+ current

$$\begin{aligned}
I_{K_p} &= \bar{G}_{K_p} K_p (V - E_{K_p}) \\
E_{K_p} &= E_{K,1} \\
K_p &= \frac{1}{1 + e^{-\frac{-V+7.488}{5.98}}} \tag{5.40}
\end{aligned}$$

Na^+ - Ca^{2+} exchanger current

$$\begin{aligned}
I_{NaCa} &= k_{NaCa} \frac{1}{K_{m,Na}^3 + [Na_o^+]^3} \frac{1}{K_{m,Ca} + [Ca_o^{2+}]} \\
&\quad \frac{1}{1 + k_{sat} e^{\frac{(\eta-1)VF}{RT}}} \left(e^{\frac{\eta VF}{RT}} [Na_i^+]^3 [Ca_o^{2+}] - e^{\frac{(\eta-1)VF}{RT}} [Na_o^+]^3 [Ca_i^{2+}] \right) \tag{5.41}
\end{aligned}$$

Na^+ - K^+ pump

$$\begin{aligned}
I_{NaK} &= \bar{I}_{NaK} f_{NaK} \frac{1}{1 + \left(\frac{K_{m,Na_i}}{[Na_i^+]} \right)^{1.5}} \frac{[K_o^+]}{[K_o^+] + K_{m,K_o}} \\
f_{NaK} &= \frac{1}{1 + 0.1245e^{\frac{-0.1VF}{RT}} + 0.0365\sigma e^{\frac{-VF}{RT}}} \\
\sigma &= \frac{1}{7} \left(e^{\frac{[Na_o^+]}{67.3}} - 1 \right)
\end{aligned} \tag{5.42}$$

Nonspecific Ca^{2+} activated current

$$\begin{aligned}
I_{ns(Ca)} &= I_{ns(Na)} + I_{ns(K)} \\
E_{ns(Ca)} &= \frac{RT}{F} \ln \left(\frac{[K_o^+] + [Na_o^+]}{[K_i^+] + [Na_i^+]} \right) \\
V_{ns(Ca)} &= V - E_{ns(Ca)} \\
\bar{I}_{ns(Na)} &= P_{ns(Ca)} \frac{V_{ns(Ca)} F^2}{RT} \frac{0.75[Na_i^+] e^{\frac{V_{ns(Ca)} F}{RT}} - 0.75[Na_o^+]}{e^{\frac{V_{ns(Ca)} F}{RT}} - 1} \\
\bar{I}_{ns(K)} &= P_{ns(Ca)} \frac{V_{ns(Ca)} F^2}{RT} \frac{0.75[K_i^+] e^{\frac{V_{ns(Ca)} F}{RT}} - 0.75[K_o^+]}{e^{\frac{V_{ns(Ca)} F}{RT}} - 1} \\
I_{ns(Na)} &= \bar{I}_{ns(Na)} \frac{1}{1 + \left(\frac{K_{m,ns(Ca)}}{[Ca_i^{2+}]} \right)^3} \\
I_{ns(K)} &= \bar{I}_{ns(K)} \frac{1}{1 + \left(\frac{K_{m,ns(Ca)}}{[Ca_i^{2+}]} \right)^3}
\end{aligned} \tag{5.43}$$

Sarcolemmal Ca^{2+} pump current

$$I_{p(Ca)} = \bar{I}_{p(Ca)} \frac{[Ca_i^{2+}]}{[Ca_i^{2+}] + K_{m,p(Ca)}} \tag{5.44}$$

Ca^{2+} background current

$$\begin{aligned}
I_{Ca,b} &= \bar{G}_{Ca,b} (V - E_{Ca,N}) \\
E_{Ca,N} &= \frac{RT}{2F} \ln \left(\frac{[Ca_o^{2+}]}{[Ca_i^{2+}]} \right)
\end{aligned} \tag{5.45}$$

Na^+ background current

$$\begin{aligned}
I_{Na,b} &= \bar{G}_{Na,b} (V - E_{Na,N}) \\
E_{Na,N} &= E_{Na}
\end{aligned} \tag{5.46}$$

RyR channel states (Keizer and Levine)

$$\begin{aligned}
 \frac{dP_{C_1}}{dt} &= -k_a^+ [Ca_{ss}^{2+}]^n P_{C_1} + k_a^- P_{O_1} \\
 \frac{dP_{C_2}}{dt} &= k_c^+ P_{O_1} - k_c^- P_{C_2} \\
 \frac{dP_{O_1}}{dt} &= k_a^+ [Ca_{ss}^{2+}]^n P_{C_1} - k_a^- P_{O_1} - k_b^+ [Ca_{ss}^{2+}]^m P_{O_1} + k_b^+ P_{O_2} - k_c^+ P_{O_1} + k_c^- P_{C_2} \\
 \frac{dP_{O_2}}{dt} &= k_b^+ [Ca_{ss}^{2+}]^m P_{O_1} - k_b^- P_{O_2}
 \end{aligned} \tag{5.47}$$

Electrical pacing protocol C++ code

This section presents the three major kind of stimulation protocol used for the action potential analysis cited in chapter 3.

Fixed Cycle Length

```

1 void StimulationProtocol::fixedCycleLength( const Real& t, const Real& dt, int&
    NbStimulus, Real& Iapp )
{
3   if ( NbStimulus < M_nbStimMax )
{
5     if ( t >= M_timeSt && t <= M_timeSt + M_StimDuration ) // Apply the electrical
        simulation
{
7       Iapp = M_Istim;
8       if ( t >= M_timeSt + M_StimDuration - dt && t <= M_timeSt + M_StimDuration )
// In order to applied once
9       {
10         NbStimulus++;
11         M_timeSt = M_timeSt + M_stInt; // Next stimulation time
12       }
13     }
14     else
15       Iapp = 0;
16   }
17   else
18     Iapp = 0;
19 }
```

S1-S2 Standard Restitution Protocol

```

1 void StimulationProtocol::standardS1S2Protocol( const Real& t, const Real& dt, int
    & NbStimulus, Real& Iapp )
{
3   if ( t < M_nbStimMax * M_stInt )
{
5     if ( t >= M_timeSt && t <= M_timeSt + M_StimDuration ) // Apply the electrical
        simulation
{
7       Iapp = M_Istim;

9       if ( t >= M_timeSt + M_StimDuration - dt && t <= M_timeSt + M_StimDuration )
// In order to apply once
10      {
11        M_timeSt = M_timeSt + M_stInt; // Next stimulation time
12      }
13    }
14  }
15 }
```

```

13         if ( t > ( M_nbStimMax - 1 ) * M_stInt && t < M_nbStimMax * M_stInt ) // Counter returns to zero at last repeated S1 stimuli
14             NbStimulus = 0;
15
16         else
17             NbStimulus++;
18     }
19
20     else
21         Iapp = 0;
22 }
23
24 else
25 {
26     if ( M_stIntS1S2 >= M_stIntS1S2Min ) // While S1S2 interval larger than min S1-S2 interval
27     {
28         if ( t >= M_timeSt && t <= M_timeSt + M_StimDuration ) // Apply the electrical simulation
29         {
30             Iapp = M_Istim;
31
32             if ( t >= M_timeSt + M_StimDuration - dt && t <= M_timeSt + M_StimDuration )
33                 // In order to apply once
34             {
35                 NbStimulus++;
36
37                 if ( NbStimulus < M_repeatSt ) // Repeat S1 stimuli between each S2
38                     M_timeSt = M_timeSt + M_stInt;
39
40                 else if ( NbStimulus == M_repeatSt ) // Time of the S2 stimulus
41                     M_timeSt = M_timeSt + M_stIntS1S2;
42
43                 else if ( NbStimulus == M_repeatSt + 1 ) // After S2, decrease S1-S2 interval
44                 {
45                     M_timeSt = M_timeSt + M_stInt;
46                     NbStimulus = 0;
47
48                     if ( M_stIntS1S2 > 1000 )
49                         M_stIntS1S2 = M_stIntS1S2 - 1000;
50
51                     else if ( M_stIntS1S2 <= 1000 && M_stIntS1S2 > 300 )
52                         M_stIntS1S2 = M_stIntS1S2 - 50;
53
54                     else if ( M_stIntS1S2 <= 300 && M_stIntS1S2 > 200 )
55                         M_stIntS1S2 = M_stIntS1S2 - 10;
56
57                     else if ( M_stIntS1S2 <= 200 )
58                         M_stIntS1S2 = M_stIntS1S2 - 5;
59
60                 }
61
62                 else
63                     Iapp = 0;
64
65             }
66         }
67     }
68 }
```

Dynamic Restitution Protocol

```

void StimulationProtocol::dynamicProtocol( const Real& t, const Real& dt, int&
2   NbStimulus, Real& Iapp )
{
  if ( M_stInt >= M_stIntMin ) // While S1-S1 interval larger than min S1-S1
  interval
4  {
    if ( t >= M_timeSt && t <= M_timeSt + M_StimDuration ) // Apply the electrical
    simulation
5  {
      Iapp = M_Istim;

8    if ( t >= M_timeSt + M_StimDuration - dt && t <= M_timeSt + M_StimDuration )
    // In order to apply once
10   {
      NbStimulus++;
      M_timeSt = M_timeSt + M_stInt;
    }
14   }
  else
16   Iapp = 0;

18   if ( t > M_tShortS1S1 ) // After each stabilizing time, change S1-S1 interval
19   {
20     if ( M_stInt > 1000 )
21     {
22       M_stInt      = M_stInt - 1000;
23       M_tShortS1S1 = M_tShortS1S1 + M_stInt * M_repeatSt;
24     }
25     else if ( M_stInt <= 1000 && M_stInt > 300 )
26     {
27       M_stInt      = M_stInt - 50;
28       M_tShortS1S1 = M_tShortS1S1 + M_stInt * M_repeatSt;
29     }
30     else if ( M_stInt <= 300 && M_stInt > 200 )
31     {
32       M_stInt      = M_stInt - 10;
33       M_tShortS1S1 = M_tShortS1S1 + M_stInt * M_repeatSt;
34     }
35     else if ( M_stInt <= 200 )
36     {
37       M_stInt      = M_stInt - 5;
38       M_tShortS1S1 = M_tShortS1S1 + M_stInt * M_repeatSt;
39     }
40   }
41   else
42   Iapp = 0;
43 }

```

Crossbridges Model

This section presents the Matlab code used to compute the muscle dynamics submitted to constant calcium concentration introduced in section 3.2.1.

```

%%%
2 % Negroni Lascano muscle model
%%%
4 clc
6 close all

```

```

8 % Parameters
10 % =====
12 Y1 = 39e-3; % 1 / ( uM * ms )
13 Z1 = 30e-3; % 1 / ms
14 Y2 = 1.3e-3; % 1 / ms
15 Z2 = 1.3e-3; % 1 / ms
16 Y3 = 30e-3; % 1 / ms
17 Z3 = 1560e-3; % 1 ( uM * ms )
18 Y4 = 40e-3; % 1 / ms
19 Yd = 9e3; % ms / um^2
20 Tt = 70; % uM
21 B = 1200e-3; % 1 / ms
22 hc = 0.005; % um
23 La = 1.17; % um
24 R = 20; % 1 / um^2

26 cCar = 0.04; % uM
27 Kp = 150e-3; % uM / ms
28 Km = 0.1; % uM
29 Qm = 1600e-3; % uM / ms
30 t1 = 0.025e3; % ms

32 A = 1800; % mM / mm^2 / um / uM
33 K = 140000; % mM / mm^2 / um^5
34 L0 = 0.97; % um
35 alpha = 0.5; % mN / mm^2
36 beta = 100; % 1 / um

38 method = 'IsotonicChange';

40 % Fonctions for resolution of the cross-bridge model
41 % =====
42 t = linspace(0, 200, 2000);
43 N = length(t);

46 if strcmp(method, 'NoIsometric')
47 dL = 0.5 * linspace(-0.005, 0.001, 25);
48 M = length(dL);
49 L = zeros(N, M);
50 L(1, :) = 1.05;
51 stepLNew = 1000;
52 dtStep = 2;
54 elseif strcmp(method, 'IsotonicChange')
55 dF = linspace(-75, 0, 6);
56 DF = length(dF);
57 F0 = zeros(N, DF);
58 F0(1, :) = 90;
59 L = zeros(N, DF);
60 L(1, :) = 1.05;
61 stepLNew = 200;
62 dtStep = 1;
66 end

68 T = @(TCa, TCas, Ts) Tt - TCa - TCas - Ts;
69 TCaEff = @(TCa, L) TCa .* exp(-R * (L - La).^2);

```

```

70 Qb = @(t, cCa, TCa, TCas, Ts) Y1 * cCa * T(TCa, TCas, Ts) - Z1 * TCa;
72 Qa = @(TCa, TCas, L) Y2 * TCaEff(TCa, L) - Z2 * TCas;
74 QR = @(t, cCa, TCas, Ts) Y3 * TCas - Z3 * Ts * cCa;
76 Qd = @(Ts) Y4 * Ts;
Qd1 = @(v, Ts) Yd * v * v * Ts;
Qd2 = @(v, TCas) Yd * v * v * TCas;

78 dTCa = @(t, cCa, TCa, TCas, Ts, L) Qb(t, cCa, TCa, TCas, Ts) - Qa(TCa, TCas, L)
    ;
80 dTCas = @(t, v, cCa, TCa, TCas, Ts, L) Qa(TCa, TCas, L) - QR(t, cCa, TCas, Ts) -
    Qd2(v, TCas);
dTc = @(t, v, cCa, TCa, TCas, Ts) QR(t, cCa, TCas, Ts) - Qd(Ts) - Qd1(v, Ts);

82 dX = @(t, X, L) B * (L - X - hc);
84 dXBE = @(t, dt, X, L) (X + dt * B * (L - hc)) / (1 + dt * B);

86 dTCaBE = @(t, dt, cCa, TCa, TCas, Ts, L) (TCa / dt + Y1 * cCa * (Tt - TCas
    - Ts) + Z2 * TCas) / (1.0 / dt + Y1 * cCa + Z1 + Y2 * exp(-R * (L - La)
    .^2));
dTCasBE = @(t, dt, v, cCa, TCa, TCas, Ts, L) (TCas / dt + Y2 * TCa * exp(-R *
    (L - La).^2) + Z3 * Ts * cCa) / (1.0 / dt + Z2 + Y3 + Yd * v.^2);
88 dTsBE = @(t, dt, v, cCa, TCa, TCas, Ts) (Ts / dt + Y3 * TCas) / (1.0 / dt +
    Z3 * cCa + Y4 + Yd * v.^2);

90 % Resolution of crossbriges model
92 %=====

94 if (strcmp(method, 'NoIsometric')) )
96
98 X = zeros(N,M);
X(1,:) = L(1,:)-hc;

100 TCa = zeros(N,M);
TCa(1,:) = 35.4752; % Initial value
102 TCas = zeros(N,M);
TCas(1,:) = 20.5848; % Initial value
104 Ts = zeros(N,M);
Ts(1,:) = 0.1954; % Initial value
106 cCai = 2.0*ones(N,M);

108 F = zeros(N,M);
F1 = zeros(M,1);
F2 = zeros(M,1);

112 for i = 1 : M
    for j = 1 : N - 1
114        dt = t(j+1) - t(j);
116        Fb = A * (TCas(j, i) + Ts(j, i)) * (L(j, i) - X(j, i));
118        Fp = K * (L(j, i) - L0).^5;
        F(j, i) = Fp + Fb;

120        % Length step modification at some specific time step (stepLNew) applied
once.

122        if (j > stepLNew && j <= stepLNew + dtStep)
            L(j+1, i) = L(j, i) + dL(i) / dtStep;
        else

```

```

126    L( j + 1, i ) = L( j, i );
127    end
128
129    vi = dX( t( j ), X( j, i ), L( j, i ) );
130
131    % Predictor step
132
133    TCa( j + 1, i ) = TCa( j, i ) + dt * dTCa( t( j ), cCai(j), TCa( j, i
134    ), TCas( j, i ), Ts( j, i ), L( j, i ) );
135    TCas( j + 1, i ) = TCas( j, i ) + dt * dTCas( t( j ), vi, cCai(j), TCa( j
136    ), i ), TCas( j, i ), Ts( j, i ), L( j, i ) );
137    Ts( j + 1, i ) = Ts( j, i ) + dt * dTs( t( j ), vi, cCai( j ), TCa(
138    j, i ), TCas( j, i ), Ts( j, i ) );
139
140    X( j + 1, i ) = dXB( t( j + 1 ), dt, X( j, i ), L( j + 1, i ) );
141    vip1 = dX( t( j + 1 ), X( j + 1, i ), L( j + 1, i ) );
142
143    % Corrector step
144
145    TCa( j + 1, i ) = TCa( j, i ) + 0.5 * dt * ( dTCa( t( j + 1 ), cCai( j
146    ) + 1 ), TCa( j + 1, i ), TCas( j + 1, i ), Ts( j + 1, i ), L( j + 1, i ) ) ...
147    + dTCa( t( j ), cCai(j), TCa( j, i ), TCas( j, i ), Ts( j, i ), L( j, i
148    ) );
149    TCas( j + 1, i ) = TCas( j, i ) + 0.5 * dt * ( dTCas( t( j + 1 ), vip1,
cCai( j + 1 ), TCa( j + 1, i ), TCas( j + 1, i ), Ts( j + 1, i ), L( j + 1, i
) ) ...
150    + dTCas( t( j ), vi, cCai(j), TCa( j, i ), TCas( j, i ), Ts( j, i ), L(
j, i ) );
151    Ts( j + 1, i ) = Ts( j, i ) + 0.5 * dt * ( dTs( t( j + 1 ), vip1,
cCai( j + 1 ), TCa( j + 1, i ), TCas( j + 1, i ), Ts( j + 1, i ) ) ...
152    + dTs( t( j ), vi, cCai( j ), TCa( j, i ), TCas( j, i ), Ts( j, i ) ) );
153
154    end
155    end
156
157    for i = 1:M % Data for the force-length curve
158        if dL(i) < 0
159            Fref = F(stepLNew-450, i);
160            F1(i) = min(F(stepLNew:stepLNew+10,i));
161            posF1 = find(F(:,i) == F1(i));
162            F1(i) = F1(i) / Fref;
163            F2(i) = F(posF1+50,i) / Fref;
164        else
165            Fref = F(stepLNew-450, i);
166            F1(i) = max(F(stepLNew:stepLNew+10,i));
167            posF1 = find(F(:,i) == F1(i));
168            F1(i) = F1(i) / Fref;
169            F2(i) = F(posF1+50, i) / Fref;
170        end
171    end
172
173
174    figure(1)
175    plot(dL,F1, 'bo', dL,F2, 'ro');
176
177    % Saving data
178
179    tableF = [t, F];
180    table = [dL, F1, F2];
181    save('outputFNoIsomet.txt', 'tableF', '-ascii');
182    save('outputF1F2.txt', 'table', '-ascii');
183
184
185    elseif (strcmp(method, 'Isometric') )

```

```

180
181 L = 1.05;
182 X = zeros(N,1);
183 X(1) = L-hc;
184
185 TCa = zeros(N,1);
186 TCa(1) = 35.4752; % Initial value
187 TCas = zeros(N,1);
188 TCas(1) = 20.5848; % Initial value
189 Ts = zeros(N,1);
190 Ts(1) = 0.1954; % Initial value
191 cCai = 2.0*ones(N,1);
192
193 F = zeros(N,1);
194
195 for j = 1 : N - 1
196
197 dt = t(j + 1) - t(j);
198
199 Fb = A * (TCas(j) + Ts(j)) * (L - X(j));
200 Fp = K * (L - L0)^5;
201 F(j) = Fp + Fb;
202
203 vi = dX(t(j), X(j), L);
204
205 % Predictor step
206
207 TCa(j + 1) = TCa(j) + dt * dTCa(t(j), cCai(j), TCa(j), TCas(j),
208 , Ts(j), L);
208 TCas(j + 1) = TCas(j) + dt * dTCas(t(j), vi, cCai(j), TCa(j), TCas(j),
209 , Ts(j), L);
209 Ts(j + 1) = Ts(j) + dt * dTs(t(j), vi, cCai(j), TCa(j), TCas(j),
210 , Ts(j));
211
212 X(j + 1) = dXB(t(j + 1), dt, X(j), L);
213 vip1 = dX(t(j + 1), X(j + 1), L);
214
215 % Corrector step
216
217 TCa(j + 1) = TCa(j) + 0.5 * dt * (dTCa(t(j + 1), cCai(j + 1),
218 , TCa(j + 1), TCas(j + 1), Ts(j + 1), L) ...
218 + dTCa(t(j), cCai(j), TCa(j), TCas(j), Ts(j), L));
219 TCas(j + 1) = TCas(j) + 0.5 * dt * (dTCas(t(j + 1), vip1, cCai(j +
220 , TCa(j + 1), TCas(j + 1), Ts(j + 1), L) ...
220 + dTCas(t(j), vi, cCai(j), TCa(j), TCas(j), Ts(j), L));
221 Ts(j + 1) = Ts(j) + 0.5 * dt * (dTts(t(j + 1), vip1, cCai(j + 1,
222 , TCa(j + 1), TCas(j + 1), Ts(j + 1)) ...
222 + dTs(t(j), vi, cCai(j), TCa(j), TCas(j), Ts(j)));
223 end
224
225 figure(2)
226 plot(t, TCa, t, TCas, t, Ts)
227 legend('TCa', 'TCas', 'Ts')
228
229 figure(3)
230 plot(t, F);
231 legend('F');
232
233 figure(200)
234 plot(t, X, 'b');
235
236 elseif strcmp(method, 'IsotonicChange')

```

```

238 X      = zeros(N,DF);
X(1,:) = L(1,:)-hc;
240
241 TCa   = zeros(N,DF);
242 TCa(1,:) = 35.4752; % Initial value
243 TCas = zeros(N,DF);
244 TCas(1,:) = 20.5848; % Initial value
245 Ts    = zeros(N,DF);
246 Ts(1,:) = 0.1954; % Initial value
247
248 cCai = 2.0*ones(N,1);
249
250 for i = 1 : DF
251     for j = 1 : N - 1
252
253         dt = t(j+1) - t(j);
254
255         vi = dX(t(j), X(j,i), L(j,i));
256         dFb = A * (TCas(j,i) + Ts(j,i));
257
258         % Force step modification at some specific time step (stepLNew) applied
259         % once.
260
261         if (j > stepLNew && j <= stepLNew + dtStep)
262             F0(j+1,i) = F0(j,i) + dF(i);
263         else
264             F0(j+1,i) = F0(j,i);
265         end
266
267         L(j+1,i) = L(j,i);
268
269         for k = 1:10
270             Fb = dFb * (L(j+1,i) - X(j,i));
271             Fp = K * (L(j+1,i) - L0).^5;
272             dFp = 5 * K * (L(j+1,i) - L0).^4;
273             G = Fp + Fb - F0(j+1,i);
274             dG = dFp + dFb;
275             L(j+1,i) = L(j+1,i) - G / dG;
276         end
277
278         % Predictor step
279
280         TCa(j+1,i) = TCa(j,i) + dt * dTCa(t(j), cCai(j), TCa(j,i),
281                                         TCas(j,i), Ts(j,i), L(j,i));
282         TCas(j+1,i) = TCas(j,i) + dt * dTCas(t(j), vi, cCai(j), TCa(j,i),
283                                         TCas(j,i), Ts(j,i), L(j,i));
284         Ts(j+1,i) = Ts(j,i) + dt * dTs(t(j), vi, cCai(j), TCa(j,i),
285                                         TCas(j,i), Ts(j,i));
286
287         X(j+1,i) = dXB(t(j+1), dt, X(j,i), L(j+1,i));
288         vip1 = dX(t(j+1), X(j+1,i), L(j+1,i));
289
290         % Corrector step
291
292         TCa(j+1,i) = TCa(j,i) + 0.5 * dt * (dTCa(t(j+1), cCai(j+1),
293                                         TCa(j+1,i), TCas(j+1,i), Ts(j+1,i), L(j+1,i)) ...
294                                         + dTCa(t(j), cCai(j), TCa(j,i), TCas(j,i), Ts(j,i), L(j,i)));
295         TCas(j+1,i) = TCas(j,i) + 0.5 * dt * (dTCas(t(j+1), vip1,
296                                         cCai(j+1), TCa(j+1,i), TCas(j+1,i), Ts(j+1,i), L(j+1,i)) ...
297                                         + dTCas(t(j), vi, cCai(j), TCa(j,i), TCas(j,i), Ts(j,i), L(j,i)));

```

```

292     j , i ) ) );
293     Ts( j + 1, i ) = Ts( j , i ) + 0.5 * dt * ( dTs( t( j + 1 ), vip1 ,
294     cCai( j + 1 ), TCa( j + 1, i ), TCas( j + 1, i ), Ts( j + 1, i ) ) ...
295     + dTs( t( j ), vi , cCai( j ), TCa( j , i ), TCas( j , i ), Ts( j , i ) ) );
296
297 end
298 end
299
300 col = [ 'y' , 'm' , 'k' , 'r' , 'g' , 'b' ];
301 for i = 1:DF
302     figure( 600 )
303     plot(t , F0(:,i) , col(i));
304     hold on;
305     figure( 700 )
306     plot(t , L(:,i) , col(i));
307     hold on;
308 end
309 hold off;
310
311 tableL = [t , L, F0];
312 save('outputF0LIsotonic.txt' , 'tableL' , '-ascii');
313

```

Bibliography

- [1] Gallant's Biology Stuff. <http://kvhs.nbed.nb.ca/gallant/biology/biology.html>. Accessed: 2013-06-18.
- [2] Nikhil V. Munshi. Gene regulatory networks in cardiac conduction system development. *Circulation Research*, 110(11):1525–1537, 2012.
- [3] Muscular cells type. <http://www.nsbri.org/HumanPhysSpace/focus5/earthphys-frame.html>. Accessed: 2013-06-19.
- [4] Master 1, Physio Animale-Chapitre 1: la Circulation sanguine. <http://www.biodeug.com/master-1-physio-animale-chapitre-1-circulation-sanguine/>. Accessed: 2013-06-19.
- [5] Coen Ottenheijm, Leo Heunks, and Richard Dekhuijzen. Diaphragm adaptations in patients with copd. *Respiratory Research*, 9(1):12, 2008.
- [6] Mariana Ruiz Villarreal. Cell membrane. https://en.wikipedia.org/wiki/Cell_membrane/. Accessed: 2013-06-19.
- [7] B. Alberts, D. Bray, K. Hopkin, A. Johnson, Lewis J., Raff M., Roberts K., and Walter P. *Essential cell biology, second edition*. Garland Science, 2004.
- [8] Mariana Ruiz Villarreal. GapJunction. https://en.wikipedia.org/wiki/Gap_junction. Accessed: 2013-06-19.
- [9] Penn State. global logoBiology 230 - Molecules and Cells.
- [10] Electrocardiograma. <http://es.wikipedia.org/wiki/Electrocardiograma>. Accessed: 2013-06-19.
- [11] David Richfield. Sarcomere. <http://en.wikipedia.org/wiki/Sarcomere>. Accessed: 2013-06-19.
- [12] Kimberly Frei. 2 Muscles and functions. <http://www.studyblue.com/notes/note/n/2-muscles-and-functions/deck/6056990>. Accessed: 2013-06-19.
- [13] The heart. In James Keener and James Sneyd, editors, *Mathematical Physiology*, volume 8/2 of *Interdisciplinary Applied Mathematics*, pages 523–626. Springer New York, 2009.
- [14] FrankB. Sachse. 7. cardiac electrophysiology. In *Computational Cardiology*, volume 2966 of *Lecture Notes in Computer Science*, pages 157–219. Springer Berlin Heidelberg, 2004.
- [15] A. L. Hodgkin and A. F. Huxley. A quantitative description of membrane current and its application to conduction and excitation in nerve. *The Journal of Physiology*, 117(4):500–544, 1952.

- [16] Emmanuel Drouin, Flavien Charpentier, Chantal Gauthier, Karine Laurent, and Herve Le Marec. Electrophysiologic characteristics of cells spanning the left ventricular wall of human heart: Evidence for presence of m cells. *Journal of the American College of Cardiology*, 26(1):185 – 192, 1995.
- [17] Muscle. In James Keener and James Sneyd, editors, *Mathematical Physiology*, volume 8/2 of *Interdisciplinary Applied Mathematics*, pages 717–772. Springer New York, 2009.
- [18] Jorge A. Negroni and Elena C. Lascano. A cardiac muscle model relating sarcomere dynamics to calcium kinetics. *Journal of Molecular and Cellular Cardiology*, 28(5):915 – 929, 1996.
- [19] Gallant's Biology Stuff. <http://www.e-cardiogram.com>. Accessed: 2013-06-19.
- [20] M.R. Boyett, S.M. Harrison, N.C. Janvier, S.O. McMorn, J.M. Owen, and Z. Shui. A list of vertebrate cardiac ionic currents nomenclature, properties, function and cloned equivalents. *Cardiovascular Research*, 32(3):455–481, 1996.
- [21] HBP, The Human Brain Project. <http://www.humanbrainproject.eu/>. Accessed: 2013-04-30.
- [22] R.H. Clayton, O. Bernus, E.M. Cherry, H. Dierckx, F.H. Fenton, L. Mirabella, A.V. Panfilov, F.B. Sachse, G. Seemann, and H. Zhang. Models of cardiac tissue electrophysiology: Progress, challenges and open questions . *Progress in Biophysics and Molecular Biology* , 104(1–3):22 – 48, 2011. <ce:title>Cardiac Physiome project: Mathematical and Modelling Foundations</ce:title>.
- [23] Karen Cardona Julio Gomis Javier Saiz Jose Maria Ferrero (Jr.) Beatriz Trenor, Lucia Romero.
- [24] K. H. W. J. ten Tusscher, D. Noble, P. J. Noble, and A. V. Panfilov. A model for human ventricular tissue. *American Journal of Physiology - Heart and Circulatory Physiology*, 286(4):H1573–H1589, 2004.
- [25] R.A. Rhoades and D.R. Bell. *Medical Phisiology: Principles for Clinical Medicine*. Wolters Kluwer Health, 2012.
- [26] A.R. Boccaccini and S.E. Harding. *Myocardial Tissue Engineering*. Studies in Mechanobiology. Springer Berlin Heidelberg, 2011.
- [27] P. Lacolley. *Biologie et pathologie du coeur et des vaisseaux*. John Libbey Eurotext, 2007.
- [28] W. Contributors. *Human Physiology*. Blacksleet River.
- [29] P.J. Podrid and P.R. Kowey. *Cardiac Arrhythmia: Mechanisms, Diagnosis, and Management*. Lippincott Williams & Wilkins, 2001.
- [30] E.J. Topol and R.M. Califf. *Textbook of Cardiovascular Medicine*. Number vol. 355 in Textbook of Cardiovascular Medicine. Lippincott Williams & Wilkins, 2007.
- [31] R.H. Garrett, C.M. Grisham, and B. Lubochinsky. *Biochimie*. De Boeck Supérieur, 2000.
- [32] A.L. Kierszenbaum, P. Validire-Charpy, and P. Validire. *Histologie et biologie cellulaire: Une introduction à l'anatomie pathologique*. Biologie cellulaire et moléculaire. De Boeck Supérieur, 2006.

- [33] Cours d'Histologie Fonctionnelle dispensé par le Prof. Mark à la Faculté de Médecine de Walia/N'Djamena (Tchad) en 2008 et 2009. <http://udsmed.unistra.fr/emed/courses/HISTOFONCTTCHAD/>. Accessed: 2013-06-19.
- [34] B. Alberts, D. Bray, K. Hopkin, A. Johnson, Lewis J., Raff M., Roberts K., and Walter P. *L'essentiel de la biologie cellulaire, 2ème édition*. Flammarion Médecine-Sciences, 2004.
- [35] Dan M. Roden, Jeffrey R. Balser, Alfred L. George Jr, and Mark E. Anderson. Cardiac ion channels. *Annual Review of Physiology*, 64(1):431–475, 2002. PMID: 11826275.
- [36] G.A. Langer. *The Myocardium*. Elsevier Science, 1997.
- [37] Augustus O. Grant. Cardiac ion channels. *Circulation: Arrhythmia and Electrophysiology*, 2(2):185–194, 2009.
- [38] D.C. Sigg, P.A. Iaizzo, Y.F. Xiao, and B. He. *Cardiac Electrophysiology Methods and Models*. SpringerLink : Bücher. Springer US, 2010.
- [39] H.H. Girault. *Électrochimie physique et analytique*. Presses polytechniques et universitaires romandes, 2007.
- [40] A.J. Pullan, L.K. Cheng, and M.L. Buist. *Mathematically Modelling the Electrical Activity of the Heart: From Cell to Body Surface and Back Again*. World Scientific Publishing Company Incorporated, 2005.
- [41] W. Ganong and M. Jobin. *Physiologie médicale*. Anatomie - physiologie. De Boeck Supérieur, 2005.
- [42] S.V. Madihally. *Principles of Biomedical Engineering*. Artech House engineering in medicine & biology series. Artech House, Incorporated, 2010.
- [43] Muriel Boulakia, Miguel A. Fernández, Jean-Frédéric Gerbeau, and Nejib Zemzemi. Numerical simulations of electrocardiograms. In D. Ambrosi, A. Quarteroni, and G. Rozza, editors, *Modeling of Physiological Flows*, pages 77–106. Springer, 2011.
- [44] J.A. Southern P. Pathmanathan, G.R. Mirams and J.P. Whiteley. The significant effect of the choice of ionic current integration method in cardiac electrophysiological simulations. *International Journal for Numerical Methods in Biomedical Engineering*, 27:1751–1770, 2011.
- [45] M. Saleet Jafri, J. Jeremy Rice, and Raimond L. Winslow. Cardiac Ca^{2+} dynamics: The roles of ryanodine receptor adaptation and sarcoplasmic reticulum load. *Biophysical Journal*, 74(3):1149 – 1168, 1998.
- [46] S Sicouri and C Antzelevitch. A subpopulation of cells with unique electrophysiological properties in the deep subepicardium of the canine ventricle. the m cell. *Circulation Research*, 68(6):1729–41, 1991.
- [47] Michael Nabauer, Dirk J. Beuckelmann, Peter Uberfuhr, and Gerhard Steinbeck. Regional differences in current density and rate-dependent properties of the transient outward current in subepicardial and subendocardial myocytes of human left ventricle. *Circulation*, 93(1):168–177, 1996.
- [48] C H Luo and Y Rudy. A dynamic model of the cardiac ventricular action potential. i. simulations of ionic currents and concentration changes. *Circulation Research*, 74(6):1071–96, 1994.
- [49] John P. Imredy and David T. Yue. Mechanism of Ca^{2+} -sensitive inactivation of L-type Ca^{2+} channels . *Neuron*, 12(6):1301 – 1318, 1994.

- [50] J. Keizer and L. Levine. Ryanodine receptor adaptation and Ca²⁺(-)induced Ca²⁺ release-dependent Ca²⁺ oscillations . *Biophysical Journal* , 71(6):3477 – 3487, 1996.
- [51] John Jeremy Rice and Pieter P. de Tombe. Approaches to modeling crossbridges and calcium-dependent activation in cardiac muscle. *Progress in Biophysics and Molecular Biology*, 85(2–3):179 – 195, 2004. <ce:title>Modelling Cellular and Tissue Function</ce:title>.
- [52] Lifev. a parallel finite element library.
- [53] Veneziani Alessandro Perego, Mauro. An efficient generalization of the rush-larsen method for solving electro-physiology membrane equations. *ETNA. Electronic Transactions on Numerical Analysis [electronic only]*, 35:234–256, 2009.
- [54] Kimberly Frei. Cell ML. Language for storing and exchange of computer based mathematical models. <http://www.cellml.org>. Accessed: 2013-04-30.
- [55] G. Ng, ré, Kieran E. Brack, Vanlata H. Patel, and John H. Coote. Autonomic modulation of electrical restitution, alternans and ventricular fibrillation initiation in the isolated heart. *Cardiovascular Research*, 73(4):750–760, 2007.
- [56] Marcus L. Koller, Mark L. Riccio, and Robert F. Gilmour Jr. Dynamic restitution of action potential duration during electrical alternans and ventricular fibrillation. *American Journal of Physiology - Heart and Circulatory Physiology*, 275(5):H1635–H1642, 1998.
- [57] J. Wagner and J. Keizer. Effects of rapid buffers on Ca²⁺ diffusion and Ca²⁺ oscillations . *Biophysical Journal*, 67(1):447 – 456, 1994.
- [58] C.C.B. Anfinsen, J.J.T. Edsall, and F.F.M. Richards. *ADVANCES IN PROTEIN CHEMISTRY*. Number vol. 38 in Advances in protein chemistry. Elsevier Science, 1986.
- [59] Z Grabarek, P C Leavis, and J Gergely. Calcium binding to the low affinity sites in troponin c induces conformational changes in the high affinity domain. a possible route of information transfer in activation of muscle contraction. *Journal of Biological Chemistry*, 261(2):608–613, 1986.
- [60] Da-Wei Liu and Charles Antzelevitch. Characteristics of the delayed rectifier current (ikr and iks) in canine ventricular epicardial, midmyocardial, and endocardial myocytes : A weaker iks contributes to the longer action potential of the m cell. *Circulation Research*, 76(3):351–365, 1995.
- [61] Alfio Quarteroni, Paola Gervasio, and Fausto Saleri. Equations différentielles ordinaires. In *Calcul Scientifique*, pages 205–259. Springer Milan, 2010.
- [62] L. E. Ford, A. F. Huxley, and R. M. Simmons. Tension responses to sudden length change in stimulated frog muscle fibres near slack length. *The Journal of Physiology*, 269(2):441–515, 1977.
- [63] RAINER BODEM and EDMUND H. SONNENBLICK. Deactivation of contraction by quick releases in the isolated papillary muscle of the cat: Effects of lever damping, caffeine, and tetanization. *Circulation Research*, 34(2):214–225, 1974.
- [64] Gabriella Piazzesi, Leonardo Lucii, and Vincenzo Lombardi. The size and the speed of the working stroke of muscle myosin and its dependence on the force. *The Journal of Physiology*, 545(1):145–151, 2002.
- [65] Jorge A. Negroni and Elena C. Lascano. Simulation of steady state and transient cardiac muscle response experiments with a huxley-based contraction model. *Journal of Molecular and Cellular Cardiology*, 45(2):300 – 312, 2008.

- [66] R. Eckert and F. Math. *Physiologie anémale: Mécanismes et adaptations*. DeBoeck Université, 1999.
- [67] R.A. Rhoades and D.R. Bell. *Medical Physiology: Principles for Clinical Medicine*. Wolters Kluwer Health, 2012.
- [68] S. Sircar. *Principles of Medical Physiology*. Thieme Medical Publishers, 2008.
- [69] R.M. Enoka. *Neuromechanics of Human Movement*. Neuromechanics of Human Movement. Human Kinetics, 2008.
- [70] J. N. Peterson, W. C. Hunter, and M. R. Berman. Estimated time course of Ca^{2+} bound to troponin c during relaxation in isolated cardiac muscle. *American Journal of Physiology - Heart and Circulatory Physiology*, 260(3):H1013–H1024, 1991.
- [71] Lorenzo Sewanan. Modeling Cardiac Muscle Mechanics, Bachelor Thesis. <http://digitalrepository.trincoll.edu/theses/213/>, 4 2012. Accessed: 2013-04-30.
- [72] M. A. Goethals D. L. Brutsaert, N. M. de Clerck and P. R. Housmans. Relaxation of ventricular cardiac muscle. *J. Physiol.*, 283:469–480, 1978.
- [73] R.L. Bijlani and S. Manjunatha. *Understanding Medical Physiology: A Textbook for Medical Students*. Jaypee Bros. Medical Publishers, 2010.
- [74] A.M. Katz. *Physiology of the Heart*. Wolters Kluwer Health/Lippincott Williams & Wilkins Health, 2010.
- [75] Socrates Dokos and Nigel H. Lovell. Parameter estimation in cardiac ionic models. *Progress in Biophysics and Molecular Biology*, 85(2–3):407 – 431, 2004. <ce:title>Modelling Cellular and Tissue Function</ce:title>.
- [76] Optimisation of a Generic Ionic Model of Cardiac Myocyte Electrical Activity . *Computational and Mathematical Methods in Medicine*, 2013, 2013.
- [77] Peter Kohl and Ursula Ravens. Cardiac mechano-electric feedback: past, present, and prospect. *Progress in Biophysics and Molecular Biology*, 82(1–3):3 – 9, 2003. <ce:title>Mechano-Electric Feedback and Cardiac Arrhythmias</ce:title>.